ISSN 0137-5075
Index 351873

POLISH ACADEMY OF SCIENCES
INSTITUTE OF FUNDAMENTAL TECHNOLOGICAL RESEARCH
COMMITTEE ON ACOUSTICS · POLISH ACOUSTICAL SOCIETY

ARCHIVES of ACOUSTICS

QUARTERLY
Vol. 24, No 2
1999

POLISH SCIENTIFIC PUBLISHERS

WARSZAWA

CONTENTS

POLISH ACADEMY OF SCIENCES
INSTITUTE OF FUNDAMENTAL TECHNOLOGICAL RESEARCH
COMMITTEE ON ACOUSTICS • POLISH ACOUSTICAL SOCIETY

ARCHIVES of ACOUSTICS

QUARTERLY
Vol. 24, No 2
1999

POLISH SCIENTIFIC PUBLISHERS
WARSZAWA

Editorial Committee Office:
ul. Świętokrzyska 21, p. 508
00-049 Warszawa (Poland)
fax (48) (22) 826 98 15
phone (48) (22) 826 92 85
e-mail: publikac@ippt.gov.pl

PRINTED IN POLAND

Abstracted in Acoustics Abstracts, in Applied Mechanics Reviews and indexed in J. Acoust. Soc. Am.

Wydanie publikacji dofinansowane przez Komitet Badań Naukowych
Edition co-sponsored by State Committee for Scientific Research

Arkuszy wydawniczych 11,5
Arkuszy drukarskich 8,75
Skład: "MAT-TEX"
Druk i oprawa: Drukarnia Braci Grodzickich, Piaseczno, ul. Geodetów 47A

ARCHIVES OF ACOUSTICS
24, 2, 111–118 (1999)

EXPOSURES AND HEARING THRESHOLDS IN MUSIC STUDENTS DUE TO TRAINING SESSIONS

A. JAROSZEWSKI, T. FIDECKI and P. ROGOWSKI

Fr. Chopin Academy of Music
(00-368 Warszawa, Okólnik 2, Poland)

Measurements of SPL's in sound emission from some wind instruments during training sessions of music students show all in excess of L_{Amax} 110 dB and reach L_{Amax} 132 dB in some cases. Long time average spectra in 1/3-octave bands and cumulative distribution functions show that e.g. sound pressure levels L_{A} 50 are often around 100–110 dB and in most instruments the spectra cover substantial range of frequencies. Resting hearing thresholds in many students show dips of various depths at 6 kHz, which in some cases reach over 30 dB. TTS_2 measured at 6 kHz following 4-hrs training session reach 40 dB.

1. Introduction

The effects of exposure to music on hearing in musicians can be determined in two ways: by direct audiometric testing and indirectly by measurements of sound levels and duration of exposure in musical performances. In audiometric examination of classical musicians AXELSSON and LINDGREN [1], WESTMORE and EVERSDEN [17], RABINOWITZ *et al.* [14], KARLSSON *et al.* [12], JOHNSON *et al.* [11], JANSSON *et al.* [5]. WOOLFORD *et al.* [18], OSTRI *et al.* [13], and ROYSTER *et al.* [15], JAROSZEWSKI [8], JAROSZEWSKI *et al.* [10], JAROSZEWSKI *et al.* [9] and others all have found audiometric patterns corresponding to the noise induced hearing loss. The audiograms showed notches, mostly at frequency 6 kHz in 30% to over 50% of the tested samples. The depth of these notches varied between HTL 10 dB (OSTRI *et al.* [13], ROYSTER *et al.* [15]), and 20 to 25 dB (RABINOWITZ *et al.* [14], WOOLFORD *et al.* [18] up to 10–30 dB (JAROSZEWSKI [8]). The greatest hearing loss was found in musicians playing bassoon, horn, trumpet and trombone (e.g. AXELSSON and LINDGREN [1]). However, some investigators, e.g. WESTMORE *et al.* [17], AXELSSON and LINDGREN [1], have declared that only "*slight degree of hearing loss was found in the averaged hearing thresholds*" even that they also found notch shaped audiograms with the dip at 6 kHz in the tested samples.

In the investigation of sound exposures in Swedish symphonic orchestras JANSSON and KARLSSON [7] reported mean (for all tested music) L_{Aeq} values from 88.9 dB up to 93.1 dB with maximum values reaching 98.6 dB (for specific music and position). They have not observed A-weighted "short-time levels" exceeding 125 dB. Similar data L_{Aeq}

from 85 dB up to 90 dB with weekly equivalent of 85 dB were reported by AXELSSON and LINDGREN [1]. SCHACKE [16], recorded continuos sound pressure levels in orchestra of the Deutsche Oper Berlin, and found average A-weighted levels for brass ranging from 87 dB to 96 dB, with peaks reaching 122 dB and average A-weighted levels for woodwinds varying between 88 dB and 97 dB, with peaks reaching 117 dB. Lower values, in the range from 83 dB to 93 dB were found for violins and violas, however, with peaks reaching 110 dB. The presence of impulsive sounds in the exposure have been, as it is well known, recognised as having substantial contribution in the development of hearing loss (e.g. HENDERSON and HAMMERNIK [4]). It has been observed that interaction of peaks with continuous background produces larger hearing loss than should result from the sum of these components.

In the report by SCHACKE [16] $L_{\mathrm{Aeq\ 8h}}$ for wind instruments was determined at 87.7 dB which is almost twice as much as maximum permissible exposure according to German regulations, HAY [3]. CAMP and HORSTMAN [2] obtained values ranging from $L_{\mathrm{Aeq}} = 84.4$ dB to 98 dB for bass players and horn players correspondingly. While JAROSZEWSKI *et al.* found L_{Aeq} reaching 100 – 110 dB for e.q. trumpet player with substantial amount of impulsiveness. Alarming data on L_{Aeq} values were reported by ROYSTER *et al.* [15]. They found $L_{\mathrm{Aeq\ 8h}}$ values ranging from 74.7 to 94.7 dB and "*maximum peak levels*" in the range from 112.0 to 143.5 dB (A-weighted).

In the present report sound pressure levels L_{Amax}, L_{Aeq} and $L_{\mathrm{A}}\,1$ were measured and spectral analysis in 1/3-octave bands was performed on short selections from performances of music students during their training sessions. The same music selections were used in computation of Cumulative Distribution Functions. Effects of exposure to music noise were determined by comparison of resting audiograms and TTS_2, i.e. threshold 2 min after cessation of the exposure. Estimation of the hearing loss risk in sound exposure of music students playing wind instruments was the aim of this investigation.

2. Procedure and apparatus

Sound pressure level measurements were performed using Bruel&Kjaer precision sound level meter type 2230 which was positioned 1 m from the output aperture of the musical instrument. Readings were taken during actual training sessions and then for chromatic scales fast played over the whole range of the instrument and during short music selections chosen by the performer. Readings were taken 10 times at 2-min intervals during routine training sessions at the Academy of Music. An average of 10 readings for each pressure value measured was taken as characteristic for the given instrument and given performer.

Chromatic scales fast played at the same level over the whole range of the instrument and short (duration 60 s) music selections were recorded on tape using NAGRA IV-SJ recorder and precision omnidirectional condenser microphone B&K type 4133 placed 1 m from the instrument. Long time average spectra analysis in 1/3 octave bands in the frequency range from 20 Hz to 20 kHz were determined for such samples using B&K analyser type 2144. A-weighted levels L_{Aeq} and $L_{\mathrm{A}}\,1$ for the whole range of frequencies

are also given. LTAS correspond to the sound pressure levels averaged over the duration of performance. Statistical measures L_A 1 correspond to the sound levels, which were present in 1% of the duration of the analysis. Exponential averaging with time constant 1/124 s was used.

Resting hearing thresholds 48 hrs without exposure and shifted thresholds 2 min after cessation of the exposure of 4 hrs duration were measured with the use of clinical audiometer Interacoustics type AC-40 equipped with headphones Telephonics TDH 39P with cushions MX-41/AR, in connection with HP Vectra 486 33U personal computer. Audiometric testing was executed on a sample of 14 representatives of most exposed brass and woodwind sections. HTL(246) indicator was used to determine TTS_2. Only wind instrument data are given in the present report.

3. Results and discussion

The sound pressure level and its spectral and temporal structure depend, as it is known, on the instrument, the performer and also on the type of music. Years of observation of music students training and sound pressure level measurements during training sessions indicated, that particularly in brass and woodwind instruments the sound pressure levels generated are far beyond the SPL's measured in LTAS records for symphonic orchestras. This observation is confirmed by the present investigation. Maximum and equivalent sound pressure levels measured and calculated are represented in cumulative distribution functions and in the LTAS functions. Six examples of these functions obtained for trumpet, trombone, horn, french horn, clarinet and piccolo, are given in Fig. 1 to Fig. 6.

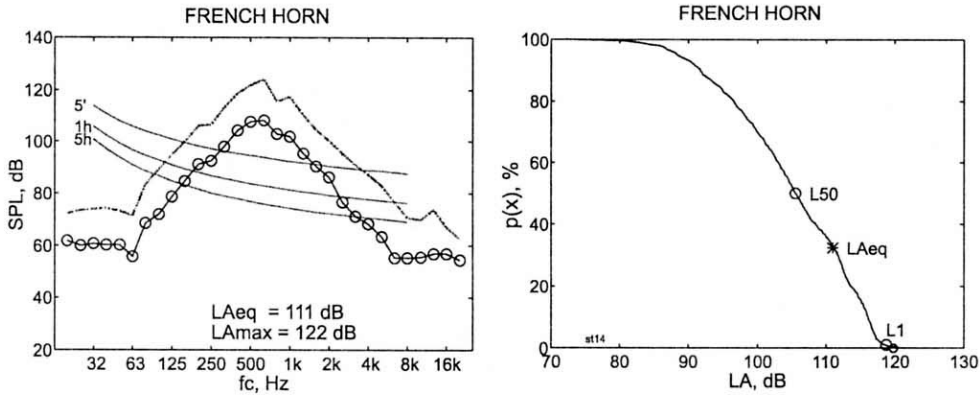

Fig. 1. Long time average spectra and cumulative distribution functions for french horn in typical routine training sessions by music students.

Statistical measures L_A 1 and equivalent sound levels L_{Aeq} for these instruments are given in Tab. 1 for easy comparison. It can be easily observed that the data obtained are well beyond the values measured by various researchers in symphonic orchestras.

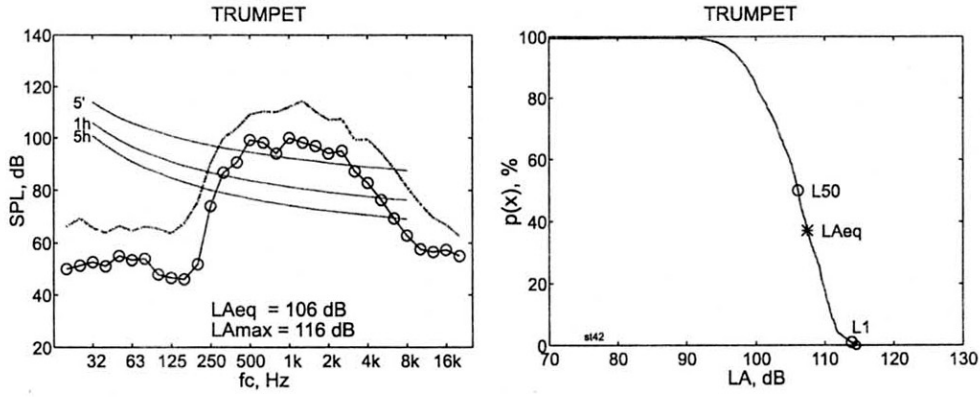

Fig. 2. Long time average spectra and cumulative distribution functions for trumpet in typical routine training sessions by music students.

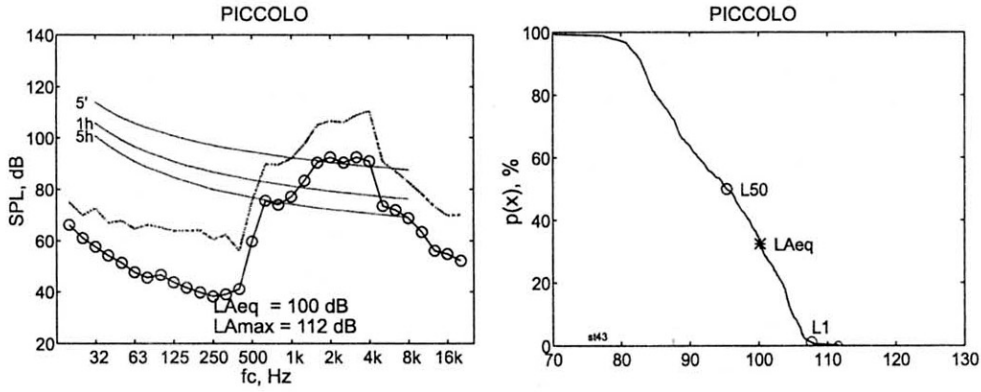

Fig. 3. Long time average spectra and cumulative distribution functions for piccolo flute in typical routine training sessions by music students.

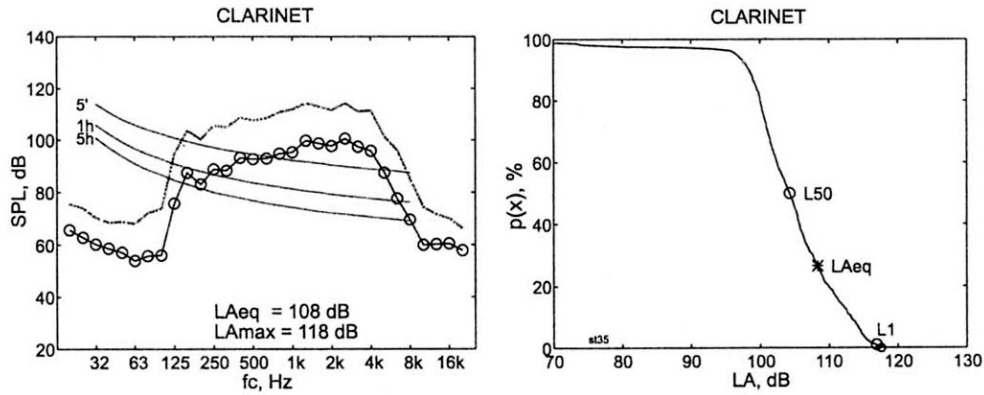

Fig. 4. Long time average spectra and cumulative distribution functions for clarinet in typical routine training sessions by music students.

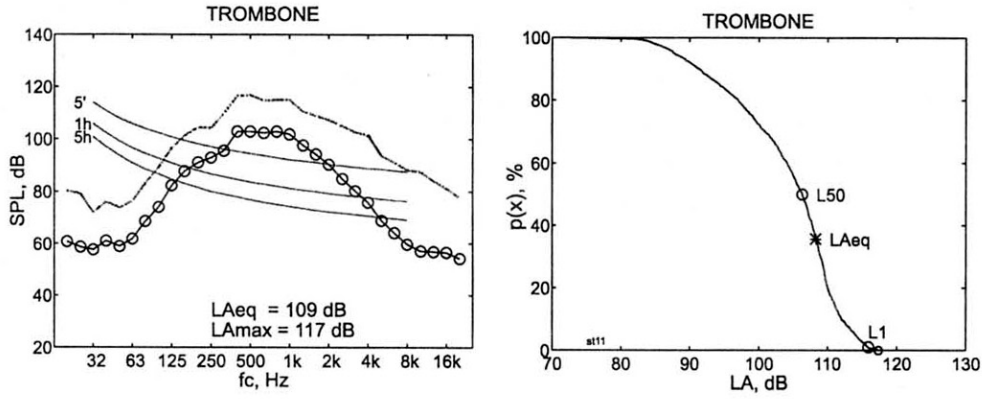

Fig. 5. Long time average spectra and cumulative distribution functions for trombone in typical routine training sessions by music students.

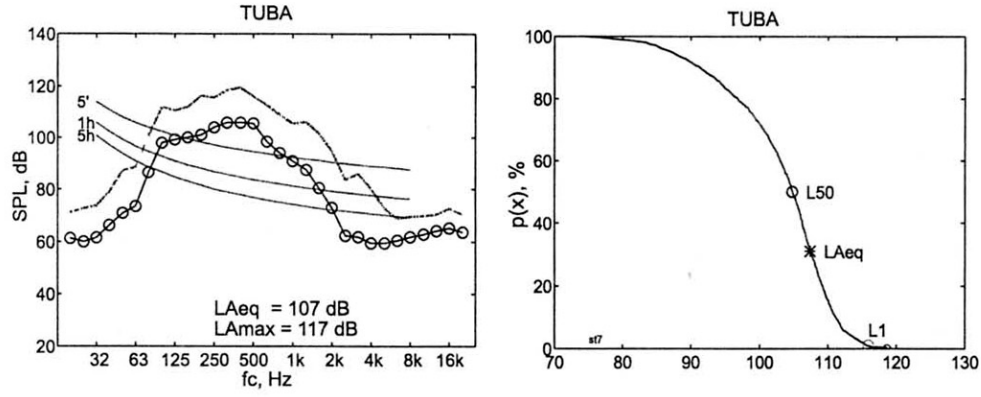

Fig. 6. Long time average spectra and cumulative distribution functions for tuba in typical routine training sessions by music students.

Table 1. Statistical measures L_A 1 and equivalent sound pressure levels L_{Aeq} for wind instruments in typical routine training sessions by music students.

Instrument	french horn	tuba	trumpet	trombone	piccolo	clarinet
L_A 1, dB	119	116	114	116	107	117
$L_{A\,eq}$ 1, dB	111	107	106	109	100	108

Consequently, temporary threshold shifts following exposures experienced in training sessions are substantial. In 50% of performers notch shaped audiograms were found with permanent selective loss of 10 dB to 30 dB at 6 kHz and comparatively less at adjacent frequencies. The amount of TTS_2 reached 30 dB in some cases resulting in HTL 40 dB, see for example audiogram of the subject PM playing trumpet Fig. 7.

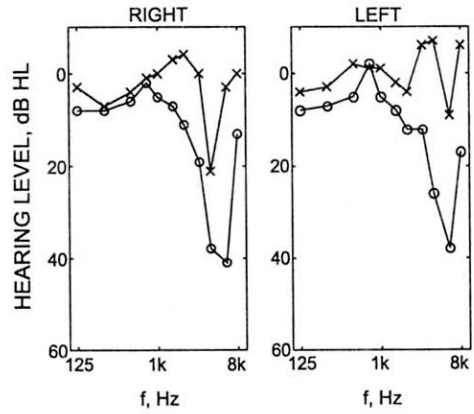

Fig. 7. Resting hearing threshold and TTS_2 for music student playing trombone after 4 1/2 hrs of training.

Resting hearing levels and TTS_2 in the tested sample of 14 music students, after 4 – 4 1/2 hrs of training in the group of 8 – 12 persons are presented in Fig. 8. While the averaged threshold shift value is around 15 dB over the range of frequencies between 1 and 6 kHz, the data show large intersubject variability. Thus in some cases the individual TTS_2 reaches 20 dB at least in one ear. The threshold in quiet in the tested sample of 14 students also shows significant decrease of sensitivity. While the averaged data lie within permissible limits spare for the 26 dB V-dip at 6 kHz, some students show substantial amount of permanent threshold shift.

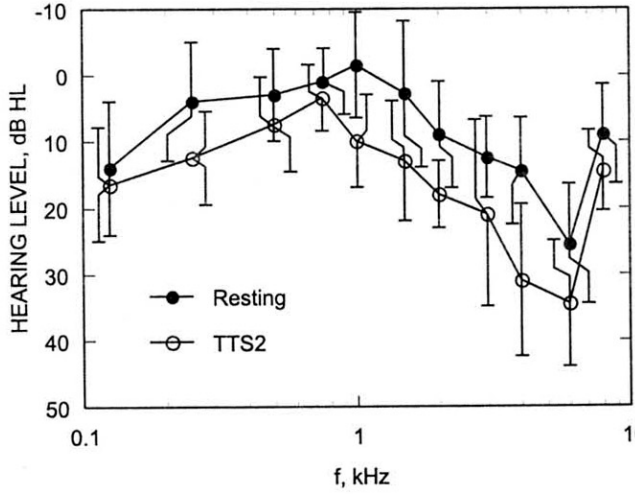

Fig. 8. Averaged resting hearing thresholds and averaged TTS_2 for a group of 14 music students playing wind instruments (both ears). Vertical bars represent standard deviations.

4. Conclusion

Present findings indicate that the exposures experienced by music students during their training sessions are far in excess relative to the permissible doses. Maximum measured values of sound levels are substantially higher than maximum levels observed by other researchers except for ROYSTER *et al.* [15], who recorded in orchestra A-weighted sound levels reaching 140 dB while "*the great majority of peak SPL's were in the range 115 - 129 dB (A)*".

Predictably, such exposures lead to aggregation of NIPTS if acquired over a long period of time and as such should not be ignored. In 50% of brass and woodwind players PTS of 10 dB to 20 dB was found which could be explained only by acoustic trauma.

Acknowledgement

This work was supported by Grant No. 4 S404 041 07 from The State Committee for Scientific Research. The body of this paper was presented to OSA'97 conference.

References

[1] A. AXELSSON, F. LINDGREN, *Hearing in classical musicians*, Acta Otolaryngologica, Supplement, **377**, 3–74 (1981).

[2] J. CAMP, S.W. HOTSTMAN, *Report on sound levels for Seattle Symphony Orchestra by School of Public Health and Environmental Medicine*, University of Washington, Seattle, WA (1987).

[3] B. HAY, *EEC directives on noise in the environment*, [in:] The Noise Handbook, W. TEMPEST [Ed.], Academic Press, 377–398, London 1985.

[4] D. HENDERSON, R.P. HAMMERNIK, *Impulse noise: a critical revue*, Journal of the Acoustical Society of America, **80**, 569–584 (1986).

[5] E. JANSSON, A. AXELSSON, F. LINDGREN, K. KARLSSON, T. OLAUSSEN, *Do musicians of the symphony orchestra become deaf?*, [in:] Acoustics for Choir and Orchestra, S. TERNSTROEM [Ed.], Royal Academy of Music, Stockholm 1986.

[6] E. JANSSON, K. KARLSSON, *Music acoustics-sound levels and long time spectra recorded within the symphony orchestra and risk criteria for hearing loss*, STL-OPSR, 1/1982, 31–48 (1982).

[7] E. JANSSON, K. KARLSSON, *Sound levels recorded within the symphony orchestra and risk criteria for hearing loss*, Scandinavian Audiology, **12**, 215–221 (1983).

[8] A. JAROSZEWSKI, *Wstępna ocena słuchu młodzieży akademickiej szkół muzycznych*, Prace Inst. Podst. Probl. Techniki PAN, XLII Otwarte Seminarium z Akustyki, Warszawa — Białowieża 12-15.09.1995 r., 491–496 (1995).

[9] A. JAROSZEWSKI, T. FIDECKI, P. ROGOWSKI, *Hearing damage from exposure to music*, Archives of Acoustics, **23**, 1, 3–31 (1998).

[10] A. JAROSZEWSKI, T. FIDECKI, P. ROGOWSKI, R. MONIAK, *Ekspozycja słuchaczy szkół muzycznych na wysokie poziomy dźwięku*, Prace Inst. Podst. Probl. Techniki PAN, XLII Otwarte Seminarium z Akustyki, Warszawa - Białowieża 12-15.09.1995 r., 497–502 (1995).

[11] D.W. JOHNSON, R.E. SHERMAN, J. ALDRIDGE, A. LORRAINE, *Extended high frequency hearing sensitivity: a normative threshold in musicians*, Annals of Otology Rhinology and Laryngology, **95**, 196–202 (1986).

[12] K. KARLSSON, P.G. LYNDQUIST, T. OLAUSSEN, *The hearing of the symphony orchestra musicians*, Scandinavian Audiology, **12**, 257–264 (1983).

[13] B. OSTRI, N. ELLER, G. SKYLV, *Hearing impairment in orchestral musicians*, Scandinavian Audiology, **18**, 243–249 (1989).

[14] J. RABINOWITZ, R. HAUSLER, G. BRISTOW, P. REY, *A study of the effect of loud music on musicians of the Orchestre de la Suisse Romande*, Medicine et Hygiene, [in:] Journal Suisse d'Informations Medicine, **19**, 1909–1921 (1982).

[15] J.D. ROYSTER, L.H. ROYSTER, M.C.V. KILLIAN, *Sound exposures and hearing thresholds of symphony orchestra musicians*, Journal of the Acoustical Society of America, **89**, 2793–2803 (1991).

[16] G. SCHACKE, *Sound pressure levels within an opera orchestra and its meaning for hearing*, 22nd International Congress on Occupational Health, Sydney, Australia 1987.

[17] G.A. WESTMORE, I.D. EVERSDEN, *Noise induced hearing loss in orchestral musicians*, Archives of Otolaryngology, **107**, 761–764 (1981).

[18] D. WOOLFORD, E.C. CARTERETTE, D.E. MORGAN, *Hearing impairment among orchestral musicians*, Music Perception, **5**, 261–284 (1988).

ARCHIVES OF ACOUSTICS
24, 2, 119–128 (1999)

HIGH FREQUENCY HEARING LOSS IN PERCUSSION PLAYERS

P. ROGOWSKI, A. RAKOWSKI and A. JAROSZEWSKI

Fr. Chopin Academy of Music
(00-368 Warszawa, Okólnik 2, Poland)

In a number of reports it has been observed that a prolonged exposure to music at sound pressure levels exceeding 100 dB leads to substantial temporary threshold shifts TTS_2, reaching 60–80 dB in the range of high frequencies. Cumulative effects of such exposures result in acoustic trauma, affecting the perception of pitch, loudness and time, accompanying the decrease of hearing sensitivity. The hearing threshold in percussion players is affected largely at high frequencies, where substantial decrease of sensitivity between 10 and 16 kHz reaching 40 to 75 dB has been observed. In the present report a number of hearing thresholds in percussion players and in control group consisting of musicians who have never played percussion instruments or were long exposed to their sounds have been analysed with reference to their exposure characteristics.

1. Introduction

There has been much concern over the past 30 years about the possibility of developing hearing loss by listening to loud music. Music was early recognised as a source of acoustic trauma (LEBO and OLIPHANT [16]). Its effects on hearing were studied with reference to the exposures experienced by listening to the rock and roll music, attending to the discotheques, listening to the portable CC and CD players and portable radios and with reference to the exposures experienced by orchestral (WOOLFORD *et al.* [24], AXELSSON and LINDGREN [1], ROYSTER *et al.* [19], JANSSON and KARLSSON [10], GRYCZYŃSKA and CZYŻEWSKI [6], JAROSZEWSKI *et al.* [12]) and rock and roll musicians (AXELSSON and LINDGREN [3], AXELSSON *et al.* [1], AXELSSON and LINDGREN [2], JAROSZEWSKI *et al.* [11], JAROSZEWSKI and RAKOWSKI [13]).

Early studies of the effects of exposure to music on hearing in musicians by GRYCZYŃSKA and CZYŻEWSKI [6] show substantial impairment of hearing. In 68% of the tested sample of 51 orchestral musicians music noise induced hearing loss was observed, while largest hearing loss was found in percussion players. In a study by AXELSSON and LINDGREN [4], noise induced hearing loss from the exposure to music was found in 43% of the tested sample of 139. However, they found largest NIHL in bassoon and French horn players (mean NIHL: 30–35 dB) while only moderate (18 dB) in percussion players. These data are in some agreement with the early findings by JAHTO and HELLMAN [9] who found NIHL in 37% of the tested sample, ZELENÝ *et al.* [25] NIHL in 72% of the tested sample, by WOOLFORD *et al.* [24] 25 dB NIHL (61% of tested ears) by WESTMORE and

EVERSDEN [23] 34% of 68 ears with NIHL, by OSTRI *et al.* [18] who measured HTL in 96 and found NIHL in 50% of males and 13% of females and with more recent findings by ROYSTER *et al.* [19] NIHL in 52.5% of the sample or by JAROSZEWSKI *et al.* [11] in 68% of the tested sample.

Contrasting data were also reported for example by KARLSSON *et al.* [15] who tested hearing threshold levels in 392 musicians, and found median values equivalent to the expected age-effect thresholds according to SPOOR [21]. Nevertheless, a dip at 6 kHz is present in median audiometric data, also in this report. It is thus apparent that no consensus exists on the effect of music exposure on hearing in musicians.

Summarising, almost all researchers arrived at the data that correspond to the noise induced hearing damage in some proportion of musicians tested. This proportion ranges from approximately 35% up to approximately 70% in most of the studies available in the literature. Spare for the study by GRYCZYŃSKA and CZYŻEWSKI [6] who found large HF sloping hearing loss up to 80 dB at 8 kHz in percussion players, hearing loss reported by other investigators were not so large e.g. 30 dB in AXELSSON and LINDGREN [4] or 26.5 and 25.0 dB at 4 and 6 kHz (SD $\cong$ 20 dB) correspondingly, for the instrument group including percussion in the study by ROYSTER *et al.* [19]. No data is available on hearing in percussion players for frequency range above 8 kHz. The present work reports the experimental data on hearing impairment found in young percussion players in the whole range of audiometric frequencies, with special attention to high frequencies above 8 kHz. The aim of this research was to test the hypothesis that percussion players and particularly xylophone players experience severe hearing impairment in the range of high and very high frequencies due to exposure to impulse music noise.

2. Procedure and equipment

Two groups, each consisting of 40 young musicians (up to 26 years), an experimental group playing percussion and often xylophone, and control group playing other instruments i.e. strings, woodwinds, brasswinds and piano were used as subjects. Average age in both groups was 21 years.

Hearing threshold in quiet was measured in both ears in both groups with the use of electronically controlled audiometer Interacoustics AC 40 connected to a PC HP Vectra which performed data acquisition and data analysis. Air conduction pure tone audiometry with intermittent 250/250 ms signal and 1 dB step level control was used throughout. Tests were performed at 11 frequencies in the low frequency range and at two frequencies in the high frequency range. Headphones TDH 39P with MX41/AR cushions were used in low frequency range and Koss HV/PRO with circumaural cushions in high frequency range.

In an attempt to relate the specific audiometric data with spectral and temporal characteristics of xylophone sounds, both spectral and temporal analyses were performed on samples of xylophone sounds. For spectral analysis short selections performed on a xylophone were recorded on Sony DAT recorder PCM 2300 using Brüel&Kjar 1/2″ condenser microphone type 4133. Spectral analyses were performed using Matlab software.

Temporal analysis included determination of the cumulative peak level distribution function for short selections performed on a MUSSER KELON 42 xylophone and measurements of signal onset times for the entire xylophone scale. This was done with the use of B&K 1/4″ condenser microphone type 4135 with measuring amplifier B&K 2607 connected to digital oscilloscope HP 54501A which memorised single signals for precision graphic measurements. Spectral analysis was performed also on these signals to eliminate the effects of limited frequency response of recording channel of DAT.

3. Results

Hearing threshold data of young percussion players are presented in Fig. 1 as mean of 80 audiograms for left and right ears and standard deviations in the experimental group. Hearing threshold data for musicians not exposed to percussion sounds, i.e. for control group are given in Fig. 2 also as mean of 80 audiograms and standard deviations in the group. The largest differences between the means of two data sets amount to 9.1 dB at 12.5 kHz and to 24.3 dB at 16 kHz. The analysis of audiometric data for the experimental and control groups is shown in Fig. 3 and Fig. 4. The results of measurements of onset times for the entire xylophone scale show that the onset time is quite small amounting to approximately 10 μs. Examples of xylophone sound C#6 (1108.8 Hz) oscillograms obtained with various time bases are given for illustration in Fig. 5.

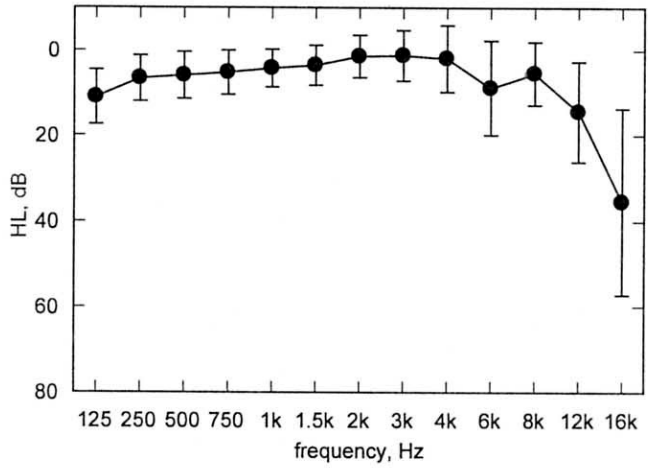

Fig. 1. Hearing threshold level in quiet in percussion players. Means and standard deviations of 80 audiograms; right and left ears.

The results of spectral analysis of the first 5 ms of one representative isolated xylophone sound C5 (523.3 Hz) obtained from the recorded material are given in Fig. 6. It shows maximum sound pressure level spectral density within the range of relatively low frequencies between 500 and 8000 Hz, decreasing towards high frequencies. However, it should be observed that while at low frequencies the peak density reaches 106 dB it

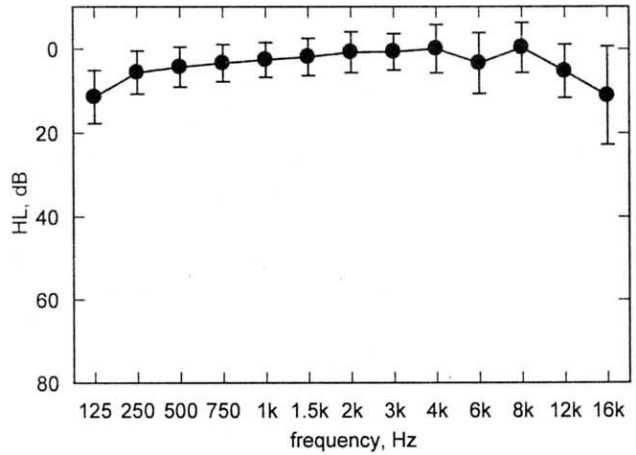

Fig. 2. Hearing threshold level in quiet in non-percussion players. Means and standard deviations of 80 audiograms; right and left ears.

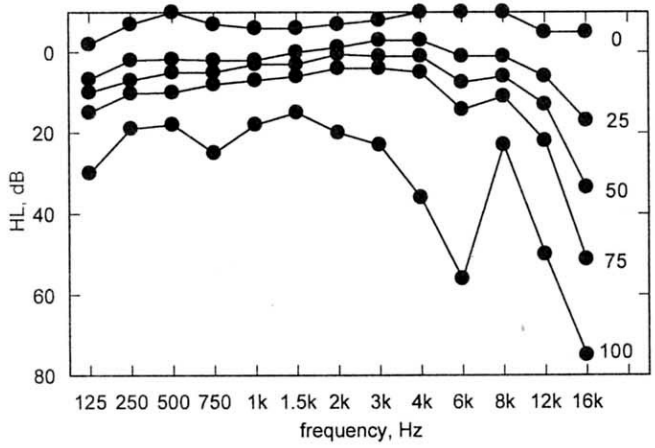

Fig. 3. Statistics of threshold in quiet in percussion players. Quartiles of 80 audiograms; right and left ears.

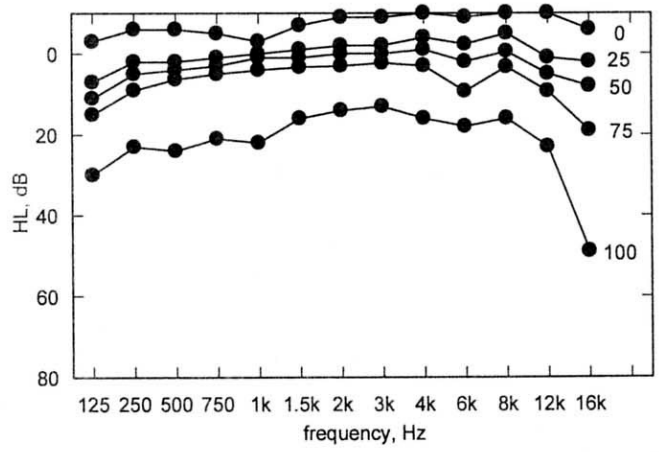

Fig. 4. Statistics of threshold in quiet in non-percussion players. Quartiles of 80 audiograms; right and left ears.

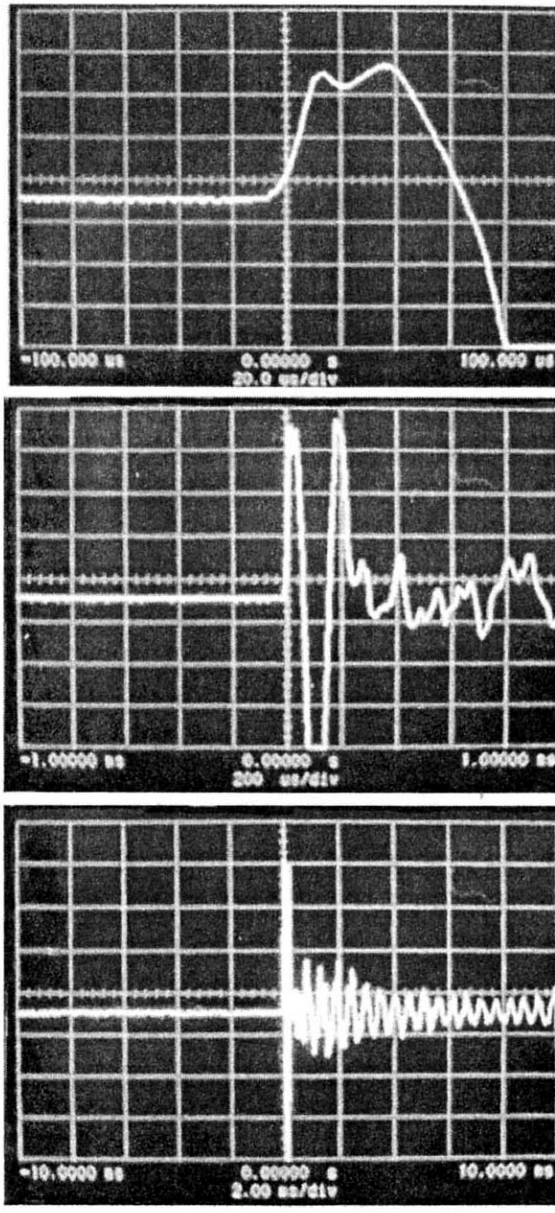

Fig. 5. Examples of oscillograms of isolated xylophone sound C#6 (1108.8 Hz) with time bases 20 μs/div, 200 μs/div and 2 ms/div.

decreases at high frequencies only by 25 dB. It means that at 20 kHz the peak spectral density is still in the range of 80 dB. The results of temporal analysis of the short selections performed on a xylophone, in the form of the cumulative distribution function are given in Fig. 7. These data show some amount of peaks reaching 140 dB.

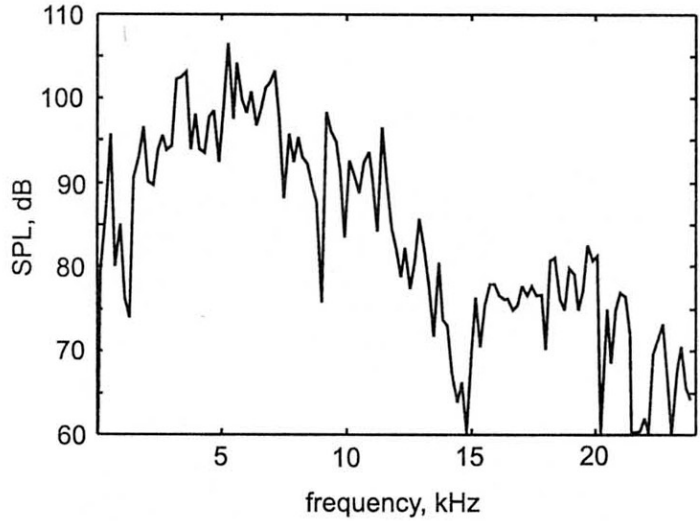

Fig. 6. Amplitude spectrum of representative isolated xylophone sound C5 (523.3 Hz).

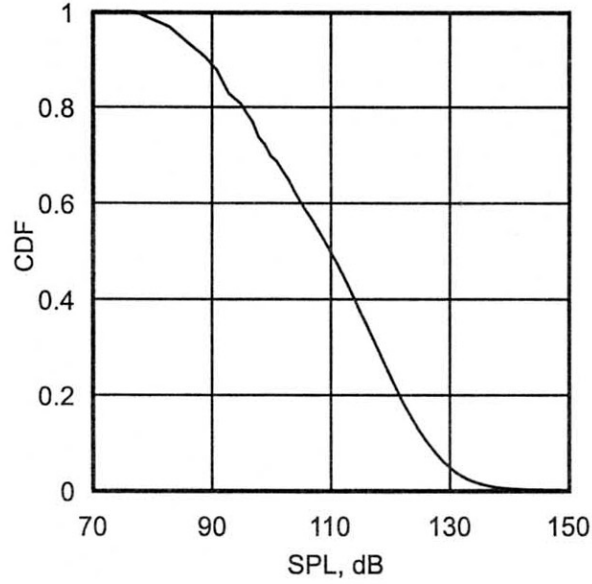

Fig. 7. Peak level cumulative distribution function (CDF) of short selection played on the xylophone.

Temporal analysis of xylophone sound models was performed to test the effect of limited frequency response of DAT recording channel. A number of C#6 (1108.8 Hz) sound samples recorded in digital oscilloscope memory with different time bases were resampled and merged into one structure. Sampling frequency was 192 kHz. This xylophone sound model was then low-pass filtered and resampled with standard DAT sampling frequency — 48 kHz. The shapes of initial transients in both cases are shown in Fig. 8.

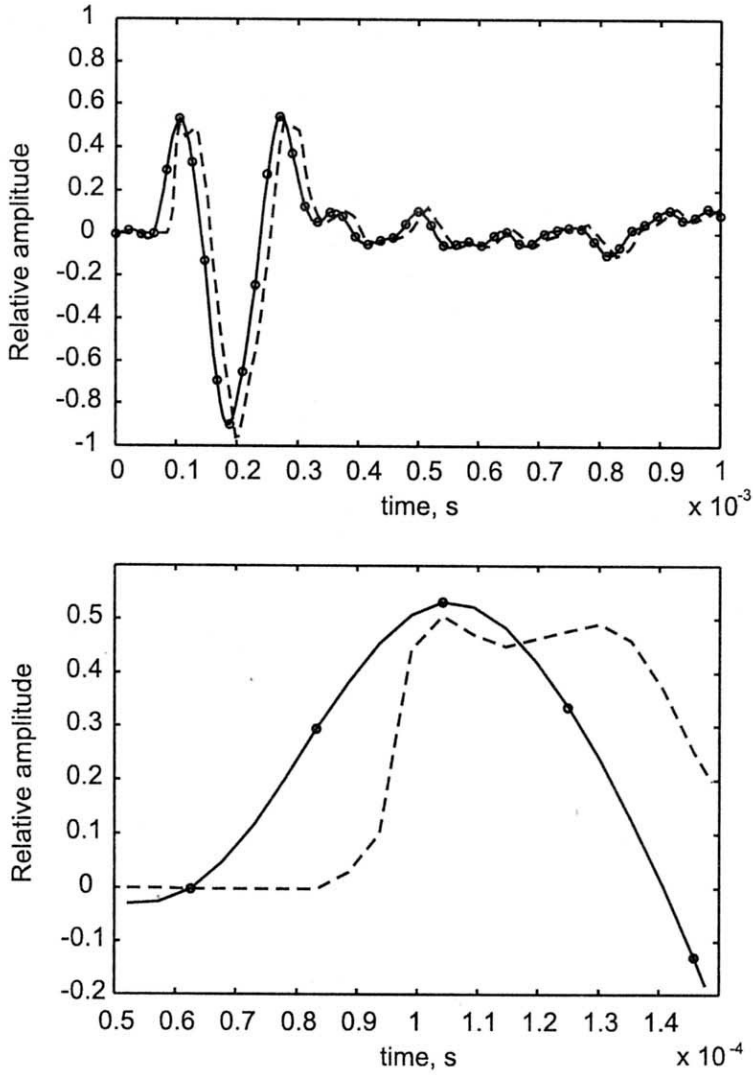

Fig. 8. Initial transients of xylophone sound C#6 (1108.8 Hz) models digitally recorded with sampling frequency 48 kHz (solid line) and 192 kHz (dashed line).

4. Discussion

The experimental data on hearing impairment in percussion players is in partial agreement with the early data from GRYCZYŃSKA and CZYŻEWSKI [6], from KARLSSON *et al.* [15] and from OSTRI *et al.* [18] who found substantial hearing loss in percussion players, but who used conventional LF audiometry up to 8 kHz only. Contrasting results were reported by OSTERHAMMEL and OSTERHAMMEL [17] who compared hearing thresholds in 286 normal hearing subjects and 28 noise exposed subjects with typical 4 – 6 kHz

V-dip. Their data show that in all age groups (30–39, 40–49, 50–59) thresholds reach normal values at very high frequencies, even for subjects with severe impairment at low frequency. However it should be stressed that no details are available as to what noise their subjects were exposed to, spare for information that it was industrial noise.

Histological examination of cochlea in man and in animals shows that impulsive sounds cause damage particularly in the basal end of cochlea i.e. place of location of high frequency receptors, HAWKINS and JOHNSON [8], JORDAN *et al.* [14], SONDIJN [20]. It is beyond any doubt that small rise times of percussion sounds give more energy in the high frequency range of their spectral density than any other musical instrument does. This results in increased excitation and consequently damages of auditory receptors in that range in case of exposure to very high sound pressure levels of percussion sounds reaching 140 dB SPL.

It should be observed that the exposure to "live" percussion sounds is evidently more dangerous to hearing because of very short rise times of sound pulses which are smoothed in the recorded material. This notion is in agreement with the early experimental evidence from WALKER and BEHAR [22] who found that impulse events recorded on tape lead to fairly less TTS than "live" pulse events. HAMERNIK *et al.* [7] suggest: "increasing of susceptibility to NIPTS from the lowest to the highest audiometric frequencies which further grows by 5 to 10 dB for pulses with spectral peak at high frequencies". This suggestion is in agreement with experimental data from FAUSTI *et al.* [5] who measured high frequency thresholds in subjects exposed to impulsive noise (gunfire) and found large thresholds shifts above 8 kHz.

5. Conclusions

From the experimental evidence it is apparent that percussion sounds have quite destructive effect on hearing. The particularly dangerous effect results from very rapid onset of some percussion sounds, like these of xylophone. Such an effect is not present in any other musical instrument. The net effects of the exposure to percussion sounds manifest themselves in the significantly worse hearing threshold in percussion players relative to the control group of other musicians.

Acknowledgements

The work was supported by Grant No 4 S404 041 07 and Grant T 07B 051 15 from the State Committee for Scientific Research. Parts of this paper were presented to Noise Control'98 conference.

The authors work to express their gratefulness to Prof. S. Skoczyński and to his students for their voluntary participation in the present research.

References

[1] A. AXELSSON, T. JERSON, U. LINDBERG, F. LINDGREN, *Early noise-induced hearing loss in teenage boys*, Scandinavian Audiology, **10**, 91–96 (1981).

[2] A. AXELSSON, F. LINDGREN, *Does pop music cause hearing damage*, Audiology, **16**, 432–437 (1977).

[3] A. AXELSSON, F. LINDGREN, *Hearing in pop musicians*, Acta Otolaryngologica, **85**, Stockholm, 225–229 (1978).

[4] A. AXELSSON, F. LINDGREN, *Hearing in classical musicians*, Acta Otolaryngologica, Supplement, **377**, 261–284 (1981).

[5] S.A. FAUSTI, D.A. ERICKSON, R.H. FREY, B.Z. RAPPAPORT, *The effect of impulsive noise upon human hearing sensitivity* (8–20 kHz), Scandinavian Audiology, **10**, 21–29 (1981).

[6] D. GRYCZYŃSKA, I. CZYŻEWSKI, *Uszkadzający wpływ muzyki na narząd słuchu u muzyków*, Otolaryngologia Polska, **31**, 527–531 (1977).

[7] R.P. HAMERNIK, W.A. AHROON, K.D. HSUEH, *The energy spectrum of an impulse: its relation to hearing loss*, Journal of the Acoustical Society of America, **90**, 197–204 (1991).

[8] J.E. HAWKINS, L.G. JOHNSON, *Patterns of sensorineural degeneration in human ears exposed to noise*, [in:] Effects of Noise on Hearing-Critical Issues, R.P. HAMERNIK *et al.* [Eds.], Raven, New York, 91–92 (1976).

[9] K. JAHTO, H. HELLMAN, *Zur Frage des Lärm – und Klangtraumas des Orchestermusikers*, HNO, **20**, 21–29 (1972).

[10] E. JANSSON, K. KARLSSON, *Sound levels and long-time spectra recorded within the symphony orchestra and risk criteria for hearing loss*, STL-QPSR, 1/1982, 31–48, Huddinge Sjukhus, Dept. of Audiology, Stockholm 1982.

[11] A. JAROSZEWSKI, T. FIDECKI, P. ROGOWSKI, *Hearing damage from exposure to music*, Archives of Acoustics, **23**, 1, 3–31 (1998).

[12] A. JAROSZEWSKI, T. FIDECKI, P. ROGOWSKI, *Exposures and hearing thresholds in music students due to training sessions*, Prace XLIV OSA, Gdańsk – Jastrzębia Góra 15–18.09.1997, PTA Oddz. Gdański (Ed.), Vol. 1, 343–348 (1997).

[13] A. JAROSZEWSKI, A. RAKOWSKI, *Loud music induced threshold shifts and damage risk prediction*, Archives of Acoustics, **19**, 311–321 (1994).

[14] V. JORDAN, M. PINHEIRO, K. CHIBA, A. JIMENEZ, *Cochlear pathology in monkeys exposed to impulse noise*, Acta Otolaryngologica, Stockholm, Supplement, **312** (1973).

[15] K. KARLSSON, P. LUNDQUIST, T. OLAUSSEN, *The hearing of the symphony orchestra musicians*, Scandinavian Audiology, **12**, 257–264 (1983).

[16] P.CH.LEBO, K.P. OLIPHANT, *Music as a source of acoustic trauma*, Laryngoscope, **78**, 1211–1218 (1968).

[17] D. OSTERHAMMEL, P. OSTERHAMMEL, *High frequency audiometry and noise-induced hearing loss*, Scandinavian Audiology, **8**, 85–91 (1979).

[18] B. OSTRI, N. ELLER, G. SKYLV, *Hearing impairment in orchestral musicians*, Scandinavian Audiology, **18**, 243–249 (1989).

[19] J.D. ROYSTER, L.H. ROYSTER, M.C. KILLIAN, *Sound exposures and hearing thresholds of symphony orchestra musicians*, Journal of the Acoustical Society of America, **89**, 2793–2803 (1991).

[20] E.R. SONDIJN, *Scanning electron microscope study of the organ of Corti in normal and sound damaged guinea pigs*, Annals of Otolaryngology, St Louis, 85, Supplement, **29** (1976).

[21] A. SPOOR, *Presbycusis values in relation to noise-induced hearing loss*, International Audiology, **6**, 48–57 (1967).

[22] I.G. WALKER, A. BEHAR, *Limitations in the use of tape recording for impulse noise measurement and TTS_2 studies*, Proc. 7th ICA, Budapest, Vol. 3, 417–420 (1971).

[23] G.L. WESTMORE, I.D. EVERSDEN, *Noise - induced hearing loss in orchestral musicians*, Archives of Otolaryngology, **107**, 761–764 (1981).

[24] D. WOOLFORD, E.C. CARTERETTE, D.E. MORGAN, *Hearing impairment among orchestral musicians*, Music Perception, **5**, 261–284 (1988).

[25] M. ZELENÝ, Z. NAVRÁTILOVÁ, Z. KAMÝČEK, *Relation of hearing disorders to the acoustic composition of working environment of musicians in a wind orchestra*, Otolaryngology (Cs), **24**, 295–299 (1975).

ARCHIVES OF ACOUSTICS
24, 2, 129–144 (1999)

ACOUSTIC AND MAGNETIC PROPERTIES OF MAGNETIC LIQUIDS

A. SKUMIEL, T. HORNOWSKI and A. JÓZEFCZAK

Institute of Acoustics
Adam Mickiewicz University
(60-769 Poznań, Matejki 48/49)
e-mail: skumiel@main.amu.edu.pl

The influence of magnetic field on the acoustic and magnetic properties of magnetic liquids is discussed. By fitting the curve of Taketomi's theory to the experimental data of the anisotropy of ultrasonic attenuation, the values of quantities describing the structure of magnetic liquid have been determined. Moreover, the dependence of magnetic susceptibility on frequency has been measured. It shows that two processes of magnetization, which are based on the mechanisms proposed by Brown and Néel, contribute to the magnetization of the EMG-605 magnetic liquid.

1. Introduction

Magnetic liquids do not exist in nature. They owe their existence to recent developments in the technology of materials and the concomitant applications in the computer technique, medicine, modern military setups, as well as in the instruments of every-day usage.

In this paper an attempt is made to elucidate the influence of an external magnetic field on the propagation of ultrasonic waves and the magnetic properties of magnetic liquids. The field gives rise to anisotropy: the liquid undergoes restructurization by the formation of spherical and chain-like clusters. As a result, the absorption of the wave undergoes an enhancement due to the rotational and translational motions of the clusters.

Moreover, it was our aim to determine which of those mechanisms predominates under different external conditions and to gain as much information as possible concerning the structure of magnetic liquids, in particular concerning the radius of the spherical clusters and their concentration. A magnetic liquid is defined as a colloid suspension of magnetic particles in a carrier liquid (water, mineral oil, or an organic compound). The radii of magnetic particles (grains) typically range from 5 to 10 nm. They are involved in Brownian motion, and their smallness considerably restricts the natural process of gravitational sedimentation.

Coagulation of the individual magnetic particles leads to a restructurizarion of the magnetic liquid. Spherical clusters arise with radii ranging from some tens of nanometers

up to several micrometers as well as chain-like clusters that can be observed by a microscope. In the external magnetic field the chain-like clusters array themselves along the lines of the field increasing the stiffness of the liquid and modyfying its acoustic properties. The size of the spherical clusters as well as the length of the chains they form are primarily dependent on the magnetic field strength and the temperature. The magnetic liquid EMG-605, which was studied by authors, consisted of water (as the carried liquid) and suspended particles of $FeO \cdot Fe_2O_3$ with diameters of about 20 nm. Thus, we dealt with a colloidal solution having a high degree of dispersion and containing polydisperse ferrimagnetic particles endowed with an intrinsic magnetic moment.

In the majority of magnetic liquids the state of magnetization is rather well described by the Langevin's law for the magnetization of molecules of a paramagnetic gas. However, in magnetic liquids the effective state of magnetization of the sample in the external magnetic field often sets in the way of two concomitant mechanisms of restructurization of the magnetic moments of the solid particles: one is that of magnetization relaxation related to the Brownian rotation of the particles in the carried liquid, whereas the other one consists in thermal fluctuations of the magnetic moment within the particle itself.

2. Characteristic of magnetic liquids

2.1. Static magnetic properties

The dispersive phase of magnetic liquids consists of ferri- or ferromagnetic particles that undergo strong magnetization already in rather weak fields. In condensed ferromagnetics, there arise elementary regions of spontaneous magnetization — domains in that the spontaneous magnetization attains saturation.

The external magnetic field reorients the elementary magnetic moments in the sample, so that it exhibits magnetization.

When the field is switched off, the magnetization M of the system of particles tends to zero due to the thermal motion of the magnetization vectors $\mathbf{m}$ of the individual particles.

The time-dependent decrease of M obeys the law of exponential decay [1],

$$M = M_\infty \exp\left(-\frac{\tau}{\tau_N}\right), \tag{1}$$

where τ_N is *the relaxation time of magnetization* due to the mechanism proposed by Néel. In accordance with the model of discrete orientation of the vector $\mathbf{m}$, the Néel relaxation time τ_N is given by the following equation [1, 2]:

$$\tau_N = \tau_0 \exp\left(\frac{K_1 V}{kT}\right), \tag{2}$$

where τ_0 — time of Larmor precession of the vector $\mathbf{m}$ around the anisotropy axis, K_1 — anisotropy constant of the single crystallographic axis, V — mean volume of the magnetic particle, kT — thermal energy of the magnetic particle.

In this case, the magnetic moment can change its direction within an immobile magnetic grain overcoming the energy barrier K_1V.

For magnetite Fe_3O_4, a component of the magnetic liquid EMG-605 studied by us, the parameter $K_1 = 11\,\mathrm{kJ/m^3}$. For the mean radius of a single magnetic particle $r = 10\,\mathrm{nm}$, which corresponds to a mean volume of $4.2 \cdot 10^{-24}\,\mathrm{m^3}$, we get for the potential energy $4.6 \cdot 10^{-20}\,\mathrm{J}$.

The time τ_0 results from the Larmor precession of the vector $\mathbf{m}$ around the anisotropy axis; various authors [2, 3] have assumed $\tau_0 \simeq 10^{-9}\,\mathrm{s}$. With this in mind, and at $T = 293\,\mathrm{K}$, the Néel magnetization relaxation time can be assessed at $\tau_N = 98\,\mu\mathrm{s}$.

The intensity of Brownian diffusion of the vector $\mathbf{m}$ is given by the energy kT.

The static state of the particle depends on the ratio of two parameters, $\sigma_N = K_1V/kT$ and $\xi = \mu_0 mH/kT$, which characterize the mutual relation between the energies of magnetic anisotropy and interaction with the external magnetic field and the energy of thermal motion. The numerator $\mu_0 mH$ means the magnetic energy of the magnetic particle with magnetic dipole moment $\mathbf{m}$ in the external magnetic field strength H; μ_0 is the permeability of the free space and has the value of $4\pi \cdot 10^{-7}\,\mathrm{H/m}$.

If $K_1V \ll kT$ and $K_1V \ll \mu_0 mH$, the orientation of the vectors $\mathbf{m}$ of the individual particles varies randomly about the field vector under the action of thermal fluctuations which damp the resultant field.

The relaxation time τ_N is the decay time of the Larmor precession τ_0 of the magnetic moment. In this case, the crystallographic anisotropy can be neglected, the external symptoms of a ferromagnetic material vanish, and the hysteresis loop goes over into a simple magnetization curve ($B_r = 0$ and $H_c = 0$) which obeys the Langevine law,

$$M = M_s \left(\coth \frac{\mu_0 mH}{kT} - \frac{kT}{\mu_0 mH} \right). \tag{3}$$

In this case B_r and H_c mean remanence and coercivity of the material, respectively, whereas M_s is the magnetization at $H \to \infty$.

As mentioned above, the colloidal particles of a ferro- or ferrimagnetic material possess a magnetic moment of constant magnitude dependent on the magnetization M_s and the volume V of the particle. The external magnetic field alignes the magnetic moments, leading to magnetization on a macroscopic scale in the sample.

The orientation of the magnetic moments of the colloidal particles proceedes according to two mechanisms:

(i) Inside the monoaxial particle of the solid, thermal reorientation of the magnetic moment takes place between two opposite directions of the easy magnetization axis of the crystal.

(ii) The particles undergo rotation with respect to the carrier as a result of thermal motion.

In the absence of a magnetic dipole interaction between monodisperse colloidal particles, the magnetic state of the medium is described by the classical law derived by Langevin for the magnetization of molecules of a paramagnetic gas,

$$\frac{M}{M_\infty} = \frac{M}{M_s \phi_M} = \coth \xi - \frac{1}{\xi} \equiv L(\xi), \tag{4}$$

with ϕ_M the volume concentration of the magnetic material and $\xi = \mu_0 mH/kT$ the argument of the Langevin function $L(\xi)$.

For spherical particles of diameter d, the argument of the Langevin function takes the form: $\xi = \pi\mu_0 M_s H d^3/6kT$.

Figure 1 shows the Langevin function $L(\xi)$ *versus* the external magnetic field strength H for spherical magnetic particles with radii of 2.5 nm, 5 nm and 10 nm. We assumed the following values for the magnetization saturation $M_s = 478\,\mathrm{kAm^{-1}}$ and the volume concentration $\phi_M = 3.5\%$ which correspond to the magnetic liquid EMG-605 used in our experimental work.

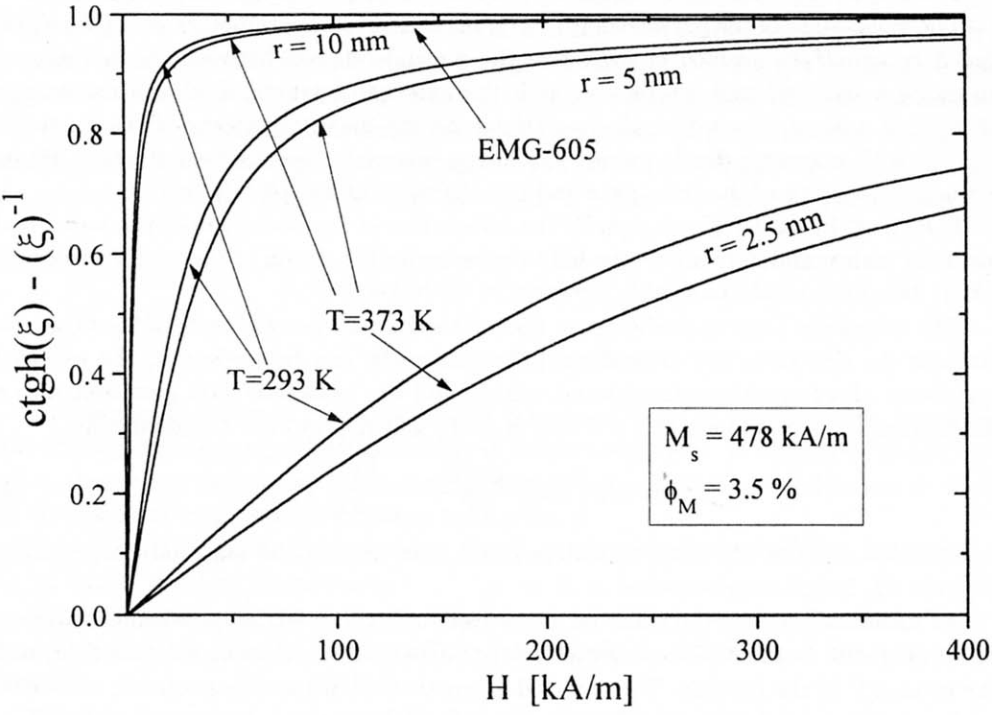

Fig. 1. Langevin function of magnetite magnetic liquids with magnetic grains of different radii *versus* the magnetic field strength at +20°C.

Figure 1 shows that the liquid achieves magnetic saturation at about $50\,\mathrm{kAm^{-1}}$, whereas the temperature affects the state of magnetization but weakly.

Now, real magnetic liquids have a well defined degree of polydispersion of the solid phase, causing some slight discrepancy between the experimental points and the magnetization curve plotted according to the Langevin's law [4]. This discrepancy is due mainly to the effect of larger particles.

Another property typical of systems of noninteracting single-domain particles is displayed by the simple $M(H/T)$ curve, i.e. by the lack of hysteresis of the magnetization.

The formation of aggregates in the magnetic liquid and the increase in the diameter of the monodisperse particles should affect the magnetization curve qualitatively.

With increasing mean diameter, an increase in the formation of aggregates is observed, the smaller particles tending to penetrate between the greater ones and leading to a packing of the aggregates that is more dense than that of a monodisperse system. The arisen aggregates cause an increase in the magnetization of the liquid of monodisperse particles, as well as an effect related to the increase of the effective size of the particles in the disperse phase.

2.2. The kinetics of magnetization

The process of magnetization of a magnetic liquid is ruled by two mechanisms:

(i) the mechanism of magnetization relaxation related to Brownian rotations of the particles in the carrier liquid,

(ii) the mechanism involving thermal fluctuations of the magnetic moments within the particles themselves.

Either of the processes is characterized by a specific relaxation time.

The Brownian rotational diffusion time of the colloidal particles is given by the expression [1, 5],

$$\tau_B = \frac{3V\eta_0}{kT}, \tag{5}$$

where η_0 is the dynamical viscosity of the carrier liquid, and V the hydrodynamic volume of the grain. Quite generally, the two mechanisms can run simultaneously when the external field is switched on, the magnetization vector of a given magnetic particle rotating at a greater velocity than the particle itself. In this case, the effective time constant of the magnetization process is smaller than both the components and can be determined from the following expression [1, 3, 5]:

$$\tau_{\text{eff}} = \frac{\tau_N \cdot \tau_B}{\tau_N + \tau_B}. \tag{6}$$

If $\tau_N \ll \tau_B$, the magnetization relaxation process is related to the Néel mechanism. If the opposite is the case ($\tau_N \gg \tau_B$), the equilibrium orientation of the magnetic moments sets in chiefly by the way of Brownian rotations of the particles.

The transition from one of the relaxation mechanisms to the other one can be found by comparing the expressions (2) and (5).

If the magnetic liquid with an aqueous carrier freezes (the magnetic particles are blocked), Brownian rotation will not occur ($\tau_B \nearrow \infty$). In this case the effective relaxation time of the magnetic susceptibility $\tau_{\text{eff}} = \tau_N$. These small single-domain magnetic particles are sometimes referred to as superparamagnetic. In this region of the radii, one of the mechanisms can predominate.

Figure 2 shows the effective relaxation time of the magnetic susceptibility *versus* the radius of a spherical particle of magnetite together with the two components originating in the respective mechanisms. The graph was plotted for a water-based magnetic liquid at 293 K. Obviously, for particles with a radius of about 8.7 nm the two mechanisms participate equally.

Moreover, it is assumed that in the liquid studied (EMG-605, $r = 10$ nm), the Brownian magnetization mechanism strongly predominates.

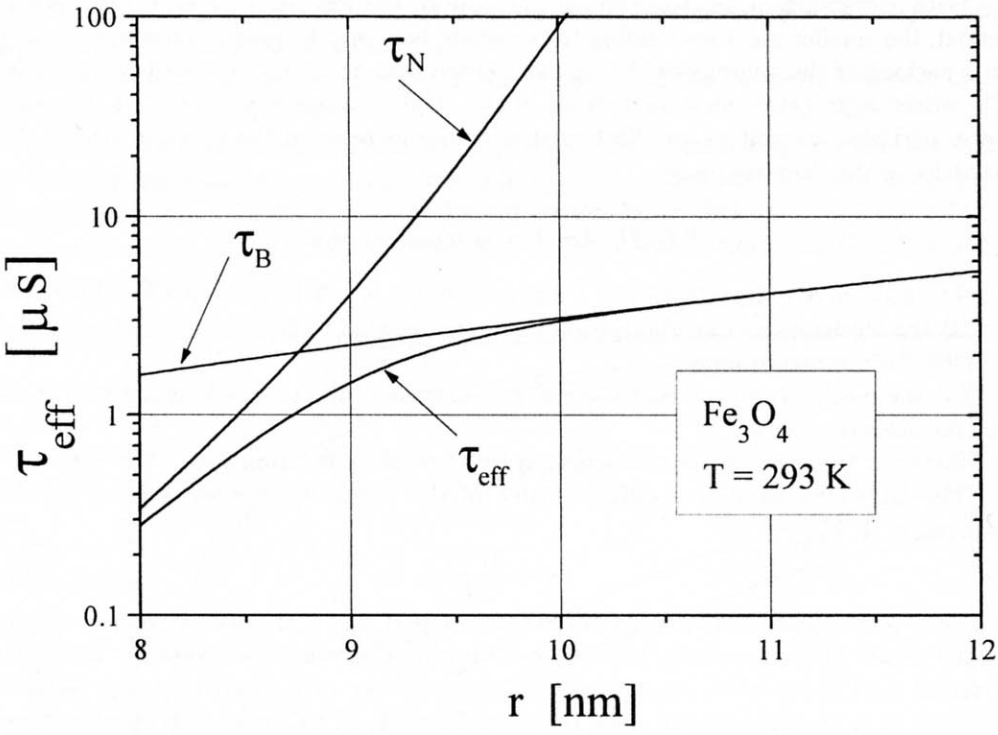

Fig. 2. Effective relaxation time of the magnetic susceptibility and its components *versus* the radius of a spherical magnetite grain at +20°C.

In this case, the effective relaxation time of the magnetic susceptibility $\tau_{\text{eff}} \simeq \tau_B$, since τ_B is about 30 times shorter than τ_N. However, it would suffice to use a magnetic liquid with smaller magnetic grains (say, with $r = 5\,\text{nm}$) and the system would magnetize according to the Néel's mechanism.

In reality, only a small portion of the grains in EMG-605 magnetizes according to the Néel mechanism because of its polydisperseness.

One of the methods of experimental determination of the characteristic relaxation times is to measure the complex magnetic susceptibility of the liquid with an AC magnetic field as a function of frequency. In such a field the magnetization undergoes a delay in phase with regard to the field strength, thus causing a change in the resultant magnetic moment that proceeds at a finite rate.

In sufficiently weak magnetic fields varying in time harmonically, the magnetic susceptibility can be written in the complex form [3, 6],

$$\tilde{\chi}(\omega) = \chi'(\omega) - i\chi''(\omega) = \chi_\infty + \frac{\chi_0 - \chi_\infty}{1 + i\omega\tau_0}\,, \tag{7}$$

where χ' — describes the reversible magnetization processes, χ'' — characterizes the processes of dissipation of the magnetic field energy, and $\omega = 2\pi f$ the angular frequency.

The time constant $\tau_0 = (2\pi f_m)^{-1}$ determines the frequency at which dissipation of the magnetic field energy becomes maximum, whereas the quantities χ_∞ and χ_0 denote respectively the susceptibility at infinitely high frequency of the magnetic field and in a constant magnetic field.

The latter can be written as:

$$\chi_0 = \frac{\mu_0 n m^2}{3kT}, \tag{8}$$

where n is the density of the magnetic particles with a magnetic moment m. The Debye's rule describes the dependencies of the real and imaginary parts of the complex electric permittivity of a dipolar liquids on the angular frequency $\omega = 2\pi f$ of the externally applied electric field and the relaxation time τ_0.

The application of this rule for the description of magnetic liquids is based on the hypothesis of the exponential increase of magnetization when the magnetic field is switched on. As in the Debye's theory, the real part of the magnetic permittivity decreases monotonically:

$$\chi'(\omega) = \chi_\infty + \frac{\chi_0 - \chi_\infty}{1 + \omega^2 \tau_0^2}, \tag{9}$$

wheras the imaginary part has a maximum at $\omega\tau_0 = 1$ and amounts to

$$\chi''(\omega) = (\chi_o - \chi_\infty)\frac{\omega\tau_0}{1 + \omega^2\tau_0^2}. \tag{10}$$

Hence, the relaxation time can be found once we have determined experimentally the frequency at which the imaginary part of the permittivity appears. However, the dispersion equation of Debye holds only as long as we deal with a simple model with a single relaxation time and if intermolecular interactions can be neglected.

In real polydisperse magnetic liquids dispersion of the magnetic permittivity described more adequately by the following formula [3, 7] containing the distribution function of the permittivity relaxation times $f(\tau)$:

$$\tilde{\chi}(\omega) = \chi'(\omega) - i\chi''(\omega) = \chi_\infty + (\chi_0 - \chi_\infty)\int_0^\infty \frac{f(\tau)d\tau}{1 + i\omega\tau}. \tag{11}$$

In most cases one can proceed by fitting the experimental results to the following function [7]:

$$\tilde{\chi}(\omega) = \chi_\infty + \frac{(\chi_0 - \chi_\infty)}{1 + (i\omega\tau_0)^{1-\alpha}}, \tag{12}$$

where the parameter α takes values from the interval $0 \leq \alpha \leq 1$. For $\alpha = 0$, equation (12) goes over into the Debye's equation.

In the complex χ', χ'' plane (Cole-Cole diagram), the above dependence is represented by an arc of a semicircle with centre at the point $[0.5(\chi_0 + \chi_\infty), -0.5(\chi_0 - \chi_\infty)\,\mathrm{tg}(\pi\alpha/2)]$ and with the radius $R = 0.5(\chi_0 - \chi_\infty)\sec(\pi\alpha/2)$. Consequently, the centre of the semicircle lies below the axis of real values of the magnetic permittivity.

3. Propagation of an ultrasonic wave in a magnetic liquid

The theory proposed by TAKETOMI [8], who considered the anisotropy of the absorption coefficient of the ultrasonic wave propagating in a magnetic liquid, proved to be much more effective than the theories of other authors [9, 10].

Magneto-optical experiments have shown that in a magnetic liquid affected by an external constant magnetic field clusters of approximately spherical shape arise.

Their size depends on the radius of the individual magnetic particles, the strength of the magnetic field and the temperature. With growing field strength, the spherical clusters tend to form chains lying along the magnetic field lines and enhancing in this way the stiffness of the liquid.

The energy of an ultrasonic wave propagating in such a medium is converted into the energy exciting the translational and, consequently, the rotational degrees of freedom of the clusters.

Thus the amplitude absorption coefficient of the ultrasonic wave propagating in a magnetic liquid placed in an external magnetic field consist of a part related to the rotational motion of the clusters, α_r, and a translational part α_t [8]:

$$\alpha_r(\phi) = \frac{\omega^2}{2\varrho_0 c^3}\left(\frac{4\eta_s}{3} + \eta_v + 2\alpha_5 \cos^2\phi + \alpha_1 \cos^4\phi\right), \tag{13}$$

$$\alpha_t(\phi) = \frac{1}{ck^2} \cdot \frac{3\pi\eta_s r\omega^3 VN(6\pi r\eta_s + V\omega\varrho_0)}{\left(\sin\phi - \dfrac{V\omega^2\varrho_m}{k}\right)^2 + \left(\dfrac{6\pi r\omega\eta_s}{k}\right)^2}, \tag{14}$$

where c is the velocity of the ultrasonic wave of angular frequency ω, ϱ_0 and ϱ_m are the densities of the carrier liquid and magnetic particles, respectively, η_s and η_v are the dynamic and volume viscosities, r and V are the radius and volume of the cluster, N is the number of clusters per unit volume, k is the elasticity constant of the magnetic liquid, ϕ is the angle between the magnetic field strength vector and the propagation vector of the ultrasonic wave, and α_1 and α_5 are the Leslie coefficients appearing in the theory of liquid crystals [14].

On adjusting the function $\alpha_r(\phi) + \alpha_t(\phi)$ to the experimentally determined values of the anisotropy of the absorption coefficient of the ultrasonic wave in the magnetic liquid, we obtain information concerning the following physical quantities: $(4\eta_s/3 + \eta_v)$, α_1, α_5, r, k and N. On the assumptions made by Taketomi, the spherical clusters should be packed homogeneously and should be of equal size which not always takes place exactly. This e.g. may be due to the polydispersion of the magnetic particles resulting in the formation of grains of different size. Thus there is a lack of ideal packing. Due to the polydispersion of the magnetic liquid, grains with a greater diameter are more apt to coagulate than the smaller ones.

However, this tendency is opposed by thermal vibrations the energy of which, kT, is a function of the absolute temperature.

Magnetostatic considerations [11] lead to the conclusion that the energy E_{dd} required to separate two coagulated magnetic grains depends on their size and magnetic properties

according to the formula:

$$E_{dd} = \frac{\mu_0 M_s^2 V}{12}, \tag{15}$$

where M_s is the spontaneous magnetization of the magnetic particle and V its volume.

The coagulation coefficient λ of the magnetic grains, defined as the quotient of the interdipole interaction energy E_{dd} and the thermal energy kT, affects the stability of the magnetic liquid essentially.

If $\lambda > 1$, the magnetic liquid can coagulate spontaneously according to the external magnetic field applied.

Figure 3 shows $\lambda(r)$ for magnetite *versus* three temperatures $T = 273$, 293 and 373 K, thus in a temperature range accessible to the magnetite liquid with the aqueous carrier. The temperature was found to have some influence on λ which, however, is very depends strongly on the radii of the magnetic particles.

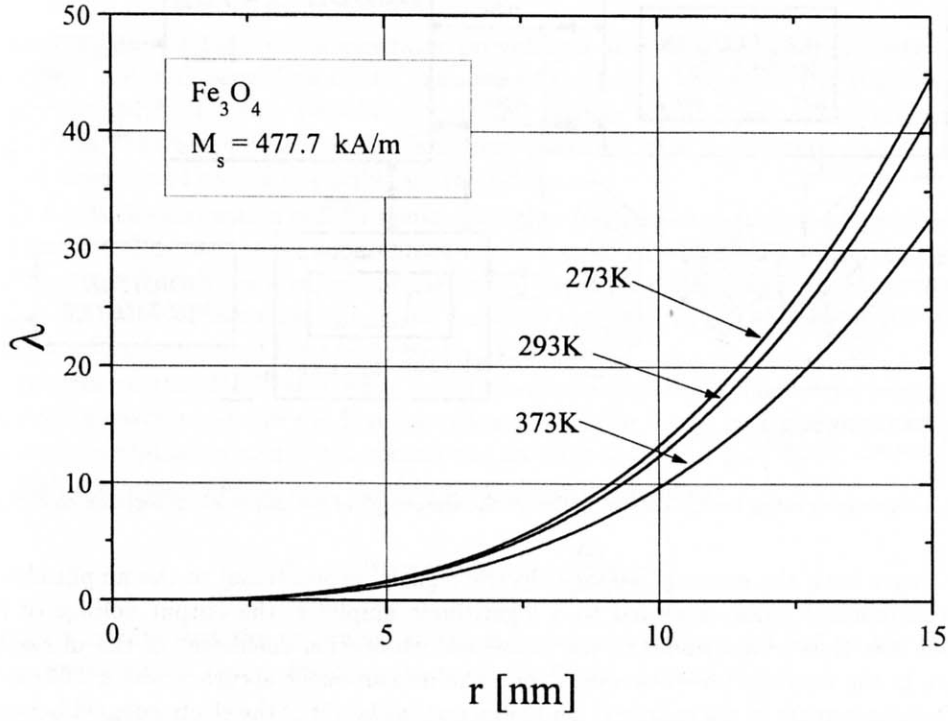

Fig. 3. Coupling coefficient of the magnetite grains $\lambda(r)$ *versus* their radius for $T = 273$ K, 293 K and 373 K.

For $\lambda < 1$ ($r < 4.5$ nm), the energy of thermal vibrations exceeds that of two dipoles in conjunction; such a monodisperse liquid should be stable. In the case of the polydisperse magnetic liquid used in our experiments, in that the mean radius amounted to 10 nm, depending on the temperature, an effective value of $\lambda = 9 \div 14$ was obtained. This points to the possibility of spontaneous coagulation.

4. Experimental

4.1. Measuring setup for the determination of the anisotropy of the absorption coefficient of ultrasonic waves

The measuring setup for the determination of the anisotropy of the absorption coefficient of the ultrasonic wave, shown in Fig. 4, consisted of subcircuits made by "MATEC". The apparatus operated on the pulse principle involved additionally a block type "MODEL 2470B" with time — delay circuits operating on the pulses of consecutive echos and two channels with analog memories in that the magnitudes of these echos were stored.

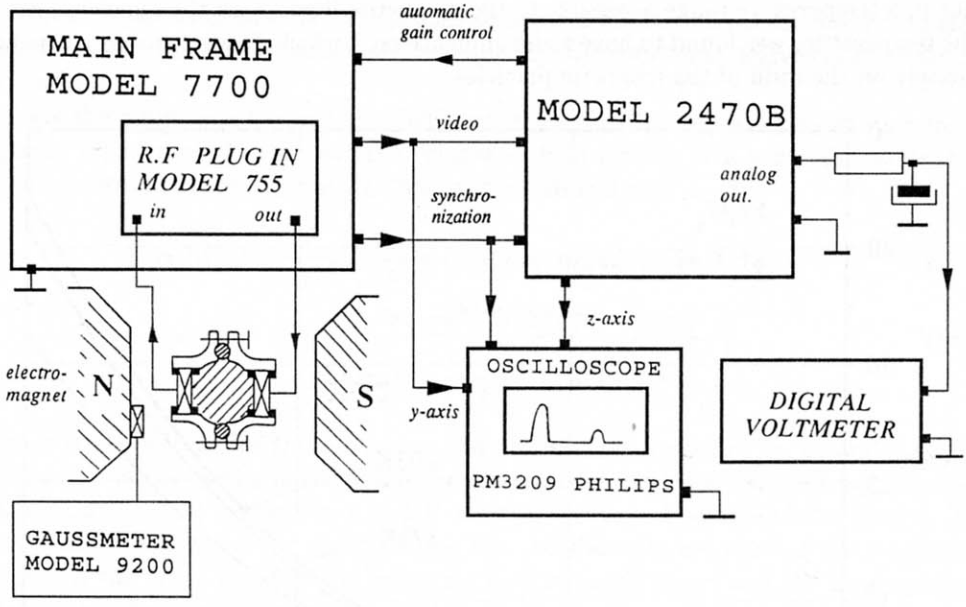

Fig. 4. Measuring setup for the determination of the anisotropy of the ultrasonic absorption coefficient.

Hence both the constant voltage electric signals, proportional to the amplitudes of the memorized echos, were fed to a logarithmic amplifier; the output voltage of the latter was thus proportional to the amplitude absorption coefficient of the ultrasonic wave in the medium under investigation. The measurement accuracy was $\pm 0.02\,\mathrm{cm}^{-1}$. The measurement of the magnetic field induction in the slit of the electromagnet between its poles was performed with an accuracy of 0.5% using a teslometer.

The temperature of the medium was stabilized to within $\pm 0.01\,\mathrm{K}$.

4.2. Measuring apparatus for the determination of the magnetic succeptibility

To determine the magnetic properties of the magnetic liquid, a Maxwell–Wien bridge (see Fig. 5) was used. The AC magnetic field applied to the cell with the magnetic fluid is perpendicular to the direction of the DC magnetic field.

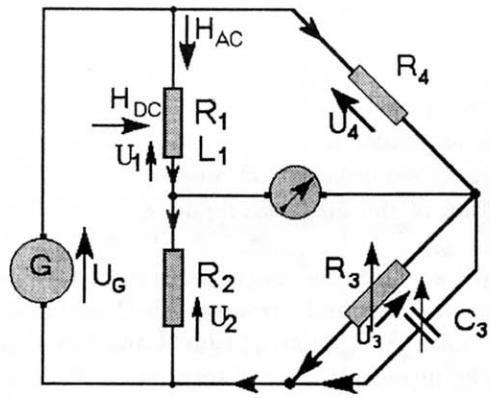

Fig. 5. Maxwell-Wien bridge for the determination of the susceptibility of EMG-605.

The bridge was fed from a generator providing a sine voltage signal of controlled amplitude and frequency. One of the branches of the bridge contained the glass vessel having the shape of a ring (Rowland ring) and holding about $3\,\mathrm{cm}^3$ of the magnetic liquid. The branch opposite the Rowland ring consisted of a capacitance decade and resistor decade and served to equilibrate the bridge.

This was checked with a milivoltmeter (at higher frequencies, a diode probe was used additionally). The two remaining branches were constructed with inductionless standard resistors ($61.9\,\Omega$). All the elements of the bridge were constructed with screened cables so that the range of measurements could be easily extended to a frequency of 100 kHz, whereas a standard use of the bridge covers 5 kHz only.

Upwards of 100 kHz, a skin effect and parasitic currents of volume type began to affect the measurements, in the first case causing an error in the imaginary part of the magnetic susceptibility and in the second one an error in its real part.

With the bridge equilibrium, the following identity is fulfilled:

$$R_2 R_4 = (R_1 + j\omega L_1)\left(\frac{R_3}{1 + j\omega C_3 R_3}\right), \tag{16}$$

whence it results that the resistance and inductance provided by the coil on the ring, the magnetic circuit being closed by the magnetic liquid, amount to

$$R_1 = \frac{R_2 R_4}{R_3}, \qquad L_1 = R_2 R_4 C_3\,. \tag{17}$$

If L_{10} is the inductance of the empty coil, we get an expression for the real part of the magnetic susceptibility:

$$\chi' = \frac{L_1 - L_{10}}{L_{10}}, \tag{18}$$

with an accuracy of the order of 0.2% [12].

5. Experimental results

The measurements have been performed for a magnetic liquid with the symbol EMG-605 made by Ferrofluidics Corporation. It consists of magnetite Fe_3O_4 grains with a mean radius of 10 nm suspended in water serving as the carrier liquid.

The values of the magnetization, initial magnetic susceptibility, dynamic viscosity and volume concentration of the magnetic liquid were 20 mT, 0.55, 0.005 Nsm^{-2} and 3.5%, respectively.

The values of density, spontaneous magnetization, crystal lattice constant, uniaxial crystallografic anisotropy constant and ferromagnetic Curie point of the magnetite Fe_3O_4 were 5240 kgm^{-3}, 477.7 kAm^{-1}, 0.84 nm, 11 kJm^{-3} and 585° C, respectively.

The anisotropy of the ultrasonic wave absorption coefficient in the magnetic liquid EMG-605 was measured at 20° C, at a constant magnetic field strength (the parameter), and the frequency of 4.38 MHz.

As an example, the dependence of the ultrasonic absorption coefficient in EMG-605 *versus* the angle ϕ at 20° C for several constant values of the magnetic field strength H is shown in Fig. 6.

The magnetic susceptibility of EMG-605 was measured *versus* the frequency f of the variable magnetic field component H_{AC} at a constant magnetizing field H_{DC} (the parameter).

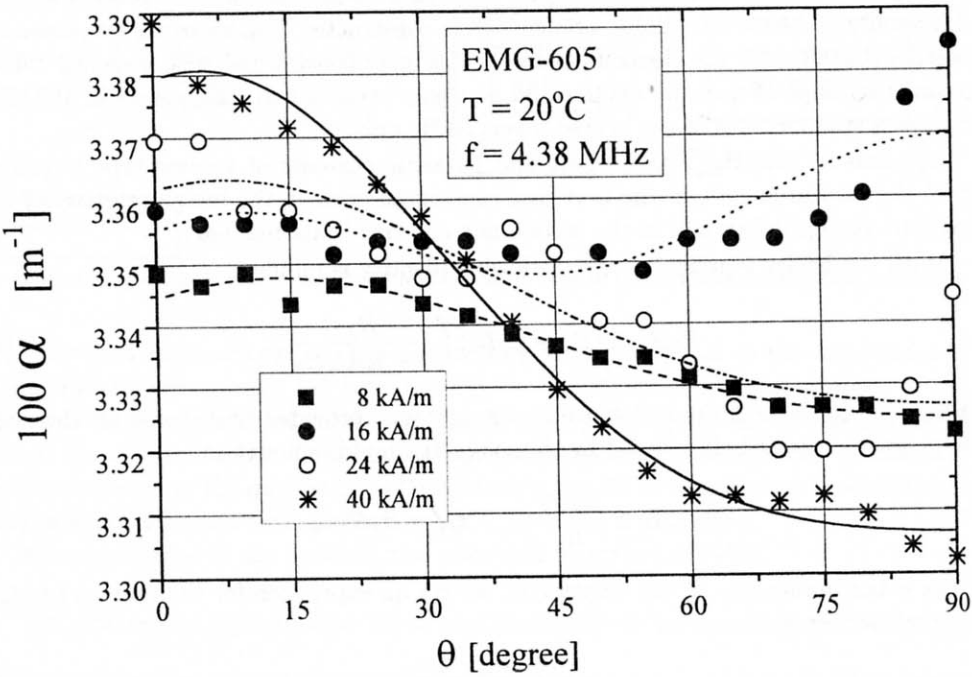

Fig. 6. Anisotropy of the ultrasonic absorption coefficient together and the curves obtained by fitting the experimental data to the Taketomi function at constant magnetic field strengths H = 8, 16, 24 and 40 kA/m.

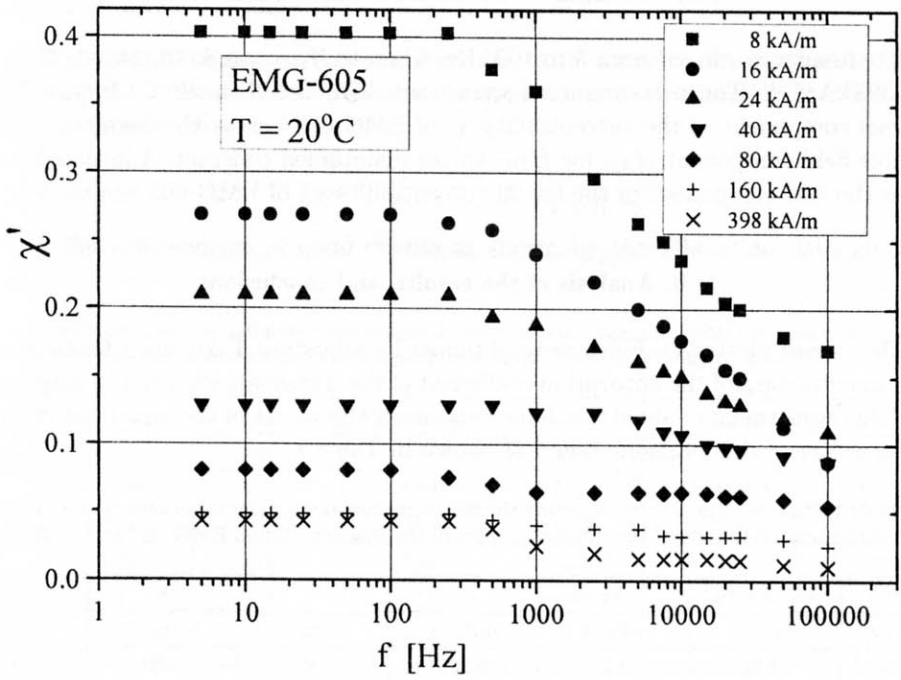

Fig. 7. Real component of the magnetic susceptibility χ' of EMG-605 *versus* frequency f of the variable magnetic field component H_{AC} at constant values of H_{DC}.

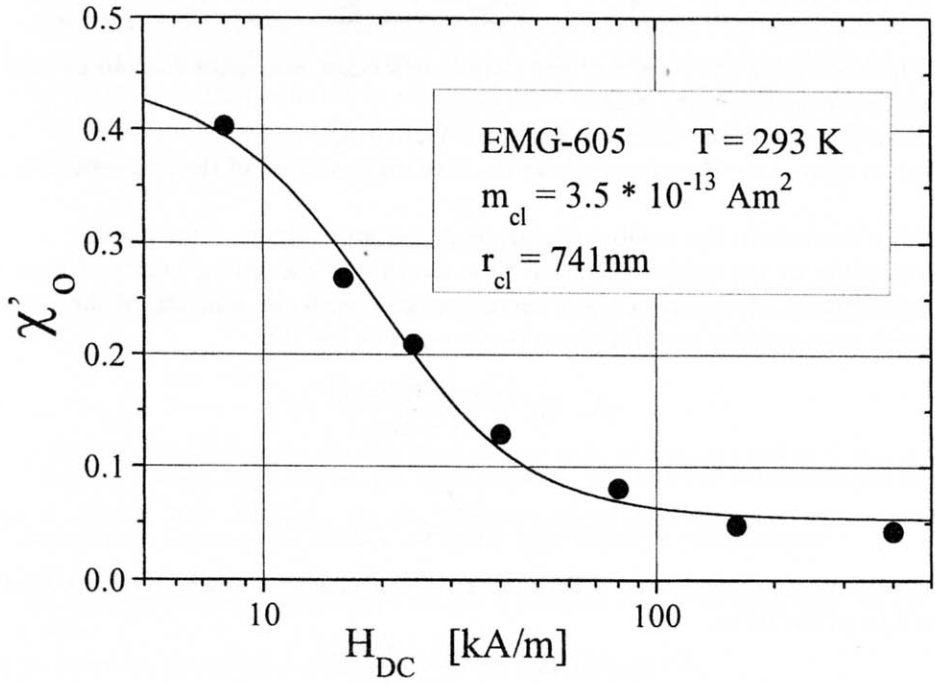

Fig. 8. Real component of the initial magnetic susceptibility χ'_0 *versus* H_{DC} and the curve resulting from the fitting to function [13] for the magnetic liquid EMG-605.

The frequency ranged from 5 to 100 kHz, whereas H_{DC} was 8, 16, 24, 40, 79.6, 159.2 and 398 kAm^{-1}. The measurements were carried out at $T = 20°$ C. Figure 7 shows the real component of the susceptibility χ' of EMG-605 *versus* the frequency f of the variable field component H_{AC} for H_{DC} values maintained constant. Additionally, Fig. 8 shows the real component of the initial susceptibility χ'_0 of EMG-605 *versus* H_{DC}.

6. Analysis of the results, and conclusions

The curves plotted in Fig. 6 were obtained by adjusting Taketomi's function to the experimental data of the absorption coefficient of the ultrasonic wave in the magnetic liquid. This adjustment enabled the determination of the values of the quantities describing the structure of the magnetic liquid as shown in Table 1.

Table 1. Results obtained by adjusting the Taketomi function to the experimental data of the absorption coefficient of the ultrasonic wave in the magnetic liquid EMG-605 at $T = 20°$C.

H	$4\eta_s/3 + \eta_v$	α_5	α_1	r	k	$N \times 10^{-16}$
kA/m	mPa · s	mPa · s	mPa · s	μm	$N \cdot m^{-1}$	m^{-3}
8	13.90	−0.121	0.099	3.67	3.90	80.6
16	14.41	−0.63	0.654	3.71	4.81	78.2
24	18.02	−0.165	0.165	3.37	4.75	71.1
40	18.57	−0.417	0.430	3.37	7.00	69.7

When analyzing the results of our ultrasonic studies, one notes that an increase in the magnetic field strength causes:

(i) an increase in the viscosity coefficient $4\eta_s/3 + \eta_v$,

(ii) an increase in the magnitude of the elasticity constant of the magnetic liquid k, and

(iii) a decrease in the number of clusters N per unit volume of the liquid.

According to the single relaxation time model, the measuring points of magnetic susceptibility $\chi'(\omega)$ shown in Fig. 7 should coincide with the function of the complex magnetic susceptibility resulting from the Langevin's law [13],

$$\chi(\omega, H_0) = \frac{\chi_0[1 + f(H_0)]}{1 + j\omega\tau_{\text{eff}}}, \tag{19}$$

where the numerator amounts to

$$[1 + f(H_0)] = 3\left[1 + \xi^{-2} - \coth^2\xi\right]. \tag{20}$$

Thus, the function expressing the real part of the magnetic susceptibility, $\chi'(\omega, H_0)$, should be of the form,

$$\chi'(\omega, H_0) = \frac{\chi_0[1 + f(H_0)]}{1 + \omega^2\tau_{\text{eff}}^2}, \tag{21}$$

where τ_{eff} is the effective relaxation time of the magnetic susceptibility.

In reality, the attempts to adjust the functions with a single relaxation time to the above experimental results failed. Whereas the application of an adjusting function with two relaxation times [6]

$$\chi(\omega) = \chi_{\infty 2} + \frac{\chi_0 - \chi_{\infty 1}}{1 + i\omega\tau_1} + \frac{\chi_{\infty 1} - \chi_{\infty 2}}{1 + i\omega\tau_2}, \tag{22}$$

permitted the achievement of good results as shown by the relaxation data given in Table 2.

Table 2. Results obtained by adjusting the magnetic susceptibility function with two relaxation times to the experimental data for the magnetic susceptibility of EMG-605 at $T = 20°$ C.

H	$\chi_0 - \chi_{\infty 1}$	τ_1	$\chi_{\infty 1} - \chi_{\infty 2}$	τ_2	$\chi_{\infty 2}$	χ_0
kA/m	–	μs	–	μs	–	–
8	0.1444	107	0.089	9.3	0.1692	0.4026
16	0.083	69.2	0.1076	4.57	0.076	0,2666
24	0.0393	210	0.0532	12.75	0.117	0.2094
40	0.03	24	0.014	3.47	0.084	0.128

In the case of the weakest magnetic field used in the measurements, $H = 8\,\mathrm{kAm}^{-1}$, the relaxation times $\tau_1 = 107\,\mu\mathrm{s}$ and $\tau_2 = 9.3\,\mu\mathrm{s}$ coincide quite satisfactorily with the components of the effective relaxation time of the magnetic susceptibility shown in Fig. 2 in accordance with the effects of Brown and Néel.

Finally, Fig. 8 shows the measuring points obtained for the real component of the initial magnetic susceptibility χ_0' *versus* H_{DC} together with the curve of fitting to the function (20). This adjustment led to a limiting value of $\chi_0' = 0.43$ for the real component of the initial magnetic susceptibility and to the mean radius of the magnetic clusters $r_{\mathrm{cl}} = 741\,\mathrm{nm}$.

Acknowledgements

The present work was carried out within KBN Research Grant No. 2PO3B 07912.

References

[1] R. Kötitz, P.C. Fannin, L. Trahms, *Time domain study of Brownian and Néel relaxation in ferrofluids*, J. Magn. Magn. Mater., **149**, 42–46 (1995).

[2] P.C. Fannin, S.W. Charles, *On the calculation of the Néel relaxation time in uniaxial single-domain ferromagnetic particles*, J. Phys. D: Appl. Phys., **27**, 185–188 (1994).

[3] P.C. Fannin, Yu.P. Kalmykov, S.W. Charles, *On the use of frequency-domain measurements to investigate time-domain magnetization decay in a ferrofluid*, J. Phys. D: Appl. Phys., **27**, 194–197 (1994).

[4] W. Fertman, *Magnetic liquids* [in Russian], High School, Minsk 1988.

[5] P.C. Fannin, S.W. Charles, T. Relihan, *Broad-band measurement of the complex susceptibility of magnetic fluids*, Meas. Sci. Technol., **4**, 1160–1162 (1993).

[6] P.C. FANNIN, S.W. CHARLES, T. RELIHAN, *On the use of complex susceptibility data to complement magnetic viscosity measurements*, J. Phys. D: Appl.Phys., **27**, 189–193 (1994).

[7] E. BLOOMS, A. CERBERS, M.M. MAIOROV, *Magnetic fluids*, Walter de Gruyter, Berlin, New York 1997.

[8] S. TAKETOMI, *The anisotropy of the sound attenuation in magnetic fluid under an external magnetic field*, J. Phys. Soc. Jpn., **55**, 838–844 (1986).

[9] K. GOTOH, D. CHUNG, *Ultrasonic attenuations in magnetic fluids*, J. Phys. Soc. Jpn., **53**, 8, 2521–2528 (1984).

[10] K. HENJES, *Sound propagation in magnetic fluids*, Phys. Rev. E, **50**, 2, 1184–1188 (1994).

[11] R.E. ROSENSWEIG, *Ferrohydrodynamics*, Dover Publications, INC., Mineola, New York 1997.

[12] A. JELLONEK, J. KURYŁOWICZ, M. ŁAPIŃSKI, Z. SICIŃSKI, *Electrical measurements*, PWN, Warszawa 1971, pp. 244–245.

[13] P.C. FANNIN, B.K.P. SCAIFE, S.W. CHARLES, *The field dependence of the complex frequency-dependent susceptibility of magnetic fluids*, J. Phys. D: Appl. Phys., **21**, 533–534 (1988).

[14] P.G. GENNES, *The physics of liquid crystals*, Oxford University Press, London 1975.

ARCHIVES OF ACOUSTICS
24, 2, 145–160 (1999)

APPLICATION OF THE ROAD TRAFFIC NOISE MODEL TO URBAN SYSTEMS

E. WALERIAN, R. JANCZUR and M. CZECHOWICZ

Institute of Fundamental Technological Research
Polish Academy of Sciences
(00-049 Warszawa, ul. Świętokrzyska 21, Poland)

In this paper, the computer simulation program PROP4, that allows prediction of the time-average sound level within an urban system, is presented together with the analysis of its accuracy. The simulation is based on an environmental noise model which contains the propagation model and the equivalent roadway model. The roadway as a noise source is represented by a sum of sound exposures due to the individual vehicle drive-by. The PROP4 allows for multi-lane roadways and different representations of sources for various classes of vehicles. Interactions of waves with obstacles are limited to multi-reflections from walls as well as single and double diffractions on wedges. The empirical data [14] have been compared with those obtained by using the PROP4 program. The comparison, especially for the relative decay of the time-average sound level with distance, shows a very good agreement with empirical data.

Notations

E^g_{Aj}	sound exposure (Eq. (4)),
G	number of vehicle classes (Eq. (5)),
$H(\mathbf{R}(u\Delta x_E), f)$	urban transfer function of a source at the $\mathbf{R}(u\Delta x_E)$ position in relation to the observation point (Eq. (14)),
J	number of lanes (Eq. (5)),
K	upper order of interaction (Eqs. (17), (18)),
L_{Aeq}	time-average sound level in $dB(A)$ (Eq. (2)),
L^g_{WA}	g-class vehicles equivalent source power level in $dB(A)$ (Eq. (9)),
N	number of panels in an urban system (Eqs. (17), (18)),
N^g_j	g-class vehicles rate flow on a j-lane in [vehicles/h] (Eq. (6)),
$p(S,P)$	acoustical pressure at the observation point P due to the unit simple-harmonic point source $Q(S)$ at the point S (Eqs. (15), (16))
$p_A(t)$	A-weighted sound pressure registered at the observation point (Eq. (2)),
$Q(...)$	source model (Eq. (1)),
$q^g_A(f_w)$	A-weighted relative power spectrum of a g-class vehicles (Eq. (11)),
$\mathbf{R}^g(x_j)$	vector describing a g-class vehicle position on a j-lane in relation to the observation point (Eq. (5)),
R_{jo}	smallest distance between the observation point and the moving source (Fig. 1),
$\{\mathbf{R}(n)\}$	set of vectors describing geometry of panels in an urban system (Eq. (19)),
$\{\mathcal{R}(n)\}$	set of reflection coefficients of panels in an urban system (Eq. (19)),
$\{\mathcal{T}(n)\}$	set of transmission coefficients of panels in an urban system (Eq. (19)),
U_j	number of the equivalent source discrete positions during its drive-by (Eq. (5)),

v_j^g average speeds of g-class vehicles along a j-lane in [m/h] (Eq. (6)),
$W_A^g(f_w)$ experimentally obtained source power spectrum in octave bands for g-class vehicles (Eqs. (11), (12)),
Δx_j^g g-class vehicles average spacing along j-lanes (Eq. (6))
Δx_E summation step (Eq. (5)),
$\widehat{\Pi}(...)$ operator describing wave propagation (Eq. (1)),
$\widehat{\Pi}_0(...)$ operator describing human perception (Eq. (1)).

1. Introduction

A road traffic noise model in a built-up area has been proposed previously by the authors [1–4]. It comprises the source model which can be made up of unit simple harmonic point sources, and the propagation model, which can be simply identified with the urban system transfer function. The special model for the roadway, as the predominant noise source in an urban area, has been introduced. It is constructed of equivalent point sources representing the individual vehicles moving along a roadway [5]. Multiple reflections and multiple diffractions have been included in the propagation model as interactions with obstacles. Those interactions have been described as a high frequency approximation of the exact solution. The latter is appropriate for the far field conditions [6–8]. Generally, the noise model presented here can be used for any other systems for that the conditions are fulfilled.

A vast literature is devoted to the sound propagation in a system of a complex building arrangement where the results of field measurements, scale modeling and analytical models are used to predict the time-average sound level, e.g. [9–14]. Nevertheless, the applications of analytical models for the outdoor noise propagation in an urban area are the most favorable ones as, apart from their flexibility; they may be applied at various stages of a project design process.

In the analytical description, the first element disturbing the free propagation is the ground. To approach the real conditions, the ground is considered to be an impedance plane. As the next step, the layer structure of the atmosphere may be included [15]. Nevertheless, the analytical description of the large distance propagation in this simplest case is still not easy, mainly because of the varying weather conditions [16].

When neglecting the medium inhomogeneity and weather conditions (see Sec. 3), the acoustical field description can be simplified to the interactions with the obstacles. For the simplest example of a single screen on the impedance ground, the solution has been found as the well-known canonical solution of diffraction at the edge and the reflection from an impedance plane [17–19]. Obstacles of more complex shapes can be made up of plane screens of limited length (panels).

To analyze noise propagation within obstacles, the image sources method for enclosures and semi-enclosures can be used [20, 21]. To get the general field description, the phenomenon of diffraction has to be included. For an urban system the description including multiple reflections and the single diffraction at screens' edges has been most frequently applied [22]. The special case of a plane screen in front of a building, which fulfills the above assumptions, has been investigated and verified by scale

modeling experiments [23, 24]. The description, other than that presented here, which contains multiple reflections and multiple diffractions, has also been elaborated [14]. In this case, the Keller geometrical theory of diffraction has been used in the form developed for building wedges [25]. The two methods [14, 22], as well as the environmental noise model presented here, result in computer simulation programs which can be used in forecasting noise.

In the PROP4 simulation program which is based on the road traffic noise model, the propagation model is adjusted to obstacles (buildings) whose shapes are approximated by a shoe-box. The plane acoustical screens are included. The double diffraction at the parallel building wedges and at the edges of two parallel screens are taken into account. The PROP4 program can be used for a multiple-lane roadway with different sources for different classes of vehicles.

The simulation program ENVIRA [26] founded on the description of propagation in a built-up area [14], is similar to the program presented here in its physical foundations and complexity. Contrary to this, commercially spread software, e.g. MICRO-BRUIT (CETUR France) [27], MITHRA (CSTB France), CADNA (DATAUSTIK Germany), can be judged mostly on the trusting to distributors since those programs are not accompanied by relevant information concerning the construction of the simulation model. In the case of the free distribution of DEMO, it is possible to perform a mutual comparison for the same input parameters. This is what the authors plan for the near future.

The aim of this paper is to show how the road traffic noise model works when the PROP4 program is applied to the urban system for which there are field measurements [14]. The exact analysis of the simulation program accuracy is almost impossible since it depends on the input data, models adequacy, and on the accuracy of the description of an individual wave interaction: the latter depends on the position of the observation point. In spite of that, a rough estimation performed here allows to say that the accuracy of the applied simulation program is comparable with that of the scale models [28, 29].

2. The road traffic noise model

In order to solve the noise abatement problem in an urban area, the model of environmental noise is needed. Taking the time-average sound level for the annoyance rating, the model can be presented in the following form:

$$L_{Aeq} = \widehat{\Pi}_0(...)\,\widehat{\Pi}(...)\,Q(...), \tag{1}$$

where the source is represented by $Q(...)$, the operator $\widehat{\Pi}(...)$ describes wave propagation, and the operator $\widehat{\Pi}_0(...)$ describes the human perception.

It is widely discussed how to measure and calculate the noise annoyance. Despite all doubts, the International Standards Organization recommends the time-average sound level. Thus, the operator $\widehat{\Pi}_0(...)$, acting on the acoustical pressure at the receiver, has to perform the A-weighting, time averaging and the level calculation.

In the time domain, the time-average sound level is defined by

$$L_{Aeq}(T) = 10\log\left\{\frac{1}{T}\int_{-T/2}^{T/2}\left[p_A^2(t)/p_0^2\right]\,dt\right\}, \tag{2}$$

$$p_0 = 2\cdot 10^{-5}\,\mathrm{N/m^2}, \tag{3}$$

where $p_A(t)$ is the A-weighted sound pressure registered during the time interval T. Its relation to the sound exposure level and its representation in the frequency domain, using the environmental noise model (Eq. (1)) will be given in the next two sections.

2.1. The roadway as a noise source

The roadway is a complex noise source composed of individual vehicles belonging to G classes and moving along J lanes. The equivalent source of a g-class vehicle is assumed to be an omnidirectional point source which radiates sound into a homogeneous and loss-free atmosphere at rest. It is characterized by the power spectrum $W_A^g(f_w)$ in the octave-frequency bands and the position above the road surface z_0^g [30].

The roadway model as noise source is assumed by adopting the concept of the sound exposure E_{Aj}^g [11, 12, 31–34] to a g-class vehicle on the j-lane:

$$E_{Aj}^g = \frac{1}{t_0}\int_{-\infty}^{\infty}\left(p_{Aj}^g(t)\right)^2\,dt \simeq \frac{1}{t_0}\int_{-\tau/2}^{\tau/2}\left(p_{Aj}^g[\mathbf{R}(t)]\right)^2\,dt, \tag{4}$$

where $t_0 = 1\,\mathrm{s}$.

For freely flowing traffic of flow rates N_j^g moving along the lines ($y = y_{j0}$, $z = z_0^g$) (Fig. 1) with the average speeds v_j^g [m/h], the time-average sound level is:

$$L_{Aeq}(T) = 10\log\left(\sum_{g=1}^{G}\sum_{j=1}^{J} N_j^g E_{Aj}^g/p_0^2\right)$$

$$= 10\log\left(\sum_{g=1}^{G}\sum_{j=1}^{J}\frac{1}{\Delta x_j^g}\int_{x_{j1}}^{x_{j2}} p_A^2\left[\mathbf{R}^g(x_j)\right]dx_j/p_0^2\right)$$

$$\simeq 10\log\left(\sum_{g=1}^{G}\sum_{j=1}^{J}\frac{\Delta x_E}{\Delta x_j^g}\sum_{u=1}^{U_j} p_A^2\left[\mathbf{R}_j^g(u\Delta x_E)\right]/p_0^2\right), \tag{5}$$

where

$$\Delta x_j^g\ [\mathrm{m/vehicle}] = \frac{v_j^g\ [\mathrm{m/h}]}{N_j^g\ [\mathrm{vehicle/h}]}, \tag{6}$$

is the average spacing between successive vehicles on the lane segments. In Eqs. (4) and (5), it is assumed that the sound level due to the source at the ends of the lane segment

(x_{j1}, x_{j2}) is by 10 dB lower than that due to the source at the smallest distance R_{j0} (Fig. 1); this means that

$$(x_{j2} - x_{j1}) \geq 6R_{j0}. \tag{7}$$

Since the analytical integration in Eq. (5) can be performed only for free space, i.e. when there are no buildings, for the propagation through an urban system it has to be replaced by discrete summation with a step Δx_E.

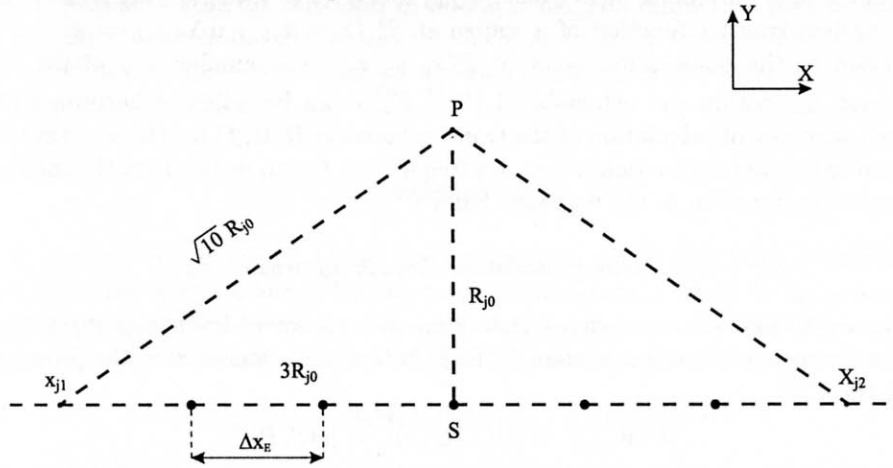

Fig. 1. The locations of an equivalent point source along the highway lane segment.

Thus, the time-average sound level is expressed by:

$$L_{Aeq}(T) = 10 \log 10 \left(\sum_{g=1}^{G} \sum_{j=1}^{J} \frac{\Delta x_E}{\Delta x_j^g} 10^{0.1 SL^g(U_j)} \right), \tag{8}$$

where

$$SL^g(U_j) = L_{WA}^g + L_{U_j}^g(P), \tag{9}$$

$$L_{U_j}^g(P) = 10 \log \left(\frac{1}{4\pi} \sum_{w=1}^{10} q_A^g(f_w) w^g(U_j, f_w) \right). \tag{10}$$

The quantity $SL^g(U_j)$ represents the sound level due to the set of U_j g-class equivalent sources spread along the j-lane with a Δx_E step. Their A-weighted relative power spectrum

$$q_A^g(f_w) = \frac{W_A^g(f_w)}{\sum_{w=1}^{10} W_A^g(f_w)}, \tag{11}$$

is defined by the obtained experimentally source power level spectra $L_{WA}^g(f_w)$ in ten octave bands:

$$\sum_{w=1}^{10} W_A^g(f_w) = W_0 10^{0.1 L_{WA}^g}, \tag{12}$$

$$W_0 = 10^{-12} \text{ Watts}. \tag{13}$$

In the w-octave-band of the center frequency f_w, the factor

$$w^g(U_j, f_w) = \frac{1}{D_w} \sum_{d=1}^{D_w} \sum_{u=1}^{U_j} \left| H(\mathbf{R}_j^g(u\Delta x_E), f_{wd}) \right|^2, \tag{14}$$

represents the average acoustical energy of the set of U_j point sources of unit strength that emit simple harmonics of frequencies $f_{wd} \in \langle F_w^{(1)}, F_w^{(2)} \rangle$. In Eq. (14) $H(\mathbf{R}, f)$ is the urban system transfer function of a source at $S_{uj}^g(x = x_{j1} + u\Delta x_E, y = y_{j0}, z = z_0^g)$ in relation to the observation point at $P(x_p, y_p, z_p)$. The number D_w of the simple harmonics f_{wd} within the octave-band $\langle F_w^{(1)}, F_w^{(2)} \rangle$ can be adjusted according to the required accuracy of calculation of the transfer function $H(\mathbf{R}, f)$ for the w-octave-band. (In the roughest approximation, the center frequencies f_w can be taken for the calculation of the transfer function in the w-octave-band.)

2.2. Noise propagation through an urban area

To have an explicit expression for the time-average sound level (Eqs. (8)–(14)), the transfer function of an urban system $H(\mathbf{R}, f)$ is needed. It stems from the propagation model (Eq. (1))

$$|H(\mathbf{R}, f)|^2 = \left| \widehat{\Pi}(...) Q(S) \right|^2 = |p(S, P)|^2. \tag{15}$$

It represents the acoustical pressure at the point P, due to the unit strength simple harmonic point source $Q(S)$, after the propagation through a built-up area.

The operator $\widehat{\Pi}(...)$, describing the propagation through an urban area, in an ideal loss-free medium at rest, to the observation point in front of a building facade, results in the operator describing interactions with obstacles.

The urban system under consideration is represented by the half-space limited by the ground on which the obstacles are placed. The obstacles are modeled by a set of panels. In the case of buildings, this yields shoeboxes (four side walls and a roof), in the case of plane acoustical screens — single panels.

When the dimensions of the obstacles and their mutual distances are large in comparison to the wavelength predominant in the A-weighted noise spectrum, the large-distance approximation ($kR \gg 1$) is justified. Then the interaction of the sound with an obstacle made up of panels can be divided into reflection and transmission through a panel, treated as an unlimited one, and the diffraction at the wedges (edges) [6, 8]. Thus, the operator $\widehat{\Pi}(...)$ (Eq. (15)) contains the sum of parallel chains of elementary interactions of the transmission, reflection and diffraction at wedges (edges). Each chain describes a different wave path to the observation point. The total field, in the system of N panels with M wedges (edges), for the upper order of interactions K, is a sum of the geometrical and diffraction parts [4]:

$$p(S, P) = p^g(S, P) + p^d(S, P), \tag{16}$$

where

$$p^g(S, P) = \sum_{k=1}^{K} \sum_{i=1}^{I(N,k)} p_i(S, P; k), \tag{17}$$

and

$$p^d(S,P) = \sum_{k=1}^{K} \sum_{i=1}^{I(N,M,k)} p_i(S,P;k), \tag{18}$$

The geometrical part of the field $p^g(S,P)$ (Eq. (17)) is composed of chains of interactions containing only transmissions and reflections, where $I(N,k)$ is the number of the wave possible paths for this kind of interactions. The diffraction part of the field $p^d(S,P)$ (Eq. (18)) contains the chains in which, apart from transmissions and reflections, a diffraction appears at least once, and $I(N,M,k)$ is the number of the wave possible paths of this kind.

3. Simulation model

The roadway model (Sec. 2.1) and the propagation model (Sec. 2.2), describing the wave interaction with buildings for the noise environmental model in an urban area (Eq. (1)), enable the construction of a simulation program. In the PROP4 simulation program, allowing calculation of the time-average sound level, the propagation model

$$\widehat{\Pi}(...) = \widehat{\Pi}\,(N, \{\mathbf{R}(n)\}, \{\mathcal{R}(n)\}, \{\mathcal{T}(n)\}, \mathbf{R}(P), K) \tag{19}$$

contains the following parameters: N – number of the panels, $\{\mathbf{R}(n)\}$ – set of the vectors describing the geometry of the panels, $\{\mathcal{R}(n)\}$ – set of the reflection coefficients of the panels, $\{\mathcal{T}(n)\}$ – set of the transmission coefficients of the panels, $\mathbf{R}(P)$ – observation point position, K – upper order of the interaction.

The roadway model of several lanes and different equivalent sources for different classes of vehicles:

$$Q(...) = Q\left(J, G, \{N_j^g\}, \{v_j^g\}, \{\mathbf{R}^g(x_j)\}, \{q_A^g(f_w)\}, \{L_{WA}^g\}, \Delta x_E\right), \tag{20}$$

has the following source parameters: J – number of the lanes, G – number of the vehicle classes, $\{N_j^g\}$ – set of the vehicle rate flow on the lanes [vehicles/h], $\{v_j^g\}$ – set of the average vehicle speeds [m/h], $\{\mathbf{R}^g(x_j)\}$ – set of vectors describing the vehicle positions on the lanes, $\{q_A^g(f_w)\}$ – set of the A-weighted relative power spectrum of the vehicles, $\{L_{WA}^g\}$ – set of the vehicle equivalent source power levels, Δx_E – the summation step.

The simulation program PROP4 gives a quantitative answer to the question how the time-average sound level depends on the source parameters (Eq. (20)) and on the urban system parameters (Eq. (19)). Though a change of the reflection coefficients of the panels (walls, ground surface) is possible, the decisive factors are the mutual arrangement of the buildings, their dimensions, and the source locations (a roadway) [35, 36].

The accuracy of the sound level calculation is affected by:

- the adequacy in the modeling of the real conditions,
- the simulation model accuracy.

The adequacy is related to the general assumptions made in modeling the source and the propagation phenomenon. Here, both the source model and the propagation model are constructed for the far field conditions. It is justified for the A-weighted spectra of

urban noise since the distances from a source to the place of the first interaction, and between the subsequent ones, are of the order of a few wavelengths of the dominating component.

In the source model assumed, a vehicle is represented by the equivalent point source of a given power spectrum with a directivity characteristic (when needed). The energy (sound exposure), emitted during a drive-by of a single vehicle, is calculated as the sum of energies at the sequence of discrete positions along the route instead of an integral. The acoustical pressure at the observation point, due to the equivalent point source representing a vehicle at a discrete position, is the sum over all the possible wave paths with their phases included. Summing up the squared pressures over all discrete positions gives the sound exposure of a vehicle drive-by.

In the propagation model, describing transmissions, reflections and diffractions at obstacles, all the effects related to the air inhomogeneity and variations in the meteorological conditions are omitted. Thus, the propagation model is adequate only for neutral meteorological condition [37]. The question whether these conditions are representative for the annoyance judgment is still an open one [12, 38]. Other simplifications are related to the urban system geometry, where the real obstacles are replaced by shoeboxes or plane panels.

In the case when the general assumptions are fulfilled, the accuracy of the simulation model depends on the modeling adequacy (assumed simplifications in the system geometry) and the accuracy of estimation of the input parameters. Some of them are not easily to obtain. However, the absolute value of the time-average sound level L_{Aeq} is not always required. Sometimes the change of L_{Aeq} caused by the variations in the source and/or propagation parameters (Eqs. (19), (20)) is sought, as e.g. in the case of shielding efficiency of screens and other obstacles where the equivalent source power level L^g_{WA} is not needed. Then, the information provided by the simulation model of the relative change in the L_{Aeq} value could be regarded as more reliable one than that of the absolute value. In this situation some parameters can be eliminated and, at least, some effects of simplifications can be removed.

Generally, the noise rating in the real environmental conditions, expressed as annoyance, depends on nonacoustical factors. It still remains unclear to what extent an annoyance-based approach is protective for human health and well-being. Although, keeping up with the noise limits, time-average sound level can be treated as a guideline in the acoustical designing. Since the simple noise abatement is limited because of technical and economic reasons, a new tendency appears which is called soundscape designing [39–41]. According to it, the simulation program comprising the sound field description has to be completed by an appropriate procedure of real annoyance estimation.

However, there are still problems with transferring the acoustical field description of better accuracy offered and the new techniques of metrology into the formulation of standards [42]. Moreover, although the science and technology provide tools and measures for noise abatement, the scope of policy is decided by the authorities. They issue laws, that are legal tools for the standard execution and can influence the process by determining economic preferences [43]. Simulation models, which can provide alternative solutions, are the best grounds for making decision.

3.1. Sound level calculation

For the simplest road model in the simulation model PROP4 $J = 1$ and $G = 1$. This means that the vehicle stream is treated as if it were concentrated at the road axis and one equivalent point source is assumed for all the vehicles. The reason for those assumption is the fact that, most frequently, a full set of data required for the simulation model is lacking. Moreover, representing a vehicle by a single equivalent point source, the fact that there are several noise sources in a vehicle is neglected. One can find expressions for equivalent source power as a function of the vehicle speed. The dependence of the energy spread within the spectrum on vehicle speed and the equivalent source height above the ground, which results from the varying participation of the vehicle elementary sources, are rarely available [30].

When vehicles are divided into two classes: light and heavy vehicles, and when the average speeds for these classes v^l and v^h are given, the single equivalent source can be applied with the percentage of heavy vehicle, p, as parameter of the simulation model. Then:

$$N = N^l + N^h, \tag{21}$$

$$v = \left[(1 - 0.01p)v^l + 0.01pv^h\right], \tag{22}$$

$$L_{WA} = 10\log\left((1 - 0.01p)10^{0.1L^l_{WA}} + 0.01p10^{0.1L^h_{WA}}\right). \tag{23}$$

The equivalent point source can be assumed to be a point emitting noise of a spectrum typical of traffic [44].

Then, the time-average sound level in an urban system due to the roadway segment of total flow rate N [vehicles/h] moving along the x-axis ($y = y_0$, $z = z_0$) with a steady speed v [m/h] is expressed by

$$L_{Aeq}(J = 1, G = 1) = L_{WA} + 10\log\frac{\Delta x_E}{\Delta x} + L_U(P), \tag{24}$$

$$L_U(P) = 10\log\left(\frac{1}{4\pi}\sum_{w=1}^{10} q_A(f_w)w(U, f_w)\right). \tag{25}$$

As can be seen, the time-average sound level is straight affected by the equivalent source power level, L_{WA}, and the average vehicle spacing (Eq. (6)). The sound level $L_U(P)$ depends on the equivalent point source relative power spectrum, $q_A(f_w)$, and the urban system transfer function for the sequence of U sources:

$$w(U, f_w) = |H\left(N, \{\mathbf{R}(n)\}, \{\mathcal{R}(n)\}, \{\mathcal{T}(n)\}, \mathbf{R}(P), \{\mathbf{R}(S_u)\}, K, U(\Delta x_E), f_w\right)|^2. \tag{26}$$

Its value depends on the upper order of interactions K, and the summation step Δx_E which can be arbitrary chosen by the user of the simulation program.

From the physical point of view, the number of interactions is unlimited. When the source is placed within two parallel surfaces (canyon structure), the specifying of an appropriate K value can be substantial. In other cases $K = 3$ seems to be sufficient [1-4, 35, 36]. The summation step Δx_E appears explicitly in the expression for the

sound level (Eq. (24)) and affects the value of $w(U, f_w)$ by the number of point sources $U(\Delta x_E) = (x_{j1} - x_{j2})/\Delta x_E$ representing a moving vehicle, and by their positions, $\mathbf{R}(S_u)$, in the urban system. The number of sources and their exact positions are decisive factors in the calculation of the $w(U, f_w)$ value as they determine the possible paths of reaching the observation point (Eqs. (16)–(18)). The influence of the Δx_E value is not easy to predict but for enough small values of Δx_E, the $w(U, f_w)$ value is expected to be independent of it [35]. For both parameters: the length of the summation step Δx_E and the upper order of interactions K, the appropriate values can be chosen with a step-by-step procedure taking 1 dB as the limit of the final change in the sound equivalent level.

4. Example

Now, the results of measurements carried out in Wrocław at the site of the Zachodnia St. (Fig. 3) [14] will be discussed. Next, the results obtained by the two simulation models $R(1)$ and $R(2)$ given in [14] and the PROP4 model will be compared.

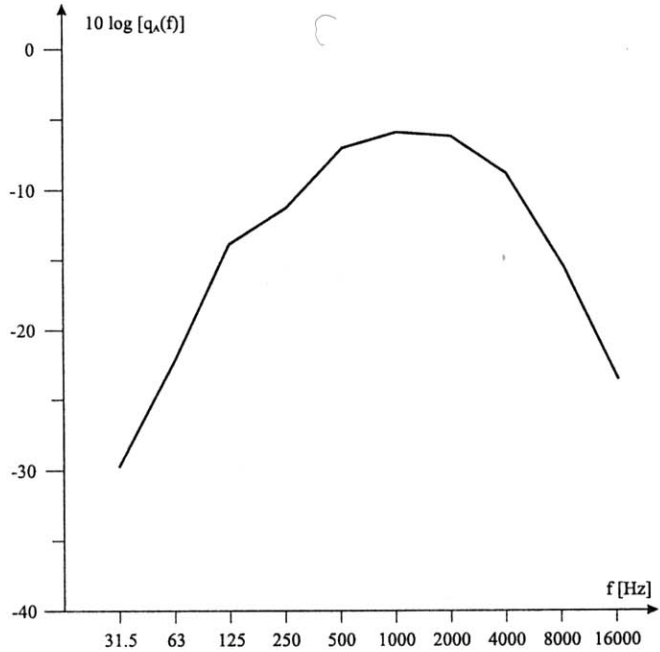

Fig. 2. The A-weighted relative power spectrum $q_A(f)$ (Eq. (11)) of the average traffic noise [14].

The sound levels are measured for $T = 900\,\mathrm{s}$ and the sampling time $t = 1\,\mathrm{s}$ at the observation points $P(z_p = 2\,\mathrm{m})$. The values of flow rates and speeds have been estimated for light and heavy vehicles.

The two simulation models, $R(1)$ and $R(2)$, have taken into account, as an averaged effect, the attenuation in the propagation medium and the influence of the impedance ground. In both the models a single reflection from the buildings' walls has been assumed

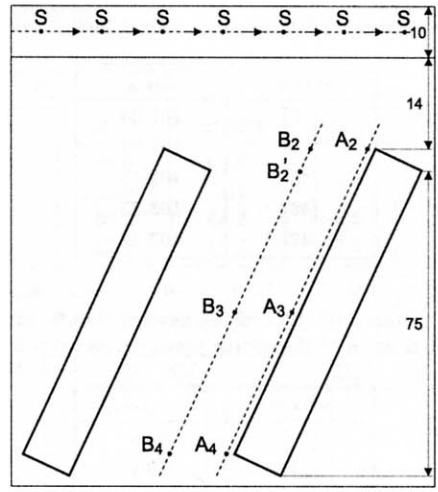

Fig. 3. The urban system under consideration [14].

for the distance $R_0 < 40\,\text{m}$ from the street axis and two reflections for $R_0 > 40\,\text{m}$. The $R(1)$ model has omitted the diffraction phenomenon, while the $R(2)$ model has omitted the background noise which is 50 dB (A). In the $R(1)$, model the movement of the vehicles has been simulated as a statistical process. In the $R(2)$ model, the 10 m street segments have been replaced by the equivalent point source at the street axis and at a height $z_0 = 0.5\,\text{m}$, with equivalent sources of the traffic noise spectrum $q_A(f)$ (Fig. 2).

The same equivalent source parameters z_0 and $q_A(f)$ as in the $R(2)$ model have been used in the PROP4 model. For the following measured vehicle stream parameters on the roadway segment: total flow rate $N = 1200\,\text{vehicles/h}$, the speed of light vehicles $v^l = 60\,\text{km/h}$ and that of the heavy ones $v_h = 45\,\text{km/h}$, with a percentage of heavy vehicles $p = 20\%$, the average speed of the vehicle flow (Eq. (22)) is

$$v = 57\,\text{km/h}, \tag{27}$$

that results in the average spacing (Eq. (6)):

$$\Delta x = v/N = 47.5\,\text{m/vehicle}. \tag{28}$$

Using the PROP4 simulation program the time-average sound level (Eq. (24)) for $\Delta x_E = 4$ m is given by

$$L_{Aeq}(P) = L_{WA} + 10\log\frac{\Delta x_E}{\Delta x} + L_U(P) = L_{WA} - 10.7 + L_U(P), \tag{29}$$

where $L_U(P)$ (Eq. (25)) is calculated with a number of interactions up to $K = 3$.

To calculate the sound equivalent level (Eq. (29)), the value of the source power level L_{WA} is needed. To this end, using the expression relating the source power to the vehicle speed [12, 14, 45–47], the source power level L_{WA} (Eq. (23)) is calculated (Table 1).

For the point A_2 (Fig. 3), which is nearest to the source and at that the direct wave has to prevail the other terms, the time-average sound level $L_{Aeq}(A_2)$ (Eq. (29))

Table 1. The calculated equivalent point source power level values L_{WA}.

source	L_{WA}
[12]	101.03
[14]	101.65
[45]	101.65
[46]	103.32
[47]	103.72

Table 2. The time-average sound level in an urban system (Fig. 3) at the observation point A_2 calculated using of the source power levels from Table 1.

source	$L_{Aeq}(A_2)$
[12]	69.8
[14]	70.4
[45]	70.4
[46]	72.1
[47]	72.5
measured [14]	68.0

is calculated for different values of L_{WA} (Table 1). The results obtained presented in Table 2 are used for choosing the appropriate value of the source power level. As the L_{WA} value estimated according to [12] results in the best fit to the value measured in the real urban system, it has been used for the calculation of $L_{Aeq}(P)$ at all the observation points in the urban system. The results are presented in Tables 3 and 4 and in Fig. 4.

Table 3. The time-average sound level at observation points lying along the A line in the urban system (Fig. 3).

point	L_{Aeq}				$\Delta L_{Aeq} = L_{Aeq}(A_i) - L_{Aeq}(A_2)$			
	M	$R(1)$	$R(2)$	PROP4	M	$R(1)$	$R(2)$	PROP4
A_2	68.0	66	69.4	69.8				
A_3	60.5	57	58.7	64.2	−7.5	−9	−10.7	−5.5
A_4	57.5	54	58.2	60.0	−10.5	−12	−11.2	−9.8

M – measured, $R(1)$ – calculated according to the $R(1)$ model [14], $R(2)$ – calculated according to the $R(2)$ model [14], PROP4 – calculated according to the PROP4 simulation program.

In Tables 3 and 4 there are also collected the time-average values of the sound levels measured in the urban system [14] and those calculated according to the two simulation models $R(1)$ and $R(2)$ given in [14]. The absolute values of the time-average sound levels, $L_{Aeq}(A_i)$ and $L_{Aeq}(B_i)$, are accompanied by the relative values $\Delta L_{Aeq} = L_{Aeq}(A_i) - L_{Aeq}(A_2)$ and $\Delta L_{Aeq} = L_{Aeq}(B_i) - L_{Aeq}(B_2)$. As it can be seen, the relative values calculated according to the PROP4 model match the best measured relative values. The better matching of the relative values results from the omission of the source power level of the moving equivalent point source which represents the vehicles. The source power estimation constitutes a separate problem. Its accuracy affects immediately

Table 4. The time-average sound level at observation points lying along the B line in the urban system (Fig. 3).

point	L_{Aeq}				$\Delta L_{Aeq} = L_{Aeq}(B_i) - L_{Aeq}(B_2)$			
	M	$R(1)$	$R(2)$	PROP4	M	$R(1)$	$R(2)$	PROP4
B_2	67.0	68	69.6	69.0				
B_2'	66.3	66	65.0	68.1	−0.7	−2	−4.6	−0.9
B_3	61.5	62	57.2	63.2	−5.5	−6	−12.4	−5.8
B_4	59.5	56	52.4	59.6	−7.5	−12	−17.2	−9.4

M – measured, $R(1)$ – calculated according to the $R(1)$ model [14], $R(2)$ – calculated according to the $R(2)$ model [14], PROP4 - calculated according to the PROP4 simulation program.

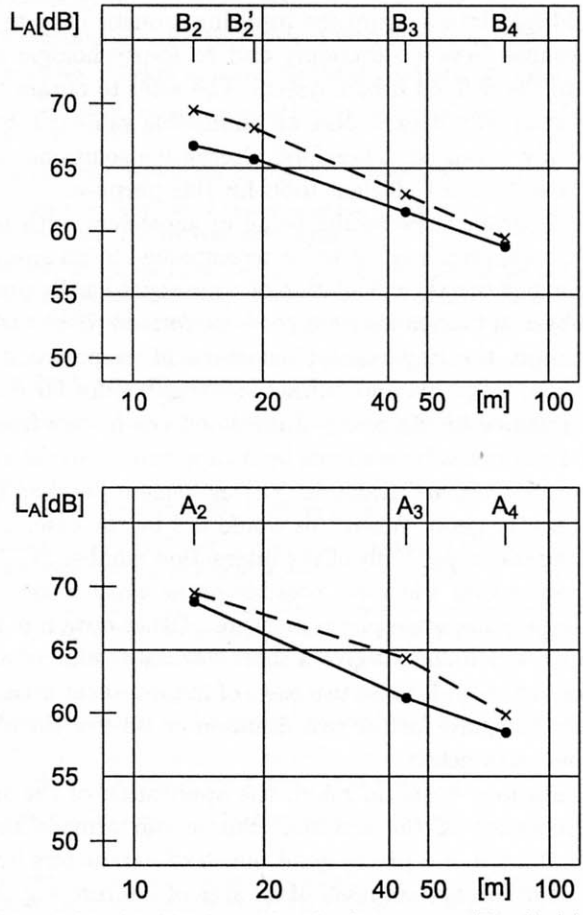

Fig. 4. The sound equivalent level in the analyzed urban system (Fig. 3): (•) – measured [14], (x) – calculated according to the PROP4 model.

the absolute value of the sound equivalent level L_{Aeq} at the observation point in an urban system (Eq. (29)). When a relative change in L_{Aeq} is awaited, L_{WA} is not needed. But the results depend still on the source model geometry with the assumed summation

step $\Delta x_E = 4\,\mathrm{m}$. In the analyzed case, although a single lane vehicle stream is assumed instead of the two lanes in the real situation, the agreement with experiment is very good. This means that the application of the PROP4 model, with the assumed source model and $K = 3$ interactions, gives a satisfactory accuracy in relation to the empirical data.

5. Conclusions

The operating of the urban infrastructures yields noise as by-product. The noise level is one of the comfort parameters of habituation. Thus decisions concerning the infrastructure should take into account the resulting acoustic climate; the final decisions should be a compromise between economy and socio-psychologic aspects of acoustic climate in relation to the defined urban system. The ways to obtain time-average sound levels in an area of interest not exceeding an admissible value can be different and not all of them are socially accepted. Therefore, alternative solutions should be prepared. Simulation models are the most efficient tools for this purpose.

Any simulation program gives results being in agreement with real records only in limited range. Thus, its application has to be accompanied by an analysis of accuracy. As for a system like an urban one the calculation of accuracy is hardly possible, a qualitative assessment of the physical foundations has to be performed. Here the presented PROP4 program holds for most the important phenomena of propagation in a system with obstacles: transmission, reflection and diffraction described for far field conditions. This choice seems to be justified for distances of few hundreds meters from the road.

How the PROP4 works has been shown by its application to the real urban situation for which field measurements are available. The agreement between the calculation and measured results is pretty good. When this would not be the case, an improvement can be achieved by raising the upper limit of the interaction number K. This results in more terms in the summation over the wave possible paths which raises generally the total acoustic pressure despite the wave phase inclusion. Other option is the decrease of the summation step Δx_E which should give a more accurate value of the sound exposure related to the vehicle drive-by. If these two ways of improvement do not work, this means that the model is not adequate for the real situation because of the physical foundations or the values of input parameters.

With all the limitations borne in mind, the application of the simulation program PROP4 for the forecasting of the acoustic climate can provide the ability to assess quantitatively the influence of a pretty good bunch of parameters involved in modeling of a noise source and urban system itself in an area of interest, e.g. in apartment house facades, recreation grounds.

References

[1] R. JANCZUR, E. WALERIAN and J. OGŁAZA, *Acoustical field in space with obstacles. Part I. Description of geometrical field*, Acustica, **78**, 154–162 (1993).

[2] E. WALERIAN and R. JANCZUR, *Acoustical field in space with obstacles. Part II. Propagation between buildings*, Acustica, **78**, 210–219 (1993).

[3] E. WALERIAN, *Multiple diffraction at edges and right angle wedges*, Acustica, **78**, 201–209 (1993).

[4] E. WALERIAN, *Description of noise propagation in a built-up area*, IFTR Reports, 29 (1995) .

[5] E. WALERIAN and R. JANCZUR, *Model of highway as noise source*, IFTR Reports 32 (1991).

[6] J.J. BOWMAN, T.B.A. SENIOR and P.L.E. USLENGHI [Eds.], *Electromagnetic and acoustical scattering by simple shapes*, Ch. 6, 8, North-Holland Company, Amsterdam 1969.

[7] E. WALERIAN and R. JANCZUR, *Theories of diffraction applied for description of acoustical field screen efficiency*, IFTR Reports, 25 (1985).

[8] E. WALERIAN, *Half-plane edge and right angle wedge as elements causing diffraction in urban area*, Archives of Acoustics, **12**, 157–189 (1988).

[9] J. SADOWSKI, *Architectural acoustics* [in Polish], PWN, Warszawa 1976.

[10] J. SADOWSKI, *Fundations of urban acoustics* [in Polish], Arkady, Warszawa 1982.

[11] R. MAKAREWICZ, *Theoretical foundation of urban noise control*, Journal of the Acoustical Society of America, **74**, 543–558 (1983).

[12] R. MAKAREWICZ, *Noise in environment* [in Polish], Center of Scientific Publication, Poznań 1996.

[13] M. STAWICKA-WAŁKOWSKA, *Acoustical factor in urban planning* [in Polish], Scientific Paper of the Building Research Institute, XLIII, Warszawa 1988.

[14] B. RUDNO-RUDZIŃSKA, *Modeling sound emission and propagation for prediction of the acoustic climate in urban environment* [in Polish], Scientific Papers of Institute of Telecommunication and Acoustics of Technical University of Wrocław No. 75, Monography No. 39, Wrocław 1994.

[15] K. ATTENBOROUGH *et al.*, *Benchmark cases for sound propagation model*, Journal of the Acoustical Society of America, **97**, 1, 173–191 (1995).

[16] Z. MAEKAWA, *Environmental acoustics update*, Journal of the Acoustical Society of Japan (E), **18**, 3, 97–107 (1997).

[17] T.F.W. EMBLETON, *Line integral theory of barriers attenuation in presence of the ground*, Journal of the Acoustical Society of America, **67**, 1, 42–45 (1980).

[18] T. ISEI, T.F.W. EMBLETON, J.E. PIERCY, *Noise reduction by barriers on finite impedance ground*, Journal of the Acoustical Society of America, **67**, 1, 46–58 (1980).

[19] D.A. HUTCHINS, H.W. JONES, L.T. RUSSEL, *Model studies of barrier performance in the presence of ground surface. Part I. Thin, perfectly reflecting barriers. Part II. Different shapes*, Journal of the Acoustical Society of America, **75**, 6, 1807–1826 (1984).

[20] A.G. GALAITSIS and W.N. PATTERSON, *Prediction of noise distribution in various enclosures from free-field measurements*, Journal of the Acoustical Society of America, **60**, 848–856 (1976).

[21] G. LEMIRE and J. NICOLAS, *Aerial propagation of spherical sound waves in bounded spaces*, Journal of the Acoustical Society of America, **86**, 5, 1845–1853 (1989).

[22] A.D. CLAYDEN, R.W.D. CULLEY, P.S. MARSH, *Modeling traffic noise*, Applied Acoustics, **8**, 1–12 (1975).

[23] R. JANCZUR, *Theoretical and scale-model investigation of a point source acoustical field in the presence of reflecting surfaces and screen*, (Ph.D. Thesis, IFTR Reports, 8 (1990).

[24] Y. SAKURAI, E. WALERIAN and H. MORIMOTO, *Noise barrier for building facade*, Journal of the Acoustical Society of Japan (E), **11**, 257–265 (1990).

[25] A.D. PIERCE, *Diffraction of sound around corners and over wide barriers*, Journal of the Acoustical Society of America, **55**, 5, 941–955 (1974).

[26] B. RUDNO-RUDZIŃSKA, J. JURKIEWICZ, *Application of the geometrical method for computer aided acoustic designing of urban system*, Proceedings of NOISE CONTROL'95, 343–348, Warszawa 1995.

[27] D. SOULAGE, C. SERVE, *Les logiciels cartbruit et microbruit*, Proceedings of 17th AICB Congress, 20–24, Prague 1992.

[28] M.E. DELANY, A.J. RENNIE and K.M. COLLINS, *A scale model technique for investigating traffic noise propagation*, Journal of Sound and Vibration, **56**, 3, 325–340 (1978).

[29] M. YAMASHITA and K. YAMAMOTO, *Scale model experiments for the prediction of road traffic noise and the design of noise control facilities*, Applied Acoustics, **31**, 185–196 (1990).

[30] S.A.L. GLEGG and J.R. YOON, *Determination of noise source heights, Part II. Measurement of the equivalent source height of highway vehicles*, Journal of Sound and Vibration, **143**, 39–50 (1990).

[31] R. MAKAREWICZ, *Traffic noise in a built-up area*, Applied Acoustics, **34**, 37–50 (1991).

[32] R. MAKAREWICZ, *Shielding of noise in a built-up area*, Journal of Sound and Vibration, **148**, 409–422 (1991).

[33] R. MAKAREWICZ, *Traffic noise in a built-up area influenced by the ground effect*, Journal of the Acoustical Society of Japan (E), **14**, 301–306 (1993).

[34] H.G. JONSSON, *A theory of traffic noise propagation with application to* L_{eq}, Journal of Sound and Vibration, **30**, 289–304 (1973).

[35] E. WALERIAN, R. JANCZUR, *Noise shielding efficiency in an urban system* [accepted for publication in Journal of Sound and Vibration].

[36] E. WALERIAN, R. JANCZUR, *Computer aid in urban planning*, Proceedings of the XLII Open Seminar on Acoustics, Warszawa – Białowieża, 373–376 (1995).

[37] K. ATTENBOROUGH, *Prediction ground effect for highway noise*, Journal of Sound and Vibration, **81**, 3, 431–424 (1982).

[38] K. RUDNO-RUDZIŃSKI, B. RUDNO-RUDZIŃSKA, *Statistics of wind and atmosphere equilibrium in investigation of sound propagation* [in Polish], Proceedings of the XLIII Open Seminar on Acoustics, Gliwice-Ustroń, 635–640 (1996).

[39] S. NAMBA, S. KUWANO, *Global environmental problems and noise*, Journal of the Acoustical Society of Japan (E), **14**, 3, 123–126 (1993).

[40] M. SASAKI, *The preference of the various sound in environment and the discussion about the concept of the sound-scape design*, Journal of the Acoustical Society of Japan (E), **14**, 189–195 (1993).

[41] K. HIRAMATSU, *Some aspects of soundscape studies in Japan*, Journal of the Acoustical Society of Japan (E), **14**, 133–138 (1993).

[42] K. ATTENBOROUGH, *Aspects of the new ISO standard for outdoor noise prediction*, Acoustics Bulletin, **21**, 1, 5–8 (1996).

[43] I. MALECKI, Z. ENGEL, A. LIPOWCZAN, J. SADOWSKI, *Problems of noise control in Poland on the way to European integration*, Proceedings of NOISE CONTROL'95, Warszawa, 1–39, 1995.

[44] R. KUCHARSKI, *Prediction of acoustical climate parameters in dwelling depending on terrain and noise sources characteristic* [in Polish], Ph.D. Thesis, Institute of Environmental Shaping, Warszawa 1990.

[45] P.T. LEWIS, *The noise generated by single vehicle in freely flowing traffic*, Journal of Sound and Vibration, **30**, 2, 191–206 (1993).

[46] R.R.K. JONES, D.C. HOTHERSALL, *Effect of operating parameters on noise emission from individual road vehicles*, Applied Acoustics, **13**, 2, 121–136 (1980).

[47] D.C. HOTHERSALL, S.N. CHANDLER-WILDE, *Prediction of the attenuation of road traffic noise with distance*, Journal of Sound and Vibration, **115**, 3, 459–472 (1987).

ARCHIVES OF ACOUSTICS
24, 2, 161–167 (1999)

HIGHER-ORDER SINGULARITIES OF THE EFFECTIVE PERMITTIVITY FUNCTION

W. LAPRUS

Polish Academy of Sciences
Institute of Fundamental Technological Research
(00-049 Warszawa, Świętokrzyska 21, Poland)

A method is given of calculating second-order singularities which are related to inflection points of slowness curves. An approximated formula is derived for the effective permittivity function in the neighbourhood of its singular points. A numerical analysis is presented of several piezoelectrics, and crystal cuts are calculated for the singular points. The analysis shows that inflection points may appear for almost every crystal cut, as is the case of lithium niobate and langasite.

1. Introduction

The effective permittivity [1, 2] of a piezoelectric half-space is a complex-valued function $Y(r)$ where r is the surface wave slowness. The well known Ingebrigtsen approximation of the imaginary part of this function is valid in the neighbourhood of the Rayleigh wave slowness r_{i}.

The function $Z(r) = 1/Y(r)$ is infinite for $r = r_{\mathrm{i}}$. Such a singularity of $Z(r)$ will be called zero-order. For $r < r_{\mathrm{i}}$ the function $Z(r)$ has three other singular points that coincide with cutoff slownesses of the three bulk waves. At these points $Z(r)$ is finite but its first derivative may be infinite. These are first-order singularities.

The Ingebrigtsen approximation has been improved by including contributions from the first-order singularities in the special case of SH waves [3]. In the general case, an approximation of the function $Z(r)$ has been found in the neighbourhood of the cutoff slowness r_{c} of bulk waves [4]. The method that leads to the approximation can be applied to the remaining two first-order singularities.

A slowness curve is described by the function $s = s(r)$, where $s(r)$ is the real part of the normal component of slowness (normal to the boundary of the the piezoelectric half-space). At the cutoff point of the curve, the first derivative of the inverse function $r = r(s)$ is equal to zero. The second derivative is usually different from zero, and is related to the curvature of the slowness curve at the cutoff point.

In the paper, we examine singularities of the function $Z(r)$ at points of a slowness curve different from the cutoff point and such that both the first and second derivative of the inverse function are equal to zero. These are inflection points of the slowness curve.

Such singularities of $Z(r)$ will be called second-order. At these points $Z(r)$ is finite but its first derivative may be infinite.

2. Second-order singularities

We adopt notations and conventions of Refs. [4] and [5]. The function $Z(r)$ is given by the equality $Z(r) = -Z_{44}^{-}(r)$, where Z_{44}^{-} is the element $(4,4)$ of the 4×4 matrix

$$Z_{KL}^{\pm} = R_{KJ}^{\pm} L_{JL}^{\pm} \tag{1}$$

with the minus superscript. This matrix is determined completely by eigenvectors of the eigenvalue problem that is related to the electro-mechanical field equations as explained in Ref. [4].

Suppose we know the function $s(r)$ that describes the slowness curve corresponding to the J-th eigenvalue in the (r,s) plane near the inflection point $(r_\mathrm{f}, s_\mathrm{f})$. Regarding the eigenvector $\widetilde{F}_K^{(J)}$ as a function of the variable s we can write, in the neighbourhood of r_f, the Taylor expansion

$$\widetilde{F}_K^{(J)}(s) = \widetilde{F}_K^{(J)}(s_\mathrm{f}) + \widetilde{F}_K^{\bullet(J)}(s_\mathrm{f})\,\Delta s, \tag{2}$$

where the higher-order terms are neglected. The dot denotes differentiation with respect to s, and $\Delta s = s - s_\mathrm{f}$.

In the neighbourhood of r_f the slowness curve can be approximated by an algebraic curve of third order. If the tangent to the slowness curve at the inflection point is parallel to the s axis then we may use the algebraic curve given by the equation

$$(s - s_\mathrm{f})^3 + \alpha^3 (r^3 - r_\mathrm{f}^3) = 0, \tag{3}$$

where α is a constant coefficient to be calculated. Hence

$$\Delta s = \alpha\, \varrho(r), \qquad \varrho(r) = (r_\mathrm{f}^3 - r^3)^{1/3}. \tag{4}$$

Straightforward differentiation of Eq. (3) with respect to s shows that $\alpha^3 = -2/r_\mathrm{f}^2 r^{\bullet\bullet\bullet}$, where $r^{\bullet\bullet\bullet}$ denotes the value of the third derivative for $s = s_\mathrm{f}$.

To calculate the coefficient α in terms of the derivatives with respect to r we choose another approach. Inflection points are located on slowness curves so that the tangent at an inflection point is usually not parallel to the s axis. In other words, the derivative s' (the prime denotes differentiation with respect to r) is finite for $r = r_\mathrm{f}$. The system of coordinates (x,y,z) should be rotated about the y axis by the angle $\zeta = -\mathrm{atan}(1/s'(r_\mathrm{f}))$ in order to make the tangent parallel to the s axis. This means that second-order singularities of $Z(r)$ appear only for particular crystal cuts. Now, the coefficient α can be calculated for an arbitrary inflection point, and then used in Eq. (3) after a suitable rotation of the system of coordinates. We have

$$\alpha^3 = 2(1 + (s')^2)^3 / s'''(r_\mathrm{f} s' - s_\mathrm{f})^2, \tag{5}$$

where s' and s''' denote the values of the derivatives for $r = r_\mathrm{f}$.

The value of s is changing fast for $r \to r_f$ (the first derivative of s tends to infinity in the rotated system of coordinates), and so do the corresponding eigenvalue $q^{(J)}$ and eigenvector $\widetilde{F}_K^{(J)}$. Other eigenvalues and eigenvectors may be considered constant in the neighbourhood of r_f. Thus, it suffices to take into account only the eigenvector $\widetilde{F}_K^{(J)}$, to find its approximation given by Eq. (2), and to calculate the function $Z(r)$ with the use of Eq. (1).

Since $s(r) = q(r)\, r$, then

$$s' = q'r + q, \qquad s'' = q''r + 2q', \qquad s''' = q'''r + 3q'' \tag{6}$$

(here $s(r)$ denotes a complex-valued function). The derivatives q', q'', q''', and $\widetilde{F}_K^{\bullet(J)}$ can be found as follows.

Denote by $\mathcal{H}_{KL}^{(J)}$ the difference $H_{KL} - q^{(J)} I_{KL}$ where I_{IJ} is the identity matrix. The equality

$$\mathcal{H}_{KL}^{(J)} \widetilde{F}_L^{(J)} = 0 \tag{7}$$

is satisfied for every r. Differentiating the both sides of Eq. (7) with respect to r gives the recurrence of equalities

$$\mathcal{H}_{KL}^{\prime(J)} \widetilde{F}_L^{(J)} + \mathcal{H}_{KL}^{(J)} \widetilde{F}_L^{\prime(J)} = 0, \tag{8}$$

$$\mathcal{H}_{KL}^{\prime\prime(J)} \widetilde{F}_L^{(J)} + 2\mathcal{H}_{KL}^{\prime(J)} \widetilde{F}_L^{\prime(J)} + \mathcal{H}_{KL}^{(J)} \widetilde{F}_L^{\prime\prime(J)} = 0, \tag{9}$$

$$\mathcal{H}_{KL}^{\prime\prime\prime(J)} \widetilde{F}_L^{(J)} + 3\mathcal{H}_{KL}^{\prime\prime(J)} \widetilde{F}_L^{\prime(J)} + 3\mathcal{H}_{KL}^{\prime(J)} \widetilde{F}_L^{\prime\prime(J)} + \mathcal{H}_{KL}^{(J)} \widetilde{F}_L^{\prime\prime\prime(J)} = 0. \tag{10}$$

Let $\widetilde{E}_L^{(I)}$ be the left eigenvector corresponding to the eigenvalue $q^{(I)}$. We assume the normalization

$$\widetilde{F}_L^{(J)} \widetilde{F}_L^{(J)} = 1, \qquad \widetilde{E}_L^{(I)} \widetilde{F}_L^{(J)} = I_{IJ} \tag{11}$$

for every r, and introduce the symbols

$$Q_1^{(IJ)} = \widetilde{E}_K^{(I)} H'_{KL} \widetilde{F}_L^{(J)}, \qquad Q_2^{(IJ)} = \widetilde{E}_K^{(I)} H''_{KL} \widetilde{F}_L^{(J)}, \qquad Q_3^{(IJ)} = \widetilde{E}_K^{(I)} H'''_{KL} \widetilde{F}_L^{(J)}. \tag{12}$$

Multiplying each of Eqs. (8) – (10) by $\widetilde{E}_K^{(J)}$ we obtain

$$q'^{(J)} = Q_1^{(JJ)}, \tag{13}$$

$$q''^{(J)} = Q_2^{(JJ)} + 2\widetilde{E}_K^{(J)} \mathcal{H}_{KL}^{\prime(J)} \widetilde{F}_L^{\prime(J)}, \tag{14}$$

$$q'''^{(J)} = Q_3^{(JJ)} + 3\widetilde{E}_K^{(J)} \mathcal{H}_{KL}^{\prime\prime(J)} \widetilde{F}_L^{\prime(J)} + 3\widetilde{E}_K^{(J)} \mathcal{H}_{KL}^{\prime(J)} \widetilde{F}_L^{\prime\prime(J)}. \tag{15}$$

The derivatives $\widetilde{F}_L^{\prime(J)}$ and $\widetilde{F}_L^{\prime\prime(J)}$ can be represented as linear combinations of eigenvectors, i.e.

$$\widetilde{F}_L^{\prime(J)} = \sum_I C_{IJ}^1 \widetilde{F}_L^{(I)}, \qquad \widetilde{F}_L^{\prime\prime(J)} = \sum_I C_{IJ}^2 \widetilde{F}_L^{(I)}, \tag{16}$$

where the constants C_{IJ}^1 and C_{IJ}^2 are to be calculated.

Inserting $\widetilde{F}_L^{\prime(J)}$ from Eq. (16) into Eq. (14) and taking into account Eq. (8) we obtain

$$q''^{(J)} = Q_2^{(JJ)} + 2 \sum_{I \neq J} C_{IJ}^1 Q_1^{(JI)}, \tag{17}$$

where $C^1_{IJ} = -(q^{(I)} - q^{(J)})^{-1} Q_1^{(IJ)}$ for $I \neq J$, and

$$\widetilde{F}_L^{\prime(J)} = C^1_{JJ} \widetilde{F}_L^{(J)} + \widetilde{D}_L^{1(J)}, \tag{18}$$

where $C^1_{JJ} = -\widetilde{D}_L^{1(J)} \widetilde{F}_L^{(J)}$, and $\widetilde{D}_L^{1(J)} = \sum_{I \neq J} C^1_{IJ} \widetilde{F}_L^{(I)}$.

Similarly, inserting $\widetilde{F}_L^{\prime\prime(J)}$ from Eq. (16) into Eq. (15), and taking into account Eq. (9) and the last results, we obtain the derivative $q^{\prime\prime\prime(J)}$ given by Eq. (15) with

$$\widetilde{F}_L^{\prime\prime(J)} = C^2_{JJ} \widetilde{F}_L^{(J)} + \widetilde{D}_L^{2(J)}, \tag{19}$$

where $C^2_{JJ} = -\widetilde{D}_L^{2(J)} \widetilde{F}_L^{(J)} - \widetilde{F}_L^{\prime(J)} \widetilde{F}_L^{\prime(J)}$, $\widetilde{D}_L^{2(J)} = \sum_{I \neq J} C^2_{IJ} \widetilde{F}_L^{(I)}$, and

$$C^2_{IJ} = \left(q^{(I)} - q^{(J)}\right)^{-1} \left(-Q_2^{(IJ)} + 2 \left(q^{\prime(I)} - q^{\prime(J)}\right)^{-1} Q_1^{(IJ)} + 2 \sum_{K \neq I} (q^{(K)} - q^{(J)})^{-1} Q_1^{(KJ)} Q_1^{(IK)} \right) \tag{20}$$

for $I \neq J$ and $K \neq J$.

The above formulae are true for all eigenvalues and eigenvectors (for r different from the cutoff values). In this way, we find the coefficient α from Eq. (5), and the derivative $\widetilde{F}_K^{\bullet(J)}(s) = \widetilde{F}_K^{\prime(J)}(r)/s'(r)$.

Inserting the eigenvector given by Eq. (2) into Eq. (1) we get the approximated matrix

$$Z^{\pm}_{KL}(r) = Z^{\pm(0)}_{KL} \pm Z^{\pm(1)}_{KL} \alpha \varrho(r) \tag{21}$$

(the higher-order terms are neglected) where the constant matrices $Z^{\pm(0)}_{KL}$ and $Z^{\pm(1)}_{KL}$ can be easily expressed in terms of $\widetilde{F}_K^{(J)}$, $\widetilde{F}_K^{\bullet(J)}$, and the remaining seven eigenvectors for $r = r_{\mathrm{f}}$ (see Appendix of Ref. [4]). In particular,

$$Z(r) = Z_0 - Z_1 \alpha \varrho(r), \tag{22}$$

where the coefficients Z_0 and Z_1 are the elements (4,4) of the corresponding matrices in Eq. (21).

3. Numerical search of inflection points

The location of inflection points on slowness curves is calculated with the use of numerical procedures similar to those described in Ref. [5]. The main procedure solves the eigenvalue problem associated with the field equations. A scanning is performed over crystal cuts (triplets of Euler angles) for several piezoelectric media. The calculations shows that for some crystal cuts there is more than 10 inflection points, and that inflection points may appear for almost every cut (the case of lithium niobate and langasite) or for only a minority of crystal cuts (the case of bismuth germanium oxide).

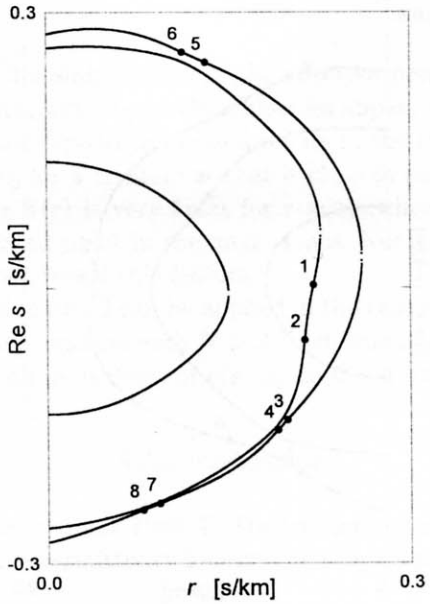

Fig. 1. Inflection points for lithium niobate (Euler angles: 20°, 160°, 120°).

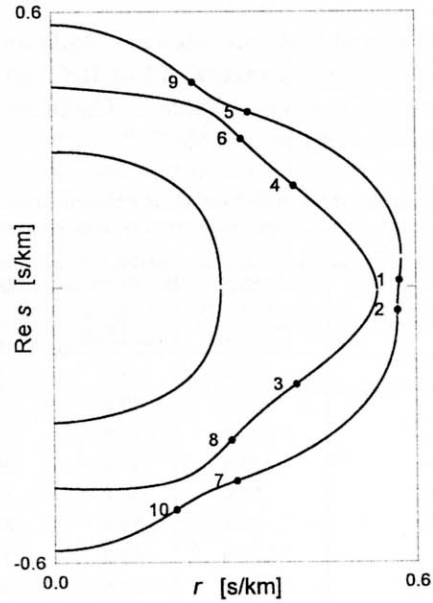

Fig. 2. Inflection points for bismuth germanium oxide (Euler angles: 0°, 40°, 20°).

Three examples of location of inflection points are given in Figs. 1 to 3 for lithium niobate, bismuth germanium oxide, and langasite. The crystal cuts have been chosen from those with a large number of inflection points. It should be noted that some inflec-

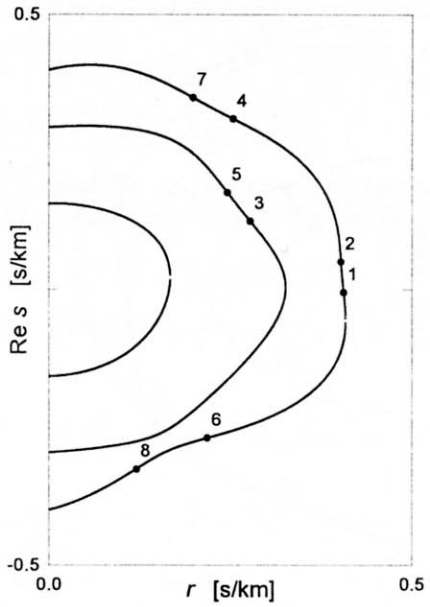

Fig. 3. Inflection points for langasite (Euler angles: 10°, 40°, 40°).

tion points may be missing due to finite precision of calculations. The appendices of the slowness curves above the cutoff points (cf. Fig. 1 of Ref. [4]) have been omitted. The angle ζ for each inflection point is given in Table 1. The inflection points are numbered in the order of decreasing values of the variable r.

Table 1. The angle ζ corresponding to the inflection points shown in the figures for lithium niobate (LNO), bismuth germanium oxide (BGO), and langasite (LGS).

Inflection Point No.	LNO 20 160 120 ζ [deg]	BGO 0 40 20 ζ [deg]	LGS 10 40 40 ζ [deg]
1	−9.2	−5.3	4.5
2	−4.9	−0.6	2.9
3	−34.9	−45.8	31.5
4	−34.4	42.7	56.6
5	59.6	65.4	30.3
6	58.3	38.2	−69.9
7	−62.9	−65.2	54.1
8	−62.7	−36.9	−50.4
9	–	43.6	–
10	–	−50.7	–

It is obvious that inflection points appear in pairs. A pair of inflection points is related to a concave portion of a slowness curve, which is delimited by the two points of the pair.

4. Conclusion

In contrast to first-order singularities of the effective permittivity function, which appear for every crystal cut, second-order singularities appear only for particular crystal cuts. These crystal cuts correspond to isolated points in the three-dimensional space of Euler angles. Nevertheless, for a crystal cut that is close to one of those points the first derivative of the function $Z(r)$ is very great for $r \approx r_{\mathrm{f}}$, where r_{f} is the singular point corresponding to the isolated point in the angle space. Numerical calculation of values of the function $Z(r)$ cannot reveal this feature.

The method presented in Sec. 2 can be applied in the case of N-th-order singularities of the effective permittivity function with $N > 2$. Such singularities are related to points of slowness curves where all derivatives of $r(s)$ up to the N-th-order are zero.

Acknowledgement

The author would like to thank Prof. E. Danicki for suggesting the investigation of singularities of the effective permittivity function and for discussions helpful in calculating the approximation.

This work was supported by Committee of Scientific Research (Poland) under Grant No. 7 T07A 049 13.

References

[1] K.A. Ingebrigtsen, *Surface waves in piezoelectrics*, J. Appl. Phys., **40**, 2681–2686 (1969).

[2] K. Bløtekjaer, K.A. Ingebrigtsen, and H. Skeie, *A method for analyzing waves in structures consisting of metal strips on dispersive media*, IEEE Trans. Electron Devices, **ED-20**, 1133–1138 (1973).

[3] E. Danicki, *New theory of SSBW devices*, [in:] 1980 IEEE Ultrasonics Symposium Proceedings, B.R. McAvoy [Ed.], IEEE, New York, 1980, pp. 235–239.

[4] W. Laprus and E. Danicki, *Singularities of the planar Green function in the spectral domain*, Archives of Acoustics, **22**, 169–177 (1997).

[5] W. Laprus and E. Danicki, *Piezoelectric interfacial waves in lithium niobate and other crystals*, J. Appl. Phys., **81**, 855–861 (1997).

ARCHIVES OF ACOUSTICS
24, 2, 169–177 (1999)

THE INFLUENCE OF THE REDUCTION METHODS OF THE CONCRETE HARDENING TIME ON THE PARAMETERS OF THE GENERATED ACOUSTIC EMISSION SIGNAL MEASURED IN PLAIN AND IN HIGH STRENGTH CONCRETES

Z. RANACHOWSKI

Polish Academy of Sciences
Institute of Fundamental Technological Research
(00-049 Warszawa, Świętokrzyska 21, Poland)

J. HOŁA

Institute of Civil Engineering
Wrocław University of Technology
(50-377 Wrocław, pl. Grunwaldzki 11, Poland)

K. POGAN

(30-552 Kraków, ul. Wielicka 89/72)

Results of the Acoustic Emission (AE) measurements including: AE counts sum, averaged AE event power and averaged AE events spectral pattern are presented in dependence on the concrete mixture type and on the used thermal treatment method. Six compositions differing in the compression strength were examined. Four of them were those of plain concrete and the remaining two were silica — fume modified compositions. The results let the authors to conclude that there is a correlation between the two AE signal parameters: the AE counts sum and the averaged AE events spectral pattern and the applied thermal treatment procedure and, further, that the nature of the so induced changes of the AE parameters is similar for all the six concrete compositions tested.

1. Introduction

The stress wave caused by the energy release in stressed solids is called the Acoustic Emission (AE) effect. In concrete, the major AE sources are: crack growth, crack formation and friction processes. The nature of the AE signal generation enables the inspection of the state of constructional elements under the mechanical load. The frequency band of the AE signal generated in concrete elements is considered to lie approximately within the limits 10 kHz – 1000 kHz and, respectively the AE activity duration may vary from miliseconds to several days. The AE signal is measured by a piezoelectric sensor coupled

to the element under test. The commonly used AE activity parameter is called "AE count rate" and denotes the number of crossings over the preset level by the AE signal. When the most common form of the AE event — a damped sinusoid is considered, the dependence between the AE signal amplitude A_m the centre frequency f_0, the count rate N_c and the preset signal level A_t can be described by the formula [1]:

$$N_c = f_0/\alpha_1 \ln(A_m/A_t), \tag{1}$$

where α_1 is the damping factor of the oscillations within the AE event.

Some authors have investigated the dependence between the compression strength of the concrete elements and the AE count sum registered during the process of loading [1–3, 5]. For the quasi-axial compression test made on 100 mm cubes, for which the 28 days compressive strength was designated within the range of 25 – 65 MPa, it was found that the total count sum $\sum N_{\mathrm{EA}}$ registered during the entire compression test depends on the composition compressive strength, R, according to the formula [4]:

$$\sum N_{\mathrm{EA}} = 814.8 \cdot R^2 - 55121 \cdot R + 10^6. \tag{2}$$

The power of the EA signal is proportional to the square of the averaged value of A_m within the measuring cycle Δt. The latter AE parameter is less preferred for the description of the AE generation process because it is affected by the scattering and damping effects caused by internal heterogenities of the tested material. However, there is also a correlation between the spectral patterns of the AE sources and the mechanical properties of the investigated object. The spectral characteristic of the AE signal registered by the AE sensor can be described by the following model [6]. The crack area generating EA is substituted by the inclusion zone V_0^*. The zone can be characterized by the same elastic constants as the remaining body with the addition of the non-elastic coefficient $\beta_{ij}^*(x,t)$. The latter should be put in the formula describing the displacement tensor in the discussed body when the displacement was activated by a Gaussian — shape disturbance of the local stress equilibrium. In this case the frequency-domain response registered by the sensor that converts the displacement appearing along the z axis into an electrical signal characterised by the electric potential V, can be described with the following formula:

$$|V(\omega)| = \frac{2\mu\Delta\varepsilon_{33}^* + \lambda\Delta\varepsilon_{33}^*}{4\pi\varrho r v_L^3} V_0^* P_0 \exp(-\omega^2\tau^2), \tag{3}$$

where: ω — pulsation of the frequency-domain EA signal registered by the sensor, Δ — "source rise time" equals 4τ [s], ε_{33}^* — component of the displacement vector used to characterize the inclusion zone V_0^* and proportional to the displacement direction, ϱ — material density, r — AE source — sensor distance, v_L — dilatation wave mode velocity, λ, μ — Lamé constants of the investigated body, P_0 — coefficient characterizing the sensivity of the AE sensor within the arbitrary chosen AE registration frequency range.

The parameter $|V(\omega)|$, averaged for an equal number of AE events registered during the experiment and calculated for certain values of the frequency $f = 2\pi\omega$, was by the authors of this paper called the averaged AE event spectral pattern, and used as the characteristic parameter for the investigated compositions. In the following chapters, the

correlation between the total count sum $\sum N_{EA}$ and the averaged AE event spectral patterns, registered before and after the heat treatment on dependence on the compression strength of different concrete compositions, is presented.

2. Experimental

Six concrete compositions differing in their compressive strength were prepared for the investigation. The compositions labelled 1, 3, 5 were based on crushed aggregates and the remaining three ones were based on river aggregates. A plasticizer was added to the compositions labelled 3, 4, 5, 6; silica fume was added to the compositions labelled 5 and 6. The water to cement ratios for the mixes 1 to 6 were: 0.6, 0.6, 0.45, 0.45, 0.3, 0.3. Each of the composition reached the maturity in one of the four following respects: staying at room temperature within 28 days or passing one of the three schemes of thermal treatment: "mild", "intermediate" and "rapid". The specimens were dismantled 1.5 hour before the start of the thermal treatment. In all schemes of the thermal treatment the same temperature levels were applied. The "mild" cycle lasted for 9.5 hours. The duration of the "intermediate" cycle was 40% of the "mild" one and that of the "rapid" cycle was 25% of the "mild" one. The increase coefficients of temperature vs. time were for the three cycles mentioned as follows: 20, 24, and 30 degrees per second. For each of the compositions the compressive strength was measured for ten cubic $100 \times 100 \times 100$ mm specimen by a quasi-axial compression test. In addition, the compression test was performed for the following three groups of specimen series: a) 28 days maturity under normal conditions; b) immediately after thermal treatment; c) 28 days maturity after thermal treatment. For ten specimens of each of the groups described above, the acoustic emission parameters were measured during the compression test. The AE measurements were made using a broadband AE sensor of type WD (Phycical Acoustic Corp., USA), an Acoustic Emission Analyser Type EA 100 and the 2.5 MHz A/D converter computer extension card. The process of the event recording was activated when the applied stress in the loaded sample reached 0.6 of the estimated rupture, shown in first column and in the first six rows of Table 1.

The following AE parameters were registered for further investigation: a) total AE counts sum registered during the compression test; b) 50 bytes long spectral patterns of AE events captured by the A/D converter card. Ca. 50 spectral patterns were recorded during the loading of each specimen. The consecutive bytes in the registered spectral patterns represent the AE signal power in the consecutive 20 kHz — wide subranges of the 1 MHz range of the analysed spectrum. It was proved after the registration that the dispersion of the averaged subrange power levels, derived from 100 recorded waveforms, is less than 10% when the different 100 — member sets of waveforms are averaged. Therefore, a common spectral pattern could be obtained for each concrete composition regardless of the number of specimens used to derive the 100 — member waveforms set. Using the averaged AE spectral patterns, two parameters were calculated. The first one was the average AE events power. To calculate this parameter, the power levels registered in all subranges were totalised. The second parameter was the average ratio of the AE

Table 1. The influence of the heat treatment scheme to the measured parameters for six investigated concrete compositions.

Composition Code	Compressive strength [MPa]	Strength rel. to measure in norm. cond. [%]	AE count sum [$N \times 1000$]	Count sum rel. to measure in normal cond. [%]	Average AE events power [arb.u.]	ev. power rel. to measure in norm. cond. [%]	Coeff. M/H [−]	Coeff. M/H average for maturing mode [−]
1	2	3	4	5	6	7	8	9
Hydration process at room temperature								
N1	25.9		277		174		1.25	
N2	24.4		216		183		0.91	
N3	34.8	100%	139	100%	210	100%	1.29	1.10
N4	35.9		176		176		1.14	
N5	63.6		886		179		0.87	
N6	52.1		471		145		1.65	
Rapid heat treatment								
R1	11.7	45	50	18	139	80	1.54	
R2	9.4	38	37	17	156	85	1.23	
R3	13.3	38	49	35	150	71	1.58	1.49
R4	12.8	35	19	10	156	89	1.57	
R5	45.8	72	370	42	166	93	1.46	
R6	36.3	70	485	103	156	108	1.56	
Rc1	23.4	90	343	124	163	94	1.00	
Rc2	19.5	80	302	140	151	82	1.07	
Rc3	25.3	73	198	142	162	77	1.72	1.27
Rc4	22.3	62	183	103	161	91	1.38	
Rc5	48.6	76	439	49	148	83	1.14	
Rc6	40.3	77	442	93	149	103	1.29	
Intermediate heat treatment								
I1	11.5	44	50	18	134	77	1.70	
I2	11.8	48	32	15	130	71	1.75	
I3	16.6	48	60	43	161	77	1.73	1.73
I4	17.3	49	61	35	144	82	1.81	
I5	52.0	82	407	51	144	80	1.71	
I6	44.0	84	357	76	146	101	1.61	
Ic1	21.1	81	374	135	148	85	1.20	
Ic2	20.4	84	355	164	147	80	1.11	
Ic3	29.3	84	213	153	144	69	1.41	1.20
Ic4	25.3	70	199	113	139	79	1.40	
Ic5	54.9	86	380	43	156	87	1.07	
Ic6	47.0	90	355	75	161	111	1.05	

Table 1. [cont.]

1	2	3	4	5	6	7	8	9
Mild heat treatment								
M1	13.5	52	80	29	150	86	1.71	
M2	13.1	54	85	39	157	85	1.52	
M3	15.6	45	71	51	151	72	1.50	1.58
M4	22.7	63	95	54	159	90	1.65	
M5	53.8	85	246	28	157	88	1.70	
M6	42.8	82	217	46	159	109	1.46	
Mc1	22.7	88	303	109	155	89	1.11	
Mc2	22.8	93	318	147	156	85	1.02	
Mc3	24.2	69	194	139	158	75	1.67	1.38
Mc4	26.7	74	181	102	143	81	1.52	
Mc5	57.2	90	257	29	159	89	1.27	
Mc6	46.8	90	266	56	158	108	1.74	

event power measured within the frequency range 50 – 400 kHz to that one measured in the frequency range 400 kHz to 800 kHz. To calculate this second parameter, the power levels registered in the two subranges mentioned above were totalised and then their ratio was calculated. The latter parameter was denoted as M/H. One of the aims of this investigation was to determine whether the structural and the maturing conditions correlate with the AE event spectral pattern changes; this correlation is represented with M/H parameter. The measured AE counts sums and rupture forces, measured for all composition sets of the specimens did not differ from each other by more than 10% within the set.

The basic composition parameters as well as the major test results are collected in Table 1. The following code was used to determine the sample series type listed in the table. The n1...n6: the 28 days maturing process under normal conditions; r1...r6: the maturing process when the rapid thermal treatment was applied and the compression test was performed immediately after the heating; rc1...rc6: the maturing process when the rapid thermal treatment was applied and the compression test was performed 28 days after the heating; i1...i6: the maturing process when the intermediate thermal treatment was applied and the compression test was performed immediately after the heating; ic1...ic6: the maturing process when the intermediate thermal treatment was applied and the compression test was performed 28 days after the heating; m1...m6: the maturing process when the mild thermal treatment was applied and the compression test was performed immediately after the heating; mc1...mc6: the maturing process when the mild thermal treatment was applied and the compression test was performed 28 days after the heating. The data presented in Table 1 include: rupture level measured in the specimen during the compression test, registered AE count sum, average AE event power and the M/H parameter. To enable the further analysis, the relative changes of the above parameters in respect to the values measured in the n1..n6 series were also put in the Table 1.

3. Discussion of the results

The relation of the total count sum $\sum N_{EA}$ vs. the registered compressive strength R_N measured for the series n1..n6 shows good agreement with the formula (2) which was found for the compositions hardening at room temperature. In the other series, the thermal treatment caused a loss of the compressive strength R_T. For all the six investigated compositions, the averaged loss of the compressive strength ratio, calculated as R_T/R_N equalled ca. 50% for the measurements made immediately after the heat treatment. The loss was reduced to ca. 20% for the measurements made 28 days after the heat treatment. It is worthy of mentioning that the relative changes of $\sum N_{EA}$ measured after the heat treatment and related to the normal hardening conditions were similar within the majority of the investigated compositions. For higher losses of compressive strength, there is a good agreement between the AE counts sum and the compressive strength changes. The dispersion of the AE counts sum rises dramatically for minor compressive strength losses measured for the samples after 28 — days curing. The results described above and the possible linear regression curve parameters are shown in Fig. 1.

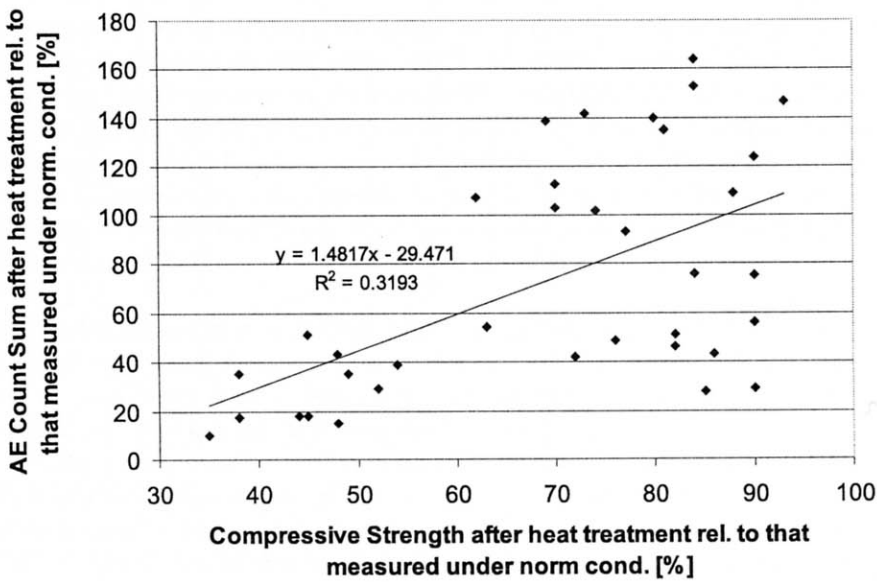

Fig. 1. The dependence of the AE count sum measured in the samples after thermal treatment and related to the AE count sum measured in samples hardened under normal conditions versus compressive strength ratio measured in the similar two sample series.

The investigation results presented in Table 1 state that there is no clear correlation between the averaged AE event power and the hardening conditions. In most of the compositions a slight loss of the averaged AE event power could be observed when thermal treatment was applied. The spectral contents of the AE signal generated in stressed concrete compositions, however, changes proportional to the degree of damages caused by the thermal treatment. To capture these changes, 100 waveforms of the AE events, each

100 bytes long were registered for every composition and heat treatment scheme. After the computer processing of this data averaged spectral patterns corresponding to the described sample series were constructed. The specific parameter, denoted M/H, was chosen to find if there is any correlation between the compression strength loss caused by the heat treatment (defined as R_N/R_T) and the averaged AE event spectral patterns. The M/H parameter was defined as the ratio of the averaged power in the range 50 kHz – 400 kHz to the averaged power in the range 400 kHz – 800 kHz for the registered AE events. The data presented in the Table 1 let the authors to point out the following conclusions.

The increase of the compressive strength causes an increase of the AE signal power in the high frequency range H. The high frequencies are generated in areas in that the local stress level had reached the relatively high value. This relation is shown in Fig. 2.

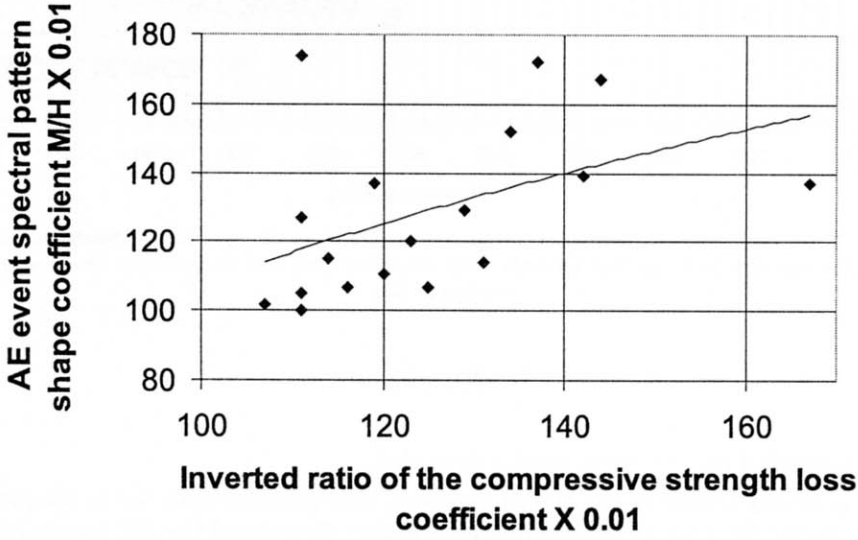

Fig. 2. The correlation between the spectral pattern shape coefficient M/H and the inverted compressive strength loss coefficient defined as R_N/R_T.

Typical spectral patterns of the averaged AE event registered for the three levels of the compression strength loss discussed above are shown in Fig. 3.

The compositions n1..n5, hardened at normal conditions generated a considerable amount of the AE event power in the high frequency range and, therefore, the M/H coefficient for these compositions was relatively low (approx. 1.0). In the compositions for which the heat treatment was applied and, additionally 28 days of hardening was effected, the average M/H coefficient level was within the range of 1.1 – 1.5. If the M/H coefficient was measured immediately after the heat treatment when most of the significant loss of the compressive strength occurred, the M/H coefficient exceeded the 1.5 level. Therefore the M/H parameter, derived from the AE signal, might be applied as a measure of the degradation of the concrete structure.

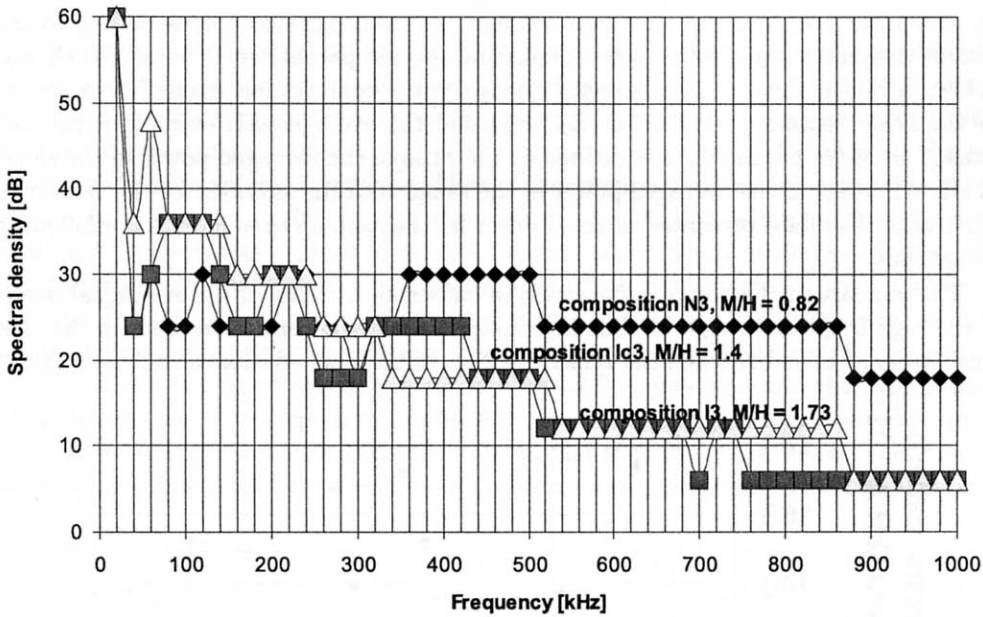

Fig. 3. Three averaged AE event spectral patterns registered in the composition hardened under normal conditions (N3), 24 days after the heat treatment (Ic3) and immediately after the heat treatment (I3).

4. Conclusions

The presented measurement results show that:

a) a generally higher loss of the compression strength caused by faster temperature changes during the heat treatment implies a higher decrease of the AE counts sum (as shown in Fig. 1),

b) regardless of the heat treatment method applied, the registered AE counts sum value in high strength concrete compositions is 200–300% higher than in weaker plain concretes matured under the same conditions.

The above conclusions let the authors state that the AE counts sum may be applied as a parameter correlating with the mechanical strength level of the investigated compositions.

The higher level of the compressive strength causes an increase of the AE signal power in the high frequency range H. The high frequencies are generated in the areas in that the local stress level reaches a relatively high value (as shown in Fig. 2); therefore the average spectral pattern of the AE events registered during the compression test also depends on the mechanical strength of the tested composition. This both the AE parameters described above can be useful in the comparison of the mechanical properties of concrete compositions.

References

[1] Z. RANACHOWSKI, *Methods of the measurement and analysis of the acoustic emission signal* [in Polish], IFTR Reports, 1/1997, IFTR, Warszawa 1997.

[2] J. HOŁA, Z. RANACHOWSKI, *Application of AE method to determination of technological and exploatation parameters to destruction process in concrete* [in Polish], IFTR Reports, 37/1992, Warszawa 1992.

[3] A. JAROSZEWSKA, J. RANACHOWSKI, F. REJMUND, *Acoustic emission in concrete under thermal and mechanical stress* [in Polish], [in:] Modern opinions on destruction processes of bones, ceramics and concrete, Collected Papers, J. RANACHOWSKI [Ed.], IFTR, Warszawa 1995.

[4] J.-M. BERTHELOT, M. BEN SOUDA, J.L. ROBERT, *Frequency analysis of acoustic emission signals in concrete*, Journal of Acoustic Emission, **11**, 1, 11–18 (1993).

[5] J. MIERZWA, K. POGAN, Z. RANACHOWSKI, *The correlation between the fracture induced acoustic emission and the compressive static strength in plain and high strength concrete*, Archives of Acoustics, **22**, 3, 333–342 (1997).

[6] K. POGAN, *Frequency characteristic of the acoustic emission signal in concrete under compressive loading*, Archives of Acoustics, **23**, 3, 426–434 (1998).

[7] T. TAKASHIMA, Y. HIGO, S. NUNOMURA, *Determination of the duration of transient phenomena by frequency-domain analysis of AE*, Philosophical Magazine A, **49**, 2, 221–229 (1984).

ARCHIVES OF ACOUSTICS
24, 2, 179–190 (1999)

THE INFLUENCE OF ACOUSTIC NONLINEARITY ON ABSORPTION PROPERTIES OF HELMHOLTZ RESONATORS PART I. THEORY

M. MEISSNER

Polish Academy of Sciences
Institute of Fundamental Technological Research
(00-049 Warszawa, Świętokrzyska 21, Poland)

This is the first of two companion papers concerned with the nonlinear absorption of Helmholtz resonators at a high amplitude incident wave. The phenomenon has been examined theoretically by use of a model of the acoustic field in the neighbourhood of the resonator placed at the end of cylindrical tube. The calculation results have shown that the peak of the absorption coefficient occurs when the nonlinear resistance is equal to the radiation resistance of the resonator. The full experimental investigations of this phenomenon and a comparison between theoretical and experimental data will be presented in the companion paper (Part II).

1. Introduction

The nonlinear properties of Helmholtz resonators occur due to the dependence of the resonator resistance on the particle velocity in the orifice. In the case of large amplitudes of velocity a part of acoustic energy is lost on account of turbulent motion nearby the edge of the orifice. The transfer of acoustic energy to the nonacoustic kinetic energy of these turbulences influences the variability of the absorption coefficient of resonator in the function of the sound intensity.

Nonlinear studies of Helmholtz resonators are scarce in number and relatively recent. Important among these are the experimental investigations by INGARD [1], BIES and WILSON [2], CZARNECKI [3, 4], WU and RUDNICK [5], as well as the theoretical work of ZINN [6]. One of the important results of these investigations is the observation that the resistance of a Helmholtz resonator increases with growing an amplitude of incident pressure. CZARNECKI [3] investigated an influence of the nonlinear properties of Helmholtz resonators on acoustic conditions in enclosures. He found an increase or a decrease of the absorption coefficients depending on the conditions of the resonator surroundings. WU and RUDNICK [5] measured a variation in the resonant frequency at high sound intensities. They observed shifts of the tuning curves of resonators towards higher frequencies with increasing amplitude of sound pressure. They ascribed these shifts to decrease of the end correction of the resonators at higher sound pressure.

The aim of this first of the two companion papers is to offer a theoretical model of the energy absorption mechanism, that occurs when a single Helmholtz resonator is excited by high amplitude plane wave. In the analysis it is considered the case of low frequency incident wave. The theoretical description of the acoustic field is based on the momentum equation for incompressible fluid in the space with rotating fluid motion and Bernoulli's equation in the space where fluid motion is irrotational. In this manner, the assumption used in earlier theoretical studies of acoustic nonlinearity [7, 8] that the fluid motion might be treated as being irrotational is removed. A loss resistance derived from the theoretical analysis is included in an impedance model of resonator to explain a change in absorption coefficient of the resonator. In the second paper [9] the comparison between experimental results and theoretical data will be presented.

2. Nonlinear effect at high amplitude incident sound

The present theoretical study is concerned with the interaction between high amplitude sound wave and a Helmholtz resonator placed at the end of cylindrical tube. The resonator consists of a part of this tube, and at one end it is terminated by rigid wall, while at the other one by a rigid plate with a centrally located circular orifice. The resonator dimensions are considerably smaller than the acoustic wavelength. When the amplitude of incident wave is large, the instantaneous flow pattern is different on both sides of the resonator orifice. In the first place, attention is focused on a flow structure during the first half of the cycle, when the flow is directed from tube to the resonator cavity (Fig. 1). Inside the tube, in the acoustic far field, the streamlines are parallel because only plane waves propagate in the area lying a long distance from the resonator. At the inflow side of the orifice the streamlines converge producing an acoustic near field, in which a reactive part of acoustic energy is concentrated. At the high amplitude of incident sound and a small ratio between orifice and tube diameters, there is a strong acoustic flow through the orifice which results in the separation of boundary layer and the formation of high velocity axial jet. When the edges of the orifice are sharp, the streamlines in the jet somewhat converge forming so-called *vena contracta*. The viscous interaction of the jet with the quiescent surroundings results in the formation of vortex ring that moves away from the orifice and dissipates into turbulence. During the second half of the cycle the flow in the resonator orifice reverses direction and the formation of the vortex ring occurs inside the tube.

To proceed with theoretical development the following assumptions will be required: (I) the frequency of incident wave is low; under this condition the fluid in the neighbourhood of the orifice may be treated as incompressible, (II) viscous forces are small compared with inertia forces, (III) the formation and the dissipation of the vortex ring occur in the small distance from the orifice, (IV) the flow pattern at the outflow side of the orifice is symmetrical during the cycle.

First we will consider the situation when the acoustic flow is directed from the tube to the resonator cavity (Fig. 1). The assumption, that a fluid motion between cross-sections 1 and 4 behaves as if it were incompressible and nonviscous, yields the following mo-

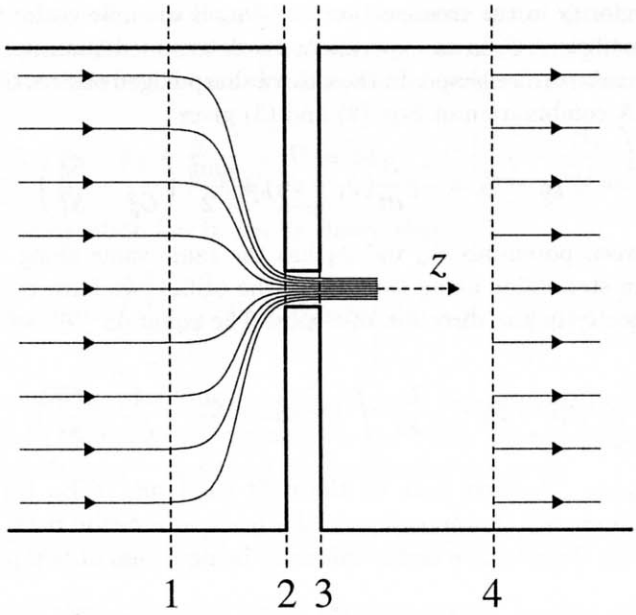

Fig. 1. Streamlines in the neighbourhood of the resonator orifice at high amplitude incident plane wave.

mentum equation

$$\varrho\frac{\partial \mathbf{U}}{\partial t} + \varrho(\mathbf{U}\cdot\nabla)\mathbf{U} + \operatorname{grad}(P) = 0. \tag{1}$$

In the above equation ϱ, $\mathbf{U}$ and P respectively denote the density of fluid, the velocity vector and the total pressure, $P = p + p_0$, where p_0 represents the equilibrium pressure. The velocity $\mathbf{U}$ is a superposition of the acoustic velocity $\mathbf{u}$ and the velocity $\mathbf{v}$ induced by the vortex ring which was formed at the outflow side of the orifice. At the inflow side, in the area between cross-sections 1 and 3, the fluid motion is irrotational ($\mathbf{v} = 0$), then the momentum equation (1) may be reduced to Bernoulli's equation

$$\varrho\frac{\partial \psi}{\partial t} + \frac{\varrho \mathbf{u}^2}{2} + P = \text{const}, \tag{2}$$

which describes the relation between the pressure, the acoustic velocity and the velocity potential ψ along the streamline defined by $\mathbf{u}$. Since the streamlines in the cross-sections 1 and 3 are parallel then the pressures P_1, P_3 and the velocities u_1, u_3 in the planes 1 and 3 are uniform. In this case the mass conservation law gives

$$S_1 u_1 = S_0 u_0\,, \qquad u_3 = u_0/C_c\,, \tag{3}$$

where $S_1 = \pi a^2$ and $S_0 = \pi b^2$ respectively denote the cross-sectional area of the tube and the orifice area, C_c is a contraction coefficient and u_0 is the average velocity in the orifice area

$$u_0(t) = \frac{1}{S_0}\int_0^{2\pi}\int_0^{b} \mathbf{u}_2\cdot\mathbf{n}_z r\,dr\,d\phi, \tag{4}$$

where $\mathbf{u}_2$ is the velocity in the cross-section 2 and $\mathbf{n}_z$ is the unit vector in a direction of the z axis. The coefficient C_c is an experimentally determined quantity, and it is known to be quite sensitive to orifice shape. In the case of sharp-edged orifices C_c approximately equals 0.61 [10]. A combination of Eqs. (2) and (3) gives

$$p_1 + p_0 - P_3 = -\varrho \frac{\partial}{\partial t}(\psi_1 - \psi_3) + \frac{\varrho u_0^2}{2}\left(\frac{1}{C_c^2} - \frac{S_0^2}{S_1^2}\right). \tag{5}$$

A difference between potentials ψ_1 and ψ_3 has the same value along each streamline. If we consider the streamline along the axis of the orifice, we have $\psi = \int u_z dz$, where $u_z(z,t)$ is the velocity in the direction of z axis. The equation (5) can thus be written in the form

$$p_1 + p_0 - P_3 = \varrho \frac{\partial u_0}{\partial t} \int_1^3 F(z)\, dz + \frac{\varrho u_0^2}{2}\left(\frac{1}{C_c^2} - \frac{S_0^2}{S_1^2}\right), \tag{6}$$

where $F(z) = u_z/u_0$. The first term on the right-hand side of Eq. (6) is the pressure drop caused by an energy concentration in the reactive acoustic field. The integral in this term represents the effective orifice thickness being a sum of two parts

$$\int_1^3 F(z)\, dz = w_c d + \int_1^2 F(z)\, dz = w_c d + \Delta d_o\,, \tag{7}$$

where w_c is the correction factor of orifice thickness d, $1 < w_c < 1/C_c$, and Δd_o is the outside end correction which results from the convergence of streamlines on the external side of the resonator orifice. It is reasonably to expect that Δd_o is very close to the end correction at a small amplitude incident wave (linear case). Thus, the analytical determination of this quantity requires a more detailed analysis of acoustic field in the vicinity of the orifice.

Inside the resonator cavity, in the volume V bounded by the cross-sections 3 and 4 (Fig. 1), the fluid motion is rotational due to the formation of vortex ring. The total velocity $\mathbf{U}$ is thus a sum of the acoustic velocity $\mathbf{u}$ and the velocity $\mathbf{v}$ induced by the vortex. In the plane 3 the velocity satisfies the condition of continuity $u_3 = U_3$, while the pressure is uniformly distributed because outside the orifice, on the rigid wall, the pressure is approximately the same as in the jet [11]. In the plane 4, where the velocity $\mathbf{v}$ vanishes, the acoustic velocity is uniform and has the value $u_4 = u_0 S_0/S_1$. Since in the volume V the condition $\mathrm{div}\mathbf{U} = 0$ is satisfied then taking into account the identity [12]

$$\int_V [(\mathbf{a}\cdot\nabla)\mathbf{b} + \mathbf{b}(\mathrm{div}\,\mathbf{a})]dv = \oint_S \mathbf{b}(\mathbf{a}\cdot\mathbf{n}_s)ds, \tag{8}$$

which is true for any vectors $\mathbf{a}$ and $\mathbf{b}$, it is possible to perform the momentum equation (1) into the following integral form

$$\varrho \int_V \frac{\partial \mathbf{U}}{\partial t} dv + \oint_S [\varrho \mathbf{U}(\mathbf{U}\cdot\mathbf{n}_s) + P\mathbf{n}_s]\, ds = 0, \tag{9}$$

where S is a boundary of the volume V and $\mathbf{n}_s$ is a unit vector directed away from the surface S. Because a normal component of velocity vanishes on rigid walls ($\mathbf{U}\cdot\mathbf{n}_s = 0$) and a pressure distribution in the volume V is axially symmetrical then from Eq. (9) one can obtain

$$P_3 - p_4 - p_0 = \frac{\varrho}{S_1}\frac{\partial}{\partial t}\int_V (\mathbf{U}\cdot\mathbf{n}_z)dv + \varrho u_0^2\left(\frac{S_0^2}{S_1^2} - \frac{S_0}{S_1 C_c}\right). \tag{10}$$

Using the mass conservation law it can be shown that

$$\int_V (\mathbf{U}\cdot\mathbf{n}_z)dv = \int_3^4 \left[\int_0^{2\pi}\int_0^a (\mathbf{U}\cdot\mathbf{n}_z) r dr d\phi\right] dz = S_0 u_0 \int_3^4 dz = S_0 u_0 \Delta l\,, \tag{11}$$

where Δl is a distance between cross-sections 3 and 4. Substituting Eq. (11) into Eq. (10) and using Eq. (6) to eliminate the pressure P_3 yields the following equation that determines the pressure drop $p_1 - p_4$ during the first half of the cycle

$$p_1 - p_4 = \varrho\frac{\partial u_0}{\partial t}(w_c d + \Delta d_o + S_0\Delta l/S_1) + \frac{\varrho u_0^2}{2}\left(\frac{1}{C_c} - \frac{S_0}{S_1}\right)^2. \tag{12}$$

Taking into account the assumption (IV) it becomes easy to proceed with the theoretical analysis during the second half of the cycle, when the flow is directed from the resonator cavity to the tube. Because of a different shape of acoustic near field on both sides of the orifice, the considerations analogous as made above give the following equation

$$p_1 - p_4 = \varrho\frac{\partial u_0}{\partial t}(w_c d + \Delta d_i + S_0\Delta l/S_1) - \frac{\varrho u_0^2}{2}\left(\frac{1}{C_c} - \frac{S_0}{S_1}\right)^2, \tag{13}$$

where Δd_i is the inside end correction. The opposite sign in front of the term proportional to u_0^2 is a main difference between Eqs. (12) and (13) because the outside and inside end corrections, as will be shown in Sec. 3, considerably differ only at very small ratios l/a, where l and a are the resonator length and the cavity radius. These end corrections are, however, nearly equal for a typical resonator geometry, in which l/a is usually not too small ($l/a \geq 1/2$). In this case Eqs. (12) and (13) may be written as one equation

$$p_1 - p_4 = \varrho\frac{\partial u_0}{\partial t}(d + \Delta d_n) \pm \frac{\varrho u_0^2}{2}\left(\frac{1}{C_c} - \frac{S_0}{S_1}\right)^2, \tag{14}$$

that applies throughout the duration of the whole cycle. In the above equation Δd_n, on the analogy of linear case, denotes the total end correction at high amplitude

$$\Delta d_n = (w_c - 1)d + \frac{1}{2}\Delta d + S_0\Delta l/S_1\,, \tag{15}$$

where $\Delta d = \Delta d_i + \Delta d_o$ is the total end correction at small amplitude incident sound. In Eq. (14) the pressure drop defined by the first term on the right-hand side is associated with an acoustic reactance. It is a part of the total reactance of resonator because it only describes a mass inertia in the orifice and the near acoustic field. The second term on the right-hand side, which not appears in the linear case, is a resistive term associated

with losses due to the conversion of acoustic energy into vortical energy. Since this term is proportional to the square of mean orifice velocity, it represents a nonlinear part of acoustic pressure.

It follows from Eq. (14), that in a range of high amplitude of the orifice velocity the resistive term is much larger than the reactive one. Now, if one suppose that the pressure drop $\Delta p = p_1 - p_4$ is a harmonic function of the time, $\Delta p \sim \cos(\omega t)$, then from Eq. (14) one can conclude that

$$u_0(t) \approx \pm U_0 |\cos(\omega t)|^{1/2}, \tag{16}$$

where U_0 denotes the peak value of orifice velocity and the plus sign holds when $\cos(\omega t) \geq 0$, while the minus sign when $\cos(\omega t) < 0$. The expression for u_0 may be expand in a Fourier series and according to INGARD [13]

$$\begin{aligned} u_0(t) &= U_0 \sqrt{\pi/2} \sum_{n=0}^{\infty} [\Gamma(7/4+n)\Gamma(3/4-n)]^{-1} \cos[(2n+1)\omega t] \\ &= U_0[1.11\cos(\omega t) - 0.159\cos(3\omega t) + 0.072\cos(5\omega t) - 0.043\cos(7\omega t) + ...], \end{aligned} \tag{17}$$

where Γ is the Gamma function. Thus, due to the nonlinearity the orifice velocity will be distorted so that its frequency spectrum will contain harmonic components.

3. Impedance of resonator

The losses resulting from the absorption of acoustic energy by vortical field may be included into a impedance model of the resonator by insertion of an additional orifice resistance. Since in Eq. (17) the first term in the Fourier series is much larger than the next ones, then it is possible to define this resistance in terms of a fundamental component of the orifice velocity

$$v_0(t) = 1.11\, U_0 \cos(\omega t) = V_0 \cos(\omega t). \tag{18}$$

Thus, using the approximation $u_0 \approx v_0$ in the reactive term of Eq. (14) and Eq. (16) in the resistive term yields the following expression for the pressure drop

$$p_1 - p_4 = \varrho \frac{\partial v_0}{\partial t}(d + \Delta d_n) + \pi b^2 R_n v_0\,, \tag{19}$$

where R_n is a loss resistance in the case of nonlinearity

$$R_n = \frac{\varrho V_0}{2.46\,\pi b^2}\left(\frac{1}{C_c} - \frac{S_0}{S_1}\right)^2. \tag{20}$$

Losses of acoustic energy at high sound intensity are then proportional to the amplitude of fundamental component of the orifice velocity. Since in this case there is a square-law relation between the pressure and the velocity amplitude, R_n is so-called the nonlinear orifice resistance (at the low intensity of incident sound the relation between the pressure and the velocity amplitude is linear). It is important to note that due to the form of

Eq. (19) it is now possible to replace the orifice velocity v_0 by its Fourier representation $\hat{v}_0 = V_0 e^{-j\omega t}$. Thus, the equation equivalent to Eq. (19) is following

$$\frac{\hat{p}_1 - \hat{p}_4}{\pi b^2 \hat{v}_0} = R_n - jk\frac{\varrho c}{\pi b^2}(d + \Delta d_n), \tag{21}$$

where $\hat{p}_1$ and $\hat{p}_4$ denote complex pressures. In order to find a dependence between the orifice velocity and the incident sound pressure it is necessary to determine the pressures $\hat{p}_1$ and $\hat{p}_4$. In the cross-section 1 a pressure distribution is uniform because the streamlines are parallel (Fig. 1). Thus, $\hat{p}_1$ is the pressure in a acoustic far field being a superposition of plane incident and reflected waves, including the plane wave radiated by resonator.

The pressure $\hat{p}_t$ inside the tube in the far field area can be determined by use of a classic theory of sound radiation. According to this theory, the response of resonator under external excitation may be analyzed as a sound production by a vibrating rigid piston located in the resonator orifice [14]. If the origin of a cylindrical coordinate system (r, ϕ, z) lies at the center of the orifice, and in addition the plane $z = 0$ covers the left-hand side of it, then for incident pressure $\hat{p}_i = \widehat{P}_i e^{j(kz-\omega t)}$ a formula describing $\hat{p}_t$ can be written as

$$\hat{p}_t(z,t) = 2\widehat{P}_i \cos(kz) e^{-j\omega t} - \varrho \frac{\partial}{\partial t} \int_0^{2\pi} \int_0^{b} \hat{v}_0(t)\, g_t(z_0 = 0)\, r_0\, dr_0\, d\phi_0\,, \tag{22}$$

where $g_t(z, z_0)$ represents Green's function for the plane wave motion inside the tube and (r_0, ϕ_0, z_0) is a position of source point. The first term on the right-hand side of Eq. (22) is a sum of incident and reflected waves. The quantity g_t can be simply obtained from the expression for the general Green's function G_t which includes both acoustic far and near field components. The function G_t is a solution of the wave equation and satisfies the boundary conditions

$$\frac{\partial G_t}{\partial r}(r = a) = \frac{\partial G_t}{\partial z_0}(z_0 = 0) = 0, \tag{23}$$

then for waves starting inside the tube from $z = -\infty$ is given by [15]

$$G_t = \sum_{m=0}^{\infty} \sum_{n=0}^{\infty} g_{mn} \cos(k_{mn} z_0) \exp(-jk_{mn} z), \tag{24}$$

where

$$g_{mn} = \frac{j}{\pi a^2}\, \epsilon_m \cos[m(\phi - \phi_0)]\, \frac{J_m(\gamma_{mn} r/a) J_m(\gamma_{mn} r_0/a)}{k_{mn}[1 - (m/\gamma_{mn})^2] J_m^2(\gamma_{mn})} \tag{25}$$

and γ_{mn} is the nth root of the equation $dJ_m(\gamma)/d\gamma = 0$, $k_{mn} = [k^2 - (\gamma_{mn}/a)^2]^{1/2}$, and ϵ_m is the Neumann factor, $\epsilon_0 = 1$, $\epsilon_m = 2$ $(m > 0)$. As may be seen, the function g_t is determined by the first term in the series on the right-hand side of Eq. (24) which is independent on r and r_0. Following from this, one can write Eq. (22) as

$$\hat{p}_t(z,t) = 2\widehat{P}_i \cos(kz) e^{-j\omega t} - \varrho c\, (b/a)^2 V_0 e^{-j(kz+\omega t)}, \tag{26}$$

where the second term on the right-hand side represents the plane wave radiated by resonator. Since it was assumed that a frequency of the incident wave is small, then a

distance between the cross-section 1 and the orifice plane is much less than the wavelength. Under this condition from Eq. (26) one can easily obtain an expression for the unknown pressure $\hat{p}_1$

$$\hat{p}_1(t) = \hat{p}_t(z,t)_{|kz\to 0} = \left[2\widehat{P}_i - \varrho c\,(b/a)^2 V_0\right] e^{-j\omega t}. \tag{27}$$

The same method, as presented above, will be used for a determination of the pressure $\hat{p}_4$. In order to simplify the analysis we move the origin of a coordinate system to a plane which covers the right-hand side of the orifice (Fig. 1). In a small distance from the orifice plane a pressure in the resonator cavity is uniform, because it represents a superposition of multiple plane wave reflections. The formula for this pressure is thus given by

$$\hat{p}_c(z,t) = \varrho \frac{\partial}{\partial t} \int_0^{2\pi} \int_0^{b} \hat{v}_0(t)\, g_c(z_0 = 0)\, r_0 dr_0 d\phi_0\,, \tag{28}$$

where $g_c(z, z_0)$ is the Green's function for the plane wave motion inside the resonator cavity. It is a part of a general Green's function G_c derived for the resonator interior. Since G_c must satisfy boundary conditions

$$\frac{\partial G_c}{\partial r}(r = a) = \frac{\partial G_c}{\partial z_0}(z_0 = 0) = \frac{\partial G_c}{\partial z}(z = l) = 0, \tag{29}$$

then it may be expressed as follow

$$G_c = j \sum_{m=0}^{\infty} \sum_{n=0}^{\infty} g_{mn} \cos(k_{mn} z_0) \left[\sin(k_{mn} z) + \cos(k_{mn} z) \cot(k_{mn} l)\right]. \tag{30}$$

Since the function g_c is determined by the first term of this series then taking into account Eq. (28) one can write the expression for the pressure $\hat{p}_4$ as

$$\hat{p}_4(t) = \hat{p}_c(z,t)_{|kz\to 0} = j\varrho c\,(b/a)^2 V_0 \cot(kl) e^{-j\omega t}. \tag{31}$$

Finally, substituting Eqs. (26) and (31) into Eq. (21) yields the following formula for the acoustic impedance of resonator

$$Z = \frac{2\widehat{P}_i}{\pi b^2 V_0} = R_r + R_n + jX, \tag{32}$$

where $R_r = \varrho c/(\pi a^2)$ is the radiation resistance and X is the reactance of resonator

$$X = \frac{\varrho c}{\pi a^2} \cot(kl) - k \frac{\varrho c}{\pi b^2}(d + \Delta d_n). \tag{33}$$

The end correction $\Delta d = \Delta d_o + \Delta d_i$ which appears in a definition of Δd_n [Eq. (15)] represents the added mass effect at small amplitudes of incident sound. Thus, the quantity Δd may be determined by calculating the co-vibrating masses m_o and m_i on both sides of the resonator orifice. They are simply a product of air density and a result of double

surface integration of these parts of Green's functions G_t and G_c which depend on radial coordinates

$$\begin{aligned} m_o &= \varrho\pi b^2 \Delta d_o = \varrho \int_{S_0}\int_{S_0} (G_t - g_t)_{|z,z_0=0}\, r_0 r\, dr_0 dr\, d\phi_0 d\phi, \\ m_i &= \varrho\pi b^2 \Delta d_i = \varrho \int_{S_0}\int_{S_0} (G_c - g_c)_{|z,z_0=0}\, r_0 r\, dr_0 dr\, d\phi_0 d\phi. \end{aligned} \tag{34}$$

After integration one can obtain expressions for outside and inside end corrections

$$\Delta d_o = \sum_{n=1}^{\infty} \frac{4aJ_1^2(\gamma_{0n}b/a)}{\gamma_{0n}^3 J_0^2(\gamma_{0n})}, \qquad \Delta d_i = \sum_{n=1}^{\infty} \frac{4aJ_1^2(\gamma_{0n}b/a)}{\gamma_{0n}^3 J_0^2(\gamma_{0n})} \coth\left(\frac{\gamma_{0n}l}{a}\right). \tag{35}$$

In the work of INGARD [1] it was assumed that for the cylindrical resonator placed at the end of a tube the outside end correction equals the inside one. The formula obtained for outside end correction agrees with Ingard's result. However, the exact expression for inside end correction derived in this paper indicates that Δd_o and Δd_i differ and it results from the additional factor $\coth(\gamma_{0n}l/a)$ in each term of the series. Since the quantity γ_{0n} is the nth root of the equation $dJ_0(\gamma)/d\gamma = 0$, then one has: $\gamma_{01} = 3.83$, $\gamma_{02} = 7.02$, $\gamma_{03} = 10.17$ ... . Thus, a difference between Δd_o and Δd_i is large at very small values of l/a, but Ingard's approximation $\Delta d_o \approx \Delta d_i$ is valid for $l/a \geq 1/2$.

4. Absorption coefficient of resonator

Inside the tube a long distance from the orifice plane an acoustic field is determined by a sum of two plane waves which propagate in positive and negative z direction. The first one represents an incident wave, while the second is a superposition of reflected and radiated waves. To proceed with theoretical analysis it is now necessary to introduce a complex reflection coefficient $\hat{\beta}$ which is defined as the ratio between pressure amplitude of the wave travelling in negative z direction to that of the incident wave. Thus, Eq. (26) for the pressure in the far field one can rewrite in the form

$$\hat{p}_t(z,t) = \widehat{P}_t e^{-j\omega t} = \widehat{P}_i \left(e^{jkz} + \hat{\beta} e^{-jkz}\right) e^{-j\omega t}. \tag{36}$$

From Eqs. (26) and (32) one can obtain the expression for the reflection coefficient

$$\hat{\beta} = \beta e^{j\chi} = 1 - 2Ae^{-j\varphi}, \tag{37}$$

where β denotes a modulus of the reflection coefficient and

$$A = \frac{R_r}{\sqrt{(R_r + R_n)^2 + X^2}}, \qquad \varphi = \arctan\left(\frac{X}{R_r + R_n}\right), \qquad -\frac{\pi}{2} \leq \varphi \leq \frac{\pi}{2}. \tag{38}$$

Equation (36) may now be used to express the modulus of a pressure in far field area in terms of coefficient $\hat{\beta}$

$$|\widehat{P}_t| = |\widehat{P}_i| \sqrt{1 + \beta^2 + 2\beta\cos(2kz - \chi)}. \tag{39}$$

From Eqs. (39) the modulus of $\hat{\beta}$ can be obtained

$$\beta = \frac{|\widehat{P}_t|_{\max} - |\widehat{P}_t|_{\min}}{|\widehat{P}_t|_{\max} + |\widehat{P}_t|_{\min}} = \sqrt{1 + 4A^2 - 4A\cos(\varphi)} \tag{40}$$

and from this, the expression for the energy absorption coefficient

$$\alpha = 1 - \beta^2 = 4A[\cos(\varphi) - A]. \tag{41}$$

At low pressure amplitudes the nonlinear component of resistance can be neglected ($R_n = 0$). In this case the expression (38) for the quantity A yields

$$A = \frac{1}{\sqrt{1 + \tan^2(\varphi)}} = \cos(\varphi), \tag{42}$$

and this means, according to Eq. (41), that the absorption coefficient α always equals zero. This result is in full agreement with the basis of linear acoustics for nonviscous fluids. Thus, the conclusion may be derived that at high amplitude the changes in the absorption coefficient at the resonant frequency result from an increase of the resistance R_n. In accordance with the foregoing theory the absorption coefficient in the case of resonance ($X = 0$),

$$\alpha = 4A(1 - A) = \frac{4R_n/R_r}{(1 + R_n/R_r)^2} \tag{43}$$

increases with the growth of the nonlinear resistance R_n as long as $R_n < R_r$. When the equality $R_n = R_r$ is reached the absorption coefficient equals unity. It follows from Eq. (43) that further increase in the resistance R_n makes a contribution to decrease in the coefficient α.

A value of α cannot be computed directly from Eq. (41) because the parameter A and phase φ are dependent of the velocity amplitude V_0 which is a solution of the equation

$$2|\widehat{P}_i| - \pi b^2 V_0 |R_r + R_n + jX| = 0. \tag{44}$$

In order to solve Eq. (44) it is necessary to apply a numerical procedure because nonlinear resistance R_n depends on the orifice velocity [see Eq. (20)]. A simple analytic solution may be obtained only in the case of resonance and the result is

$$\frac{R_n}{R_r} = \frac{1}{2}\sqrt{1 + \frac{3.26}{\varrho c^2}\left(\frac{S_1}{S_0 C_c} - 1\right)^2 |\widehat{P}_i|} - \frac{1}{2}. \tag{45}$$

Equation (43) together with this solution enables to determine a dependence of the absorption coefficient α at a resonant frequency on the incident pressure amplitude $|\widehat{P}_i|$. As may be noted, there is such a value of $|\widehat{P}_i|$ for which the absorption coefficient equals unity. This amplitude may be calculated directly from Eq. (45) putting R_n equal R_r. The result is

$$|\widehat{P}_i| = \frac{2.46\varrho c^2 (b/a)^4}{[1/C_c - (b/a)^2]^2}, \tag{46}$$

so, the pressure amplitude, at which the absorption coefficient is equal to unity, depends on the ratio b/a only. Since this dependence would be useful in the practical resonator

design it is reasonably to replace the pressure amplitude $|\widehat{P}_i|$ by its level L_i expressed in decibels. In Fig. 2, the level L_i calculated from Eq. (46) is plotted against the ratio b/a in the range $0.02 \leq b/a \leq 0.5$. One immediately sees that at very small values of b/a the maximum sound absorption occurs for relatively low pressure levels of incident wave ($L_i \approx 60\,\mathrm{dB}$). With growing b/a the level L_i fast increases, reaching the value $L_i \approx 175\,\mathrm{dB}$ for the ratio $b/a = 0.5$.

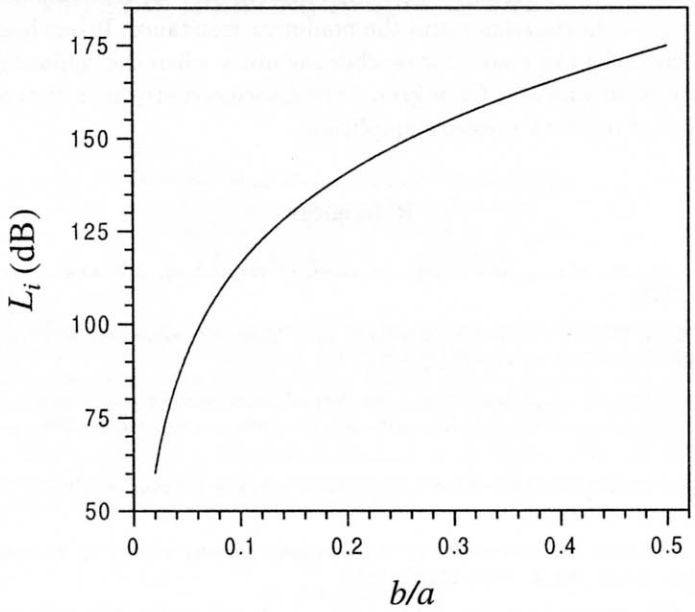

Fig. 2. Dependence of pressure level L_i on ratio b/a.

5. Discussion and conclusions

The acoustic nonlinearity phenomenon, which occurs when the Helmholtz resonator is excited by high amplitude sound wave, has been investigated in this paper. A theoretical model has been presented in order to explain an increase in acoustic energy losses with increasing sound intensity. It has been shown that the nonlinear loss mechanism is associated with a flow separation on the orifice edge and a formation of high speed jet on the outflow side of the orifice, because the interaction of jet with motionless medium results in a generation of the vortical field which extracts energy from acoustic field.

In the theoretical study a pressure field was determined separately in the area with irrotational and rotational fluid motion. It is important to emphasize that this theory may also be applied in the case of high amplitude acoustic transmission through an orifice plate in a pipe. As compared to the model of CUMMINGS [8], in which the rotational fluid motion was totally ignored, the present study gives a more complete description of the pressure field in the orifice surroundings.

It was found that a total pressure drop due to the jet formation and generation of vorticity is proportional to the square of the orifice velocity amplitude. This dependence for sinusoidal excitation signals leads to a harmonic distortion of the orifice velocity. As a result of this distortion the complications arise in definition of the resonator impedance. In the present study this problem was overcome by determining this impedance for the fundamental component of orifice velocity. If in the impedance model an acoustic energy loss due to a viscosity is neglected, then the resistive part of the resonator impedance consists of the radiation resistance and the nonlinear resistance. It has been shown that the absorption coefficient of resonator reaches the unity when the radiation resistance is equal to the nonlinear one and for a given resonator geometry it occurs at the exactly determined value of incident pressure amplitude.

References

[1] U. INGARD, *On the theory and design of acoustic resonators*, J. Acoust. Soc. Amer., **25**, 6, 1037–1061 (1953).

[2] D.A. BIES, O.B. WILSON, *Acoustic impedance of a Helmholtz resonator at very high amplitude*, J. Acoust. Soc. Amer., **29**, 6, 711–714 (1957).

[3] S. CZARNECKI, *Utilization of non-linear properties of resonators for improving acoustic conditions in rooms*, Proceedings of the 6th International Congress on Acoustics, Tokyo, Japan, 197–200 (1968).

[4] S. CZARNECKI, *Non-linear absorption properties of acoustic resonance systems* [in Polish], Arch. Akustyki, **1**, 4, 37–49 (1969).

[5] J. WU, I. RUDNICK, *Measurements of the nonlinear tuning curves of Helmholtz resonators*, J. Acoust. Soc. Amer., **80**, 5, 1419–1422 (1986).

[6] B.T. ZINN, *A theoretical study of non-linear damping by Helmholtz resonators*, J. Sound Vib., **13**, 3, 347–356 (1970).

[7] A. CUMMINGS, W. EVERSMAN, *High amplitude acoustic transmission through duct terminations: theory*, J. Sound Vib., **91**, 4, 503–518 (1983).

[8] A. CUMMINGS, *Transient and multiple frequency sound transmission through perforated plates at high amplitude*, J. Acoust. Soc. Amer., **79**, 4, 942–951 (1986).

[9] M. MEISSNER, *The influence of acoustic nonlinearity on absorption properties of Helmholtz resonators, part II: experiment* (in preparation).

[10] G. BATCHELOR, *An introduction to fluid dynamics*, Cambridge University Press 1967, pp. 388, 497.

[11] P. MORSE, K. INGARD, *Theoretical acoustics*, McGraw–Hill, New York 1968, p. 759.

[12] B. ŚREDNIAWA, *Hydrodynamics and theory of elasticity* [in Polish], PWN, Warszawa 1977, p. 407.

[13] U. INGARD, *Nonlinear distortion of sound transmitted through an orifice*, J. Acoust. Soc. Amer., **48**, 1, 32–33 (1970).

[14] L.E. KINSLER, A.R. FREY, *Fundamentals of acoustics*, John Wiley & Sons, New York 1962, p. 177.

[15] P.M. MORSE, H. FESHBACH, *Methods of theoretical physics*, McGraw–Hill, New York 1953, p. 1515.

ARCHIVES OF ACOUSTICS
24, 2, 191–206 (1999)

FROM EAR MODELING TO AUDITORY TRANSFORM

P. KLECZKOWSKI

Department of Mechanics and Vibroacoustics
Academy of Mining and Metallurgy
(30-059 Kraków, Al. Mickiewicza 30, Poland)
e-mail: kleczkow@uci.agh.edu.pl

Understanding how the auditory system works recently gains increasing importance in audio engineering. Its most widespread practical use is in perceptual audio coders, with even more applications to be foreseen in the future. The construction of a mathematical procedure that could transform acoustic signals heard by humans to data corresponding to auditory sensation would open way to significant progress in audio engineering. In this paper the issue is discussed and important research in the field is reviewed. The proposal for a frequency analysis procedure appropriate for ear modeling is presented and verified. This procedure is a form of the Wavelet Transform.

1. Introduction

Understanding how the ear works has been a challenge to researchers since Ohm formulated his "acoustic law" in 1843. This knowledge, apart from purely medical, has practical applications in such fields as construction of devices for people with handicapped ear, audio engineering [37] or noise control [11]. A new area of technology where ear modeling is directly applied is the construction of low bit rate coders of digital audio signals, usually referenced as perceptual coders.

Another, future-oriented application is the construction of an appropriate set of data (data vector) to be used as an input to artificial neural networks.

The foundations for modern knowledge on this subject have been laid by von Bekesy in 1947, with his pioneering work identifying vibration at the basilar membrane as travelling waves. The efforts are continued, but functioning of higher (neural) stages of the ear are still subjects of partial hypothesis, of which not one has been widely accepted without questioning.

2. The auditory system as an acoustic receiver

Our ear perceives time functions of acoustic pressure as continuous evolution, or sequences, of separate acoustic events, characterized by their pitches and timbres. It

is able to perceive and comprehend speech of one speaker with many other voices in the background, or to follow the melodic line of one instrument out of an ensemble. The auditory system transforms a time function of acoustic pressure into separate streams of information. Most of these complex functions are performed in higher stages of the auditory system and little is known about them, but whatever the nature of this information-processing mechanism is, it must rely on information received from the peripheral stages of the auditory system. Therefore, any attempt to investigate these processes must be based on a solid model of information supplied by the peripheral auditory system to higher auditory stages.

The time function received by the ear is a linear superposition of acoustic pressures from separate individual sources, while the separate streams of information isolated by the ear build auditory sensations corresponding to sounds produced by each of the sources individually. Although the number of those individual sources that can be simultaneously perceived by the ear is limited, the entire mechanism is so sophisticated that no successful attempt has been made so far to implement it artificially.

3. General review of operations performed by the auditory system

In this paper the acoustical, the mechanical and a fragment of the neural path are considered. The last physiological (neural) element in this chain that is covered is cochlear nucleus, so little more than the peripheral auditory system and only monaural hearing will be discussed.

The outer ear plays roles of mechanical protection, microclimate control and directivity detection aid. Physically, it is a pipe with a length of about 2 cm open at one end thus enhancing waves of four time its length, i.e. frequencies around 4 kHz. The middle ear, i.e. three ossicles: malleus, incus and stapes act as an impedance transformer, which maximizes the energy transmitted into the inner ear, and eliminates reflections of waves at the boundary of gas and liquid mediums. The cochlea (part of the inner ear) is filled with a liquid (perilymph and endolymph), and because of complexity of mechanics of the cochlea, the input impedance of the inner ear changes with vibration level and frequency. At the oval window — the place where the stapes touches the cochlea and which is a boundary between the middle and inner ears, the vibration of the stapes can still be considered a time function, related to the acoustic pressure outside of the ear.

Inside the cochlea complex, but relatively well understood processes take place, which can be functionally (but hardly physiologically) separated into two sub-processes. The first is nonlinear mechanical filtering, the second is a transduction from mechanical movement of the basilar membrane to electrochemical activity of neurones.

The basilar membrane with perylimph surrounding it was long considered to be a passive mechanical filter. Vibration at the oval window is the source of waves travelling along the membrane up to the point of maximum amplitude, and then decaying rapidly. The basilar membrane can be considered as a bank of bandpass filters. As all filters have steep upper slope and mild lower slope simpler models often simulate it as a chain of low-pass filters. The estimation of the resolution of this mechanical filter has changed

substantially. Earlier experiments indicated that the Q factor of a typical basilar membrane — based bandpass filter was on the order of 1, that is far lower than the overall Q value of the entire auditory system estimated at 100 (or even 200 by some researchers [39]). Over the past 25 years more sophisticated measurement methods were developed and evidences became available that the true value of Q of the membrane is much higher [28]. No passive mechanical model can explain such a high selectivity.

It is now agreed by most researchers that there is some active process in the cochlea, supplying energy to the basilar membrane in a positive feedback which provides this high frequency selectivity, and that outer hair cells in the organ of Corti, a small organ distributed along the basilar membrane, play a key role in this process.

The other sub-process performed in the cochlea is a transduction of vibration at specific place along the basilar membrane to the appropriate neural signal [34, 39]. This process is performed inside the organ of Corti, and transducers are inner hair cells. The vibration sensed is, in terms of signal processing, rectified, and then converted to series of neural spikes further transmitted along the auditory nerve (composed of around 30000 neural axons) to higher stages of the auditory system. The rectification mentioned is only approximate and has physiological origin: the processes resulting in the excitation of hair cells are in the most part those accompanying the deflection of the basilar membrane in one direction.

There is a long lasting controversy among researchers of the hearing system. One point of view attributes most meaning to the analysis of places of excitation on the basilar membrane ("place theories") while the other emphasizes the role of information contained in the time structure of a signal from a particular area on the basilar membrane ("time theories").

Nonlinearities in the operation of the cochlea have three sources. One is mechanical nonlinearity of the basilar membrane. The second is inherent nonlinearity of the electrochemical processes in mechanical to neural transduction. This latter nonlinearity is of the "hard limiting" type and is seriously limiting the dynamic range of any single hair cell. However, the entire transduction mechanism compensates for this, by way of combining many haircells with different thresholds of activation [28].

The third source of nonlinearity is the positive feedback in the cochlea mentioned above, and is least known.

Experiments aimed at estimation of the Q value at different stages of the neural path of the auditory system have shown that the shape of tuning of neural responses along the higher stages of the auditory system is similar to the response at the auditory nerve leaving the cochlea and is not very sharp. The origin of the ear's high Q factor is still not quite clear [28].

One feature, commonly agreed upon is that the representation of neural activity leaving the cochlea is tonotopic throughout the rest of the auditory system, that is spatial distribution of neural cells conveying information from particular fragments of the basilar membrane is preserved along the subsequent stages of the auditory system. There is evidence that this tonotopic distribution becomes two-dimensional in the auditory cortex [41]. The higher stages of auditory processing are fairly well known in their physiological construction, also neural responses in different stages have been intensively studied [28].

However, functional explanation of the entire system is still rather unclear. Apart from higher functions mentioned in Sec. 2. the seemingly simpler mechanism of a very high frequency selectivity of the ear has not yet been understood.

One more physiological stage of neural processing within the scope of this article is the cochlear nucleus. There are evidences that the process called lateral inhibition takes place there. When largely simplified and in the context of spectral analysis performed by the ear, it can be described as enhancing stronger spectral components while suppressing neighbouring weaker components. However, it is not clear whether this mechanism contributes to the sharpening of ear's overall frequency selectivity.

4. Different approaches to modeling the auditory system

This task is enormously complex for two main reasons:

a) The elements of the auditory system are highly nonlinear and difficult to separate into independent blocks performing specific functions. Modeling its higher stages is yet more difficult because their operation is hardly known.

b) When modeling the entire auditory system we have to deal with the output signals which are very difficult to measure since we neither have a measuring device nor a unit of measure. If such a unit existed, it would have to be multidimensional. Some works addressed the problem of multidimensional timbral space, trying to locate sounds of musical instruments there [33]. It is difficult to express subjective percepts in our brain in a quantitative way. Auditory percepts are the domain of psychoacoustics and some quantitative measures of auditory sensations have been developed there, for example the sone scale for measurement of sensation of loudness. Although psychoacoustics can help us to measure the sensations of loudness and pitch, we are still unable to measure more complex, multidimensional percepts such as timbre.

The problem of modeling can be approached by looking at it from two different perspectives.

Psychoacoustical approach. It seems that many of the test stimuli used in psychoacoustical experiments may not engage more complex functions of the higher stages of the auditory system, so that they may not reveal some features of the ear.

Physiological approach. Here an attempt is made to divide the auditory system to some physiologically separate parts and model their functions mathematically. A model encompassing all peripheral stages and higher stages up to the cochlear nucleus, with consequent mathematical formalism can be found in [39]. However, only limited verification of this model is given.

Fairly well verified models of this sort exist, but most of them encompass only limited part of the auditory system, mainly in its peripheral stages.

Some works try to model particular functions of the ear, instead of its physiological parts. Such models differ from the psychoacoustic approach in that in building these models they use knowledge about physiological construction of the system and can be seen as physiologically encompassing the complete system.

The function most often simulated in such models is the sensation of pitch [8, 12, 27, 36]. The sensation of pitch is very suitable for modeling, for the ear is very sensitive to pitch (high overall Q of the system seen as a filterbank) and it is probably the most important percept upon which the ear analyses and qualifies sounds.

5. Techniques of modeling

Probably the largest number of physiologically-based models have been built for the basilar membrane, from linear one-dimensional ones of various complexity [12, 39], non-linear one-dimensional [21], to three-dimensional [3]. In [20, 24] models in the form of chains of building blocks are presented. These implementations are analog and digital respectively, and both include positive feedback activated by outer hair cells.

When modeling the peripheral part of the ear, the different physical quantities (mechanical and electrochemical) can be modeled as continuous or discrete functions of time. Some researchers tend to exploit information theory and shift the problem from the domain of deterministic signals to the domain of stochastic signals, like in [13, 30].

Modeling of higher neural stages requires sophisticated mathematical tools used in pattern recognition, neural network modeling and probably some specific ones not yet developed.

6. Decomposition of functions of the ear into blocks

The following block diagram of the ear may be proposed (Fig. 1), if we try to use blocks to which appropriate signal processing procedures can be attributed This is a framework generalizing the approach taken in some models. Such a generalized model attempts to simulate all salient functions of peripheral stages of the ear, albeit in simplified form.

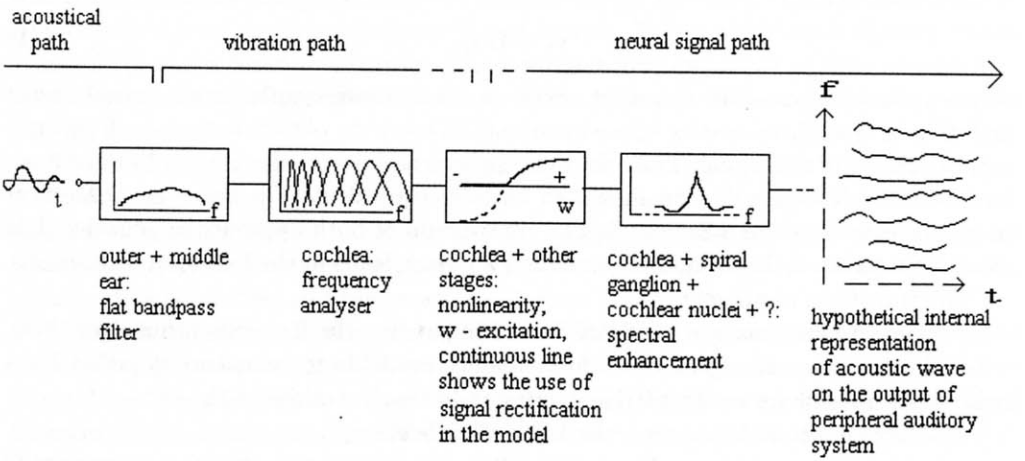

Fig. 1. Simplified functional diagram of extended peripheral auditory system.

A common element of all models of the ear is some sort of frequency analysis (Fig. 1), as this function of the cochlea is unquestionably agreed upon as probably the most fundamental. Many models in fact perform only this one function and still are successful, especially when frequency analysis is combined with a simplified form of the fourth block in Fig. 1 — spectral enhancement.

The nonlinearity, performed in the third block is being simulated by different means, and with very different effect on processing of the signal. However, due to its very complex nature and many places of the auditory system where it can be found, it is rather difficult to simulate its effects [28, 43]. Some models include the automatic gain control as the only nonlinearity, as such mechanism is certainly present in the auditory system. This stage will not be discussed in more detail.

Spectral enhancement (fourth block) is associated with the reduction of data. Such a process takes place in the auditory system. A simplified implementation of this block is achieved by assigning less meaning to parts of the spectrum which are weaker. Less meaning leads to less bits of resolution and the procedure is governed by masking curves supplied by psychoacoustics. This is the way all perceptual coders work.

7. Modeling the frequency analysis function of the ear

Bandpass filters appropriate for modeling the ear should have shorter impulse response for high frequencies than for low ones [17, 19, 31]. Such are the "filters" in the ear. This type of filters is usually referred as "constant Q" type, i.e. the widths of bandpass filters are proportional to their centre frequencies.

For frequency analysis typically either the spectral decomposition by means of an appropriate transform, or a bank of bandpass filters is used. Throughout this paper, the formulas will be given either in continuous or in discrete form, whichever is more convenient.

Usually a sequence of block transforms:

$$\mathbf{y}_k = \mathbf{H}\,\mathbf{x}_k, \tag{1}$$

where $\mathbf{y}_k$ is k-th consecutive output vector, $\mathbf{x}_k$ is k-th consecutive input signal vector and $\mathbf{H}$ is a transform matrix (time-invariant) is used, to obtain a time — frequency representation of the signal. Then the filtering approach is closely related. In their basic forms both techniques can be shown to be fully equivalent [40]. However, differences in implementations are meaningful. The comparison of both approaches, considered as candidates for modeling of auditory spectral analysis, leads to the following conclusions.

The transform approach:

+ compact mathematical form, often resulting in powerful fast computing algorithms,

+ the transformed signal has a form readily available for monitoring, either for a human observer or for an algorithm simulating further functions of the ear,

+ orthogonal transforms obey the Parseval's theorem,

– only wavelet transforms have a very desirable feature of performing a constant Q type of spectral analysis, instead of most common constant bandwidth type,

– distortion may be generated in boundaries of neighbouring signal blocks (blocking effect), which requires means to alleviate or eliminate this problem.

The filtering approach:

+ is more natural in simulation of auditory filters,

+ arbitrary filter shapes can be designed, especially in the case when non-decimated (operating at the sampling frequency of the input signal in all bands) filters are used,

+ has no blocking effects,

– non-decimated filters lead to very redundant spectral representation,

– decimated filters (critically sampled) can only be used when none or very limited processing in spectral domain is to be performed, as those filters guarantee perfect reconstruction only under such a condition,

– if some distortion is present resulting from imperfections of filters, they are very different in nature than those produced by the ear.

7.1. Application of transforms

The Fourier Transform in its original form can only be used for either the analysis of impulses shorter than ear's resolution in time or for stationary signals, and hence is impractical for ear modeling, where we require a representation in which the output vector $\mathbf{y}_k$ changes with time, as in (1). Such a distribution is the Short Time Fourier Transform (STFT — the definition in continuous domains is given as more general) [29]:

$$\mathrm{STFT}\,(\tau,\omega) = \int_{-\infty}^{\infty} s(t)h(t-\tau)e^{-j\omega t}dt, \tag{2}$$

where τ is time around which we analyse the spectrum, ω is radian frequency, $s(t)$ is an input signal, $h(t)$ is time window through which we observe this signal. The shape of the time window determines the parameters of the distribution obtained. It is easy to notice that if we divide the integrand by $e^{-j\omega t}$ then we obtain the convolution of a time signal $s(t)$ with $h(-t)$, i.e. the time window reversed in time. This is where equivalence between a transform and a filter comes from. The Fourier transform $H(\omega)$ of the function $h(t)$ is exactly the shape of the filter equivalent to the evolution with time τ of one point of the transform.

The STFT as a tool for ear modeling has two drawbacks. The first one is that it performs a constant bandwidth analysis. The second results from the Balian–Low theorem [23], which states that if we critically sample the STFT (to avoid redundancy) then either time or frequency support of basis functions of the transform must go to infinity, thus good time and frequency localization is not possible.

More advanced transforms, related to the STFT have been developed and are used in practical implementations of perceptual audio coders. They are easily interpreted as filters. Most popular of them is the Modulated Lapped Transform also known as Modified Discrete Cosine Transform (MDCT) [25, 35]. The more general framework that describes them is called local trigonometric bases [44]. Being orthogonal transforms, in contrast to the STFT they can achieve good localization in both time and frequency. They also

meet a specific compromise between the Q factor of filters, their distortion rate and computational efficiency, and would be very good candidates for ear modelling, but they perform constant bandwidth analysis.

Linear transforms related to the Fourier transform are all limited in their time--frequency resolution by the uncertainty principle. This limit could be relaxed by the use of one of a family of time-frequency distributions which have much better energy concentration in the time-frequency plane (Cohen's class distributions) [7]. The most widely investigated of them is the Wigner–Ville distribution:

$$W(\tau,\omega) = \int_{-\infty}^{\infty} s\left(\tau + \frac{t}{2}\right) s^*\left(\tau - \frac{t}{2}\right) e^{-ej\omega t}, \tag{3}$$

where $s^*(t)$ denotes complex conjugate of the signal. However, as can be seen from the formula this representation is quadratic in $s(t)$ and therefore the distribution is nonlinear. It has the so-called "cross-terms" which make the results quite obscure, despite their excellent time-frequency resolution. It is also, in general case, non-invertible.

The cross-terms can be smoothed to some extent, but at the cost of reducing good joint time-frequency resolution.

Some works have addressed the problem of finding a frequency analysis tool appropriate to analyze sounds of musical instruments. Although not directly referring to the ear, their results are suitable for the problem discussed in this paper. A specific distribution belonging to Cohen's class, related to the Wigner distribution and called modal distribution is given in [32]. This distribution suppresses cross-terms but is inappropriate for transient — like sounds, such as musical sounds with sharp attacks.

There have been many attempts to modify the Fourier or related ransforms in order to make it a constant Q analysis. For the purpose of analysing musical sounds Brown [4] proposed such a modification directly in the digital form, but it was not invertible.

The relatively new transform, the Wavelet Transform (WT), is of the constant Q type, when used for frequency analysis [6, 10, 23, 38, 40]. The continuous WT(CWT) is given by:

$$\mathrm{CWT}(\tau,a) = \frac{1}{\sqrt{a}} \int s(t) h^*\left(\frac{t-\tau}{a}\right) dt, \tag{4}$$

where a is a scale factor (corresponding to frequency), $h(t)$ is a basic wavelet (or mother wavelet). The $h(t)$ can be real (more often used in practice) or complex; in this latter case the complex conjugate $h^*(\cdot)$ is used in (4) and the transform becomes complex. The choices of $h(t)$, and discretization steps for a and τ (together forming a discretisation grid in the time — scale plane) determine the features of the wavelet transform obtained.

The essence of the WT is that for any particular scale a the function $h(\cdot)$ of (4) is dilated or contracted proportionally along the abscissa, thus fulfilling the postulate of constant Q representation.

Generally, there can be four forms of the WT: the continuous WT given by (4); the discrete parameter WT, where parameters a and τ are discretized; the discrete time WT, where parameters and the signal under analysis $s(k)$ is discrete; the discrete WT, where the previous quantities and the $h(a,\tau,k)$ are discrete. A discrete mother wavelet

$h(k)$ can be a sampled version of its continuous time counterpart, but $h(k)$ which do not have a continuous version can be constructed. The latest case, with the basis value of a equal 2, takes the form:

$$\mathrm{DWT}(m,n) = 2^{-m/2} \sum_k s(k) h(2^{-m}k - n), \tag{5}$$

where m, n are integer values of parameters a and τ, k is a number of signal sample. This form is most widely used in practice, because of two important advantages:

a) the scaling forms a simple "dyadic" structure, for which fast algorithms — Fast Wavelet Transform exist;

b) the interpretation as a filterbank is straightforward.

The big disadvantage, when used for modeling of the ear, is that the analysis defined by (5) is an octave band analysis, so its frequency resolution is insufficient.

If $\{h_{m,n}\}$ form an orthonormal basis set, then the inversion formula takes the simple form of the sum of appropriate inner products between transform coefficients and basis functions:

$$s(k) = \sum_m \sum_n 2^{-m/2} h(2^{-m}k - n) \mathrm{DWT}_{m,n}. \tag{6}$$

The mathematics related to the choice of the mother wavelet is fairly complex [10], however, if we can accept large redundancy in our data, which in practice means choosing a relatively dense sampling of the time-scale plane, then we have large area of freedom in this choice.

In the redundant case the basis vectors of the tranformation will not be orthogonal, the only requirement is that they must span the vector space. The set of basis vectors is then called a frame. A condition for a set to be a frame is that for any $m \times 1$ vector $\mathbf{s}$ [6, 10, 23, 38]:

$$A\|\mathbf{s}\|^2 \leq \sum_{i=1}^{n} |\langle \mathbf{s}, \mathbf{h}_i \rangle|^2 \leq B\|\mathbf{s}\|^2, \qquad n \geq m, \tag{7}$$

where A and B are positive constants ("frame bounds"), $\mathbf{s}$ is input signal vector, $\langle \mathbf{s}, \mathbf{h} \rangle$ is the inner product of vectors. According to (7), the energy of the (discrete) wavelet coefficients relative to that of the signal must be within the two bounds.

The reconstruction from a frame is more difficult, as instead of the set $\{h_i\}$ another set, called dual set $\{\hat{h}_i\}$ is used [10], and its computation from $\{h_i\}$ is not easy. When in (7) $A = B$, then the frame is called tight frame and $\{\hat{h}_i\} = \{h_i\}$ holds.

When the ratio of B/A is close to 1, then a frame is an approximation to the tight frame, and signals can be approximately reconstructed with the use of an original basis set $\{h_i\}$. It depends on the application and the particular mother wavelet, how close to 1 the B/A ratio should be.

Working with the discrete parameter WT, we can obtain frames arbitrarily close to tight frames, by dense sampling of the CWT in both time and scale, i.e. the a and τ parameters. For a given mother wavelet there are threshold values (a_0, τ_0), below which the $\{h_{m,n}\}$ will always form a frame [6].

The fact that it is possible, albeit not easy, to use bases which are not orthogonal and thus to have large flexibility in the choice of a mother wavelet is crucial in the task of ear

modeling: it allows to construct $h(t)$ which simulates the impulse response of auditory filters.

IRINO and KAWAHARA [18] used a simulated response of the auditory filter as the mother wavelet, and called it the Auditory Wavelet Transform. As this resulted in a non-orthogonal transform, the reconstruction (as mentioned in Sec. 7.1) was not easy, and they used two indirect methods.

7.2. Application of filters

Besides the traditional classification of digital filters to FIR and IIR types, modern filters could be divided to non-decimated (standard) and decimated (usually critically sampled) filters. While critically sampled filters do not increase the data rate of the input signal they impose several important practical limitations. The construction of banks emulating constant Q filters is possible with the use of wavelet packets [44] and excellent filterbanks for the use in audio technology have recently been designed [2]. However, they tolerate little modifications to the channel signals, which are needed in ear modelling, e.g. in blocks no. 3. and no. 4. of Fig. 1.

Non-decimated filters offer much better flexibility, computational stability and robustness to distortion, and are thus more suitable for ear modelling. The cost of non-decimating is very high redundancy of the channel (output) data. Constant Q, one-third octave band or so-called Bark filters (with bandwith corresponding to 1 Bark) are often used [37].

Non-decimated filters with impulse responses simulating that of the cochlea have been investigated. In several models the so called "gammatone" linear filter has been used. Recently IRINO [17, 19] has proposed a more advanced filter called "the gammachirp" with level — dependent, asymmetric characteristics, showing that it was theoretically optimum filter, with minimum uncertainty in a joint time frequency representation. It is given by [17]:

$$g_c(t) = at^{n-1} \exp(-2\pi b \,\mathrm{ERB}\,(f_r)t) \cos(2\pi f_r t + c \ln t + \phi), \qquad t > 0, \tag{8}$$

where a, b, c, n, are parameters, which are tuned to obtain best results, f_r is the centre frequency of the filter, ϕ is the phase of the cosine carrier, ERB is the Equivalent Rectangular Bandwidth and t is time. As the ERB is a function of f_r the bandwidths of cochlear particular filters can be precisely tuned to experimental data, thus offering better fit that the constant Q filters do.

Without the frequency modulation "chirp" term ($c \ln t$) the impulse response in (8) is equivalent to the earlier "gammatone" filter.

8. Spectral enhancement

Since a seminal paper by MCAULAY and QUATIERI [26] several procedures for discarding weaker parts of the spectrum have been proposed. Such an operation has its foundations in physiological phenomena of masking and lateral inhibition (mentioned in

Sec. 3). It can be assumed that they both contribute at peripheral auditory stages to the overall ear's ability to isolate signals of interest out of an acoustic background. The procedures in [9, 16, 26] and many others are peak picking algorithms. They consist of finding local spectral peaks in subsequent spectra evolving with time and then in forming continuous traces in the three-dimensional amplitude versus time and frequency space.

On their output they all produce plots resembling the rightmost diagram in Fig. 1. Usually they provide substantial amount of data reduction. They differ in time-frequency analysis method used, selection (peak-picking) method, elimination of blocking effects and other details.

A simple way of achieving the same goal, albeit applicable only for stationary sounds of acoustic instruments with harmonic spectra was proposed in [22].

A different approach to modeling spectral enhancement was presented in [41, 42, 43]. The authors tried to simulate more precisely the physiological processes, with mixed partial derivative with respect to both time and space of the basilar membrane patterns as key contrast — enhancing operation, followed by nonlinearity (rectification).

9. Postulates for Auditory Transform

Auditory Transform is meant to be a multi-stage computational procedure (the term "transform" is used in a wide sense) which should serve two goals:

a) analyse an audio signal yielding a result similar to its internal representation at a suitable stage of the auditory system;

b) model the peripheral auditory system.

The most desirable properties of Auditory Transform are proposed below:

a) The first stage should be linear and perceptually invertible, i.e. a listener should not perceive any difference between an original signal and the reconstructed signal.

b) The careful design of frequency analysis part of this procedure is essential. If the WT is used for this stage, a good candidate is based on a mother wavelet that in some way approximates the characteristics of an auditory filter.

c) The subsequent nonlinear spectral enhancement procedure should eliminate redundancy from frequency analysis stage.

10. A proposal for a narrow-band wavelet transform

Following the discussion presented above, the author designed a specific wavelet transform to model the frequency analysis function of the ear. The choice of wavelet leads to a redundant (frame-based) wavelet transform. The construction and verification of the proposed WT is only summarized in this chapter.

There is a way of densely sampling of the CWT, keeping a simple structure of time allocation of transform coefficients. This is obtained by preserving a dyadic structure of sampling in time, with appropriate oversampling, while samples in the scale (frequency) domain are taken by filling the dyadic scale with additional samples, taken at fractional powers of two. Such samples in the scale domain are called "voices". If we denote the

continuous wavelet at scale (octave) m by $h_m(t)$, then the voice number j in that scale will be given by:

$$h_{m,j}(t) = 2^{-j/M} h_m(2^{-j/M} t), \tag{9}$$

where M is the number of voices per one octave.

The mother wavelet chosen for that transform was similar to the Morlet wavelet. The original Morlet wavelet [6] is the basis function of the Gabor Transform, i.e. it is the complex sinusoid windowed by the Gaussian envelope. Its important advantage is that it directly preserves phase, as the basis functions are complex. The frequency resolution of the original Morlet wavelet was found inappropriate and a specific window was proposed instead of the Gaussian. This window was derived from the modified Blackman window [14], by tuning its coefficients so that the spectrum of the window is as close as possible to frequency characteristics of auditory filters, within limitations of real-valued windows. The discrete formula for the window was the following:

$$w(n) = 0.4205 + 0.4995 \cos\left[\frac{2\pi}{N}\right] + 0.08 \cos\left[\frac{2\pi}{N} 2n\right], \qquad n = -\frac{N}{2}, \ldots, 0, \ldots, \frac{N}{2}, \tag{10}$$

where $N + 1$ is the length of the window in samples. Odd length was used following the practice used in FIR filter implementations, where it is usually better to have the filter response sampled exactly in its center. The amplitude spectrum of this window is shown in Fig. 2. The frequency resolution of the resulting wavelet is much better that than offered by responses of filters described in [17] and [19].

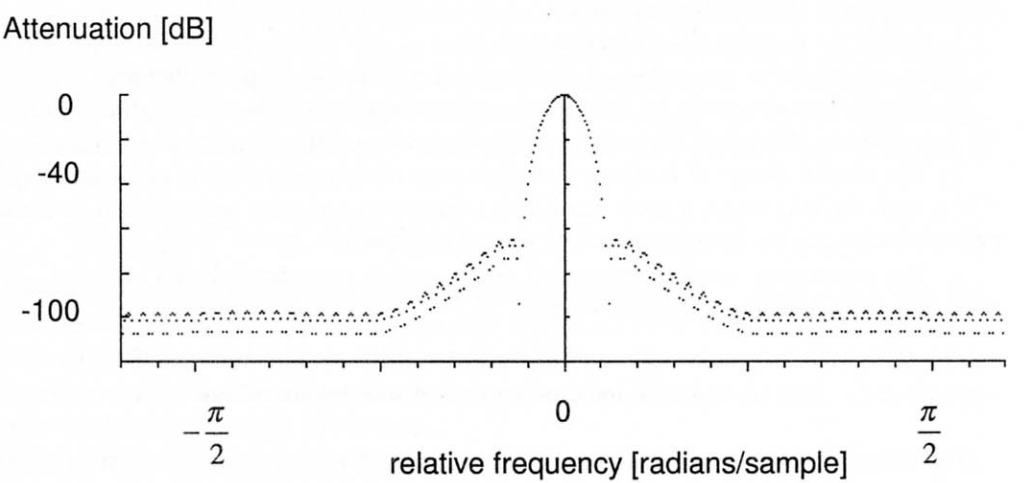

Fig. 2. Amplitude spectrum of the window used in the construction of the wavelet transform proposed.

The number of voices per octave (M in (9)) was chosen to be equal to 12, thus forming the 1/12 octave spacing of bands of frequency analysis, corresponding to the equally-tempered musical scale.

For computational reasons, the audio frequency range in the experimental system was reduced to from 30 Hz to 16 kHz. Also, the so-called scaling function, needed to

represent the lower part of the frequency spectrum was not used, without any audible effects. This range encompasses 9 octaves. Together, the transform proposed analyses the signal in 108 (9×12) frequency bands.

The overlapping factor in the time domain, after initial experiments has been chosen at 75% for the highest voice in an octave. The wavelets for subsequent, lower voices are scaled to be longer by appropriate fractional powers of 2 and effective overlapping range increases. Four coefficients are computed for any signal frame equal to the length of the window.

The 1/12 octave *spacing* between the bands did not determine their *width*. According to the discussion in Sec. 7.1, the transform was designed to be redundant, which means not only overlapping of frame analysis in time, but also overlapping of bands in scale (frequency) domain. Thus, the appropriate balance between the resolutions in frequency and in time had to be found. The width of the bands was chosen so that the point of intersection of amplitude spectra of neighbouring bandpass filters was approximately at −3 dB. That width is determined by the length of the mother wavelet. The wavelet for the lowest scale used (shortest wavelet) was 48+1 samples long, with other wavelets in this highest octave being longer. The mother wavelet consisted of 16 windowed cycles of the complex sinusoid (real part). The experiments have been carried with the sampling frequency of 48 kHz, thus the centre frequency of the highest wavelet was equal to 16 kHz. The transform encompassed 9 octaves, and the length of the lowest scale wavelet in the bottom octave was 23196+1 samples and its frequency was centred at 33.1 Hz.

The reconstruction of the signal by inverse WT, for unit impulse test signal shows some distortion, resulting from the frame used still being not tight enough. The amplitude of these distortions can be estimated at below −40 dB in relation to the amplitude of the unit impulse. However, when tested on many different samples of audio signals, no audible difference has been heard by a group of listeners. The distortion could be reduced by increasing the redundancy, but then its rate would be impractically high. The WT presented above produces exactly 4 times more of data than there were samples in an input signal. In fact, this number can be reduced to 3 without audible effect by just less dense sampling of the time — scale plane. Higher reductions were obtained and informally tested using specific procedures relying on rules from psychoacoustics. These procedures could be a basis for algorithms for spectral redundancy. The experiments on such procedures are currently conducted.

Figure 3 shows the plot of the analysis of a 150 ms fragment of the recording of an orchestra. The result displayed is based on the modulus of complex coefficients obtained from the WT proposed. For better clarity, the plot presented is of the discrete, black and white type, instead of often used grey-scale type. The threshold used for classification black/white was gradually lowered along the frequency scale, to compensate for the usual decrease of energy of the acoustic signal towards higher frequencies. All frequency bands in the plot are double-pixel wide for better visualisation, thus all short vertical strips in the highest octave are showing single transform coefficients. Despite that the very dense musical fragment was deliberately chosen and slightly smearing nature of the black/white plot, concentration of energy in time-frequency plane is clearly visible, with some horizontal strips indicating strong harmonic components.

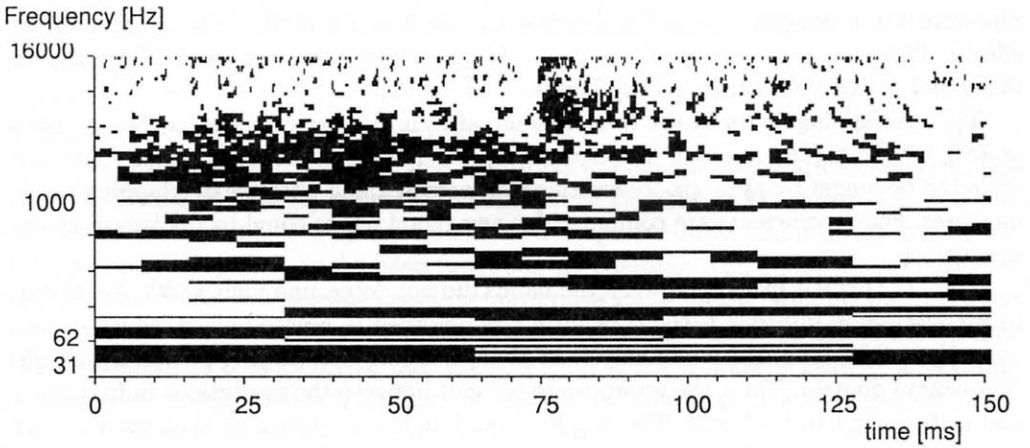

Fig. 3. The output of the transform proposed for a 150 ms fragment of orchestral music.

11. Conclusions

Analysis of the bibliography and the work performed by the author indicate, that successful modeling of the ear requires a specific linear frequency analysis procedure, which is a basis for any subsequent nonlinear operations. Its most important feature is constant Q bandpass filtering characteristics. One such method was proposed and tested. It relies on the Wavelet Transform with a modified Morlet mother wavelet, with oversampling the frequency domain by means of "voices". It performs well, but the data must be redundant by about four times, in order that the transform is perceptually invertible.

References

[1] A.N. Akansu, M.J.T. Smith [Eds.], *Subband and wavelet transforms*, Kluwer, Boston 1996.

[2] M. Bobrek, D.B. Koch, *Music segmentation using tree-structured filter banks*, Journal of the Audio Engineering Society, **46**, 5, 413–427 (1998).

[3] E. de Boer, *Classical and non-classical models of the cochlea*, J.A.S.A., **101**, 4, 2148–2150 (1997).

[4] J.C. Brown, *Calculation of a constant Q spectral transform*, J.A.S.A., **89**, 1, 425–434 (1990).

[5] C.S. Burrus, R.A. Gopinath, H. Guo, *Introduction to wavelets and wavelet transforms*, Prentice Hall, Upper Sadle River, NJ 1998.

[6] Y.T. Chan, *Wavelet basics*, Kluwer Academic Press, Norwell 1995.

[7] L. Cohen, *Time-frequency analysis*, Prentice Hall, Englewood Cliffs, NJ 1995.

[8] M.A. Cohen, S. Grossberg, L.L. Wyse, *A spectral network model of pitch perception*, J.A.S.A., **98**, 2, 862–885 (1995).

[9] A. Czyżewski, *New learning algorithms for the processing of old audio recordings*, 99th A.E.S Convention, Preprint no. 4078, New York 1995.

[10] I. Daubechies, *The wavelet transform, time-frequency localization and signal analysis*, IEEE Transactions on Information Theory, **36**, 5, 961–1005 (1990).

[11] Z. ENGEL, *Ochrona środowiska przed drganiami i hałasem*, Wydawnictwo Naukowe PWN, Warszawa 1993.

[12] J.L. FLANAGAN, *Models for approximating basilar membrane displacement*, The Bell System Technical Journal, 1163–1191 (1960).

[13] L.C. GRESHAM, L.M. COLLINS, *Analysis of the performance of a model-based optimal auditory signal processor*, J.A.S.A., **103**, 5, 2520–2529 (1998).

[14] F.J. HARRIS, *On the use of windows for harmonic analysis with the discrete Fourier transform*, Proceedings of the IEEE, **66**, 1, 51–83 (1978).

[15] W.M. HARTMANN, *Pitch, periodicity, and auditory organization*, J.A.S.A., **100**, 6, 3491–3502 (1996).

[16] W. HEINBACH, *Aurally adequate signal representation: The part-tone-time-pattern*, Acustica, **67**, 113–120 (1988).

[17] T. IRINO, *A "Gammachirp" function as an optimal auditory filter with the Mellin transform*, Proc. IEEE Int. Conf. on Acoustics, Speech and Signal Processing, 981–984, Atlanta 1996.

[18] T. IRINO, H. KAWAHARA, *Signal reconstruction from modified auditory wavelet transform*, IEEE Trans. on Signal Processing, **41**, 12, 3549–3554 (1993).

[19] T. IRINO. R.D. PATTERSON, *A time-domain, level dependent auditory filter: The gammachirp*, J.A.S.A., **101**, 1, 412–419 (1997).

[20] J.M. KATES, *A time-domain digital Cochlear model*, IEEE Trans. on Signal Processing, **39**, 12, 2573–2592 (1991).

[21] D.O. KIM, C.E. MOLNAR, R.R. PFEIFFER, *A system of nonlinear differential equations modeling basilar-membrane motion*, J.A.S.A., **54**, 6, 1517–1529 (1973).

[22] P. KLECZKOWSKI, *Nowy sposób kodowania parametrów dla syntezy addytywnej sygnałów*, Mat. VII Sympozjum Inżynierii i Reżyserii Dźwięku, 125–128, Kraków 1997.

[23] J. KOVACEVIC, M. VETTERLI, *Wavelets and subband coding*, Prentice Hall, Englewood Cliffs 1995.

[24] R.F. LYON, *An analog electronic cochlea*, IEEE Trans. on A.S.S.P., **36**, 7, 1119–1133 (1988).

[25] H.S. MALVAR, *Signal processing with lapped transforms*, Artech House, Boston 1992.

[26] R. J. MCAULAY, T.F. QUATIERI, *Speech analysis/synthesis based on a sinusoidal representation*, IEEE Trans. on A.S.S.P., **34**, 4, 744–754 (1986).

[27] R. MEDDIS, M.J. HEWITT, *Virtual pitch and phase sensitivity of a computer model of the auditory periphery. I. Pitch identification*, J.A.S.A., **89**, 6, 2866–2882 (1991).

[28] B.C. MOORE [Ed.], *Frequency selectivity in hearing*, Academic Press, London 1986.

[29] S.H. NAWAB, *Short-time Fourier transform*, [in:] J.S. LIM, A.V. OPPENHEIM [Eds.], Advanced Topics in Signal Processing, Prentice Hall, Englewood Cliffs, NJ 1988.

[30] B. PAILLARD, P. MABILLEAU, S. MORISETTE, J. SOUMAGNE, *PERCEVAL: Perceptual evaluation of the quality of audio signals*, Journal of the Audio Engineering Society, **40**, 1/2, 21–31 (1992).

[31] R.D. PATTERSON, *Auditory filter shapes derived with noise stimuli*, J.A.S.A., **59**, 3, 640–654 (1976).

[32] W.J. PIELEMEIER, G.H. WAKEFIELD, *A high resolution time-frequency representation for musical instrument signals*, J.A.S.A., **99**, 4, 2382–2396 (1996).

[33] J.-C. RISSET, D.L. WESSEL, *Exploration of timbre by analysis and synthesis*, [in:] The psychology of Music, D. DEUTSCH [Ed.], Academic Press, New York 1982, 26–58.

[34] M.R. SCHROEDER, J.L. HALL, *Model for mechanical to neural transduction in the auditory receptor*, J.A.S.A., **55**, 5, 1055–1060 (1974).

[35] S. SHLIEN, *The modulated lapped transform, its time-varying forms, and its applications to audio coding standards*, IEEE Trans. on Speech and Audio Proc., **5**, 4, 359–366 (1997).

[36] M. SLANEY, *Pattern playback in the '90s*, [in:] Advances in Neural Processing Systems 7, G. TESAURO, D. TOURETZKY, T. LEEN [Eds.], Morgan Kaufmann Publishers, San Mateo, CA, 1995.

[37] T. SPORER, K. BRANDENBURG, *Constraints of filter banks used for perceptual measurement*, J.A.E.S., **43**, 3, 107–116 (1995).

[38] G. STRANG, T. NGUYEN, *Wavelets and filter banks*, Wellesley – Cambridge Press, New York 1996.

[39] R. TADEUSIEWICZ, *Sygnał mowy*, WKiŁ, Warszawa 1988.

[40] P.P. VAIDYANATHAN, *Multirate systems and filter banks*, Prentice Hall, Englewood Cliffs, NJ 1993.

[41] X. YANG, K. WANG, S. SHAMMA, *Auditory representations of acoustic signals*, IEEE Trans. on Information Theory, **38**, 2, 824–839 (1992).

[42] K. WANG, S. SHAMMA, *Self-normalization and noise-robustness in early auditory representations*, IEEE Trans. on Speech and Audio Processing, **2**, 3, 421–435, July 1994.

[43] K. WANG, S. SHAMMA, *Spectral shape analysis in the central auditory system*, IEEE Trans. on Speech and Audio Processing, **3**, 5, 382–395 (1995).

[44] M.V. WICKERHAUSER, *Adapted wavelet analysis from theory to software*, IEEE Press, Piscataway, NJ 1994.

[45] E. ZWICKER, H. FASTL, *Psychoacoustics, facts and models*, Springer-Verlag, Berlin 1990.

[46] E. ZWICKER, T. ZWICKER, *Audio engineering and psychoacoustics: Matching signals to the final receiver, the human auditory system*, J.A.E.S., **39**, 3, 115–125 (1991).

ARCHIVES OF ACOUSTICS
24, 2, 207–212 (1999)

THE ACOUSTIC REACTANCE OF RADIATION OF A PLANAR ANNULAR MEMBRANE FOR AXIALLY-SYMMETRIC FREE VIBRATIONS

W.J. RDZANEK and W.P. RDZANEK, JR.

Pedagogical University
Department of Acoustics
(35-310 Rzeszów, ul. Rejtana 16a, Poland)

The imaginary part of the acoustic impedance of radiation of a planar, annular membrane is analyzed. Axially-symmetric free vibrations, sinusoidally varying in time, are considered. An annular membrane is placed in a planar, rigid baffle and radiates an acoustic wave into a loss-less, homogeneous, gaseous medium. The reactance of radiation is obtained in an elementary form for high frequencies of radiated waves.

1. Introduction

The energetic aspect of radiating sound source is characterized most often through the acoustic power research or the impedance of radiation research. It concerns both — the real component and the imaginary component.

The theoretical analysis of acoustic impedance of radiation of a vibrating piston ring was undertaken by many authors (e.g. MERRIWEATHER [2], THOMPSON [5] and WYRZYKOWSKI [6]).

In [3] there are presented formulas for the real component of the acoustic power of radiation of a planar, annular membrane into a hemisphere filled with a loss-less, gaseous medium.

Referring to results produced in [3] in this work the imaginary component of the impedance of radiation of an annular membrane is considered. The membrane is placed in a planar, rigid baffle. Axially-symmetric, sinusoidally varying in time, free vibrations are analyzed. A starting point for this analysis is an integral formula written in a plane of complex variable for the power radiated by a planar, annular membrane. The imaginary part of this formula is integrated in case of high frequency of the radiated acoustic wave. An expression for the reactance of radiation has been obtained of an elementary form, useful for numerical calculations, and is illustrated graphically.

Results obtained in this work can be applied for active methods (cf. [4]) for the radiation of sound of vibrating surface sources research.

The analytical results are used for practical applications of membranes modeling (cf. [1]).

2. The analysis assumptions

Axially-symmetric free vibrations of a planar, annular membrane are

$$\frac{\eta_n(r)}{A_n} = J_0\left(x_n\frac{r}{r_1}\right) - \frac{J_0(x_n)}{N_0(x_n)}N_0\left(x_n\frac{r}{r_1}\right) \tag{2.1}$$

$r_1 < r < r_2$, where J_0, N_0 are cylindrical functions of null order correspondingly BESSEL'S and NEUMANN'S. The value x_n is the n-th eigenvalue of the frequency equation

$$\frac{J_0(kx_n)}{J_0(x_n)} = \frac{N_0(kx_n)}{N_0(x_n)},$$

where $k = r_2/r_1 \geq 1$. Also: $k_n = \omega_n\sqrt{\sigma/T}$, ω_n is the n-th eigenfrequency, corresponding to the mode $(0,n)$, σ – is the surface density of the membrane, T – is the stretching force of the membrane. Eigenvalues x_n were calculated for $n = 1,2,...,6$, $k = 1.1, 1.2, 1.5, 2, 3$ and 5 and were placed in work [3].

Into a gaseous medium of rest density ϱ_0, propagation velocity of the acoustic wave c, averaged in time acoustic power [3] is radiated with frequency $\omega = k_0 c$, $k_0 = 2\pi/\lambda$.

$$N_n = N_n^{(\infty)}\frac{2\delta_n^2}{\alpha_n^2 - 1}\int_0^\infty \frac{x}{\gamma}\left\{\frac{\alpha_n J_0(k\beta x) - J_0(\beta x)}{x^2 - \delta_n^2}\right\}^2 dx, \tag{2.2}$$

where $\delta_n = x_n/\beta$, $\beta = k_0 r_1$, $\alpha_n = J_0(x_n)/J_0(kx_n)$, $\gamma = \sqrt{1-x^2}$ for $x < 1$ and $\gamma = -i\sqrt{x^2-1}$ for $x > 1$. Also $N_n^{(\infty)} = \lim\limits_{k_0\to\infty} N_n$ and

$$N_n^{(\infty)} = \frac{1}{2}\varrho_0 c\int_S v_n^2 dS, \qquad v_n = i\omega_n\eta_n(r),$$

where v_n is the vibration velocity of points of an annular membrane for the mode $(0,n)$.

Value $N_n/N_n^{(\infty)}$ is represents the normalized impedance of radiation $\zeta_n = \theta_n + i\chi_n$ of a planar, annular membrane for $(0,n)$ form of vibrations, θ_n is the normalized resistance (cf. [3]), χ_n is the normalized reactance.

3. The normalized radiation reactance

The normalized reactance of radiation $\chi_n = \Im\left(N_n/N_n^{(\infty)}\right)$ of a planar annular membrane for free vibrations $(0,n)$ have been derived from the formula (2.2)

$$\chi_n = \frac{2\delta_n^2}{\alpha_n^2 - 1}\int_1^\infty \left\{\frac{\alpha_n J_0(k\beta x) - J_0(\beta x)}{x^2 - \delta_n^2}\right\}^2 \frac{x\,dx}{\sqrt{x^2-1}}. \tag{3.1}$$

An integral of infinite limits $(1,\infty)$ integral of finite limits $(0,\pi/2)$ have been transformed to

$$\chi_n = \frac{2\delta_n^2}{\alpha_n^2 - 1}\int_0^{\pi/2} \left\{\frac{\alpha_n J_0(k\beta/\sin u) - J_0(\beta/\sin u)}{1 - \delta_n^2\sin^2 u}\right\}^2 \sin^2 u\,du \tag{3.2}$$

which is adequate formula for reactance for numerical calculations.

Integrating in the formula (3.1) we achieve with assumption that interference parameter $\beta = k_0 r_1 \gg 1$. Asymptotic formulas have been used

$$\begin{aligned} J_0^2(\beta x) &\sim \frac{1+\sin 2\beta x}{\pi\beta x}, \\ J_0(k\beta x)J_0(\beta x) &\sim \frac{1}{\pi\beta x\sqrt{k}}\left[\cos(k-1)\beta x + \sin(k+1)\beta x\right] \end{aligned} \tag{3.3}$$

and

$$\int_1^\infty \frac{e^{imx}dx}{\sqrt{x^2-1}\,(x^2-\delta_n^2)^2} = \sqrt{\frac{\pi}{2m}}\left\{(1-\delta_n^2)^{-2} + O\left(\frac{1}{m}\right)\right\} e^{i(m+\pi/4)} \tag{3.4}$$

if $m \gg 1$.

Also an integral formula is helpful

$$\int_1^\infty \frac{dx}{\sqrt{x^2-1}\,(x^2-\delta_n^2)^2} = \frac{1}{2\delta_n^2(1-\delta_n^2)}\left(1 + \frac{2\delta_n^2-1}{\delta_n\sqrt{1-\delta_n^2}}\arcsin\delta_n\right). \tag{3.5}$$

After using the asymptotic method of calculations instead the formula (3.1) we get

$$\begin{aligned} \chi_n = \left[\pi\beta(\alpha_n^2-1)(1-\delta_n^2)\right]^{-1} &\left[\left(1+\frac{\alpha_n^2}{k}\right)\left(1+\frac{2\delta_n^2-1}{\delta_n\sqrt{1-\delta_n^2}}\arcsin\delta_n\right)\right. \\ &\left. + \sqrt{\pi/\beta}\,\frac{\delta_n^2}{1-\delta_n^2}F_n(k,\beta)\right] \end{aligned} \tag{3.6}$$

with error $O(\delta_n^2\,\beta^{-3/2})$, where the function

$$\begin{aligned} F_n(k,\beta) \equiv \sin\left(2\beta+\frac{\pi}{4}\right) + \frac{\alpha_n^2}{k\sqrt{k}}\sin\left(2k\beta+\frac{\pi}{4}\right) \\ - 2\sqrt{2}\,\frac{\alpha_n}{\sqrt{k}}\left[\frac{\sin\left((k+1)\beta+\frac{\pi}{4}\right)}{\sqrt{k+1}} + \frac{\cos\left((k-1)\beta+\frac{\pi}{4}\right)}{\sqrt{k-1}}\right] \end{aligned} \tag{3.7}$$

has essential influence on "oscillating" character of reactance (3.6). The formula (3.6) represents the elementary form of an expression, convenient for calculations of normalized reactance of an annular membrane in the case of high frequency of radiated waves, when the source vibrates with n-th axially-symmetric mode.

4. Concluding remarks

As a result of theoretical analysis of the planar, annular membrane radiation formulas (3.1) and (3.6) for normalized radiation reactance have been derived.

Elementary formula (3.6) can be used for numerical calculations only if condition $x_n < \beta = k_0 r_1$ is satisfied. There have been isolated components, which have essential influence on "oscillating" character of changes of radiation reactance (Fig. 1, 2 and 3).

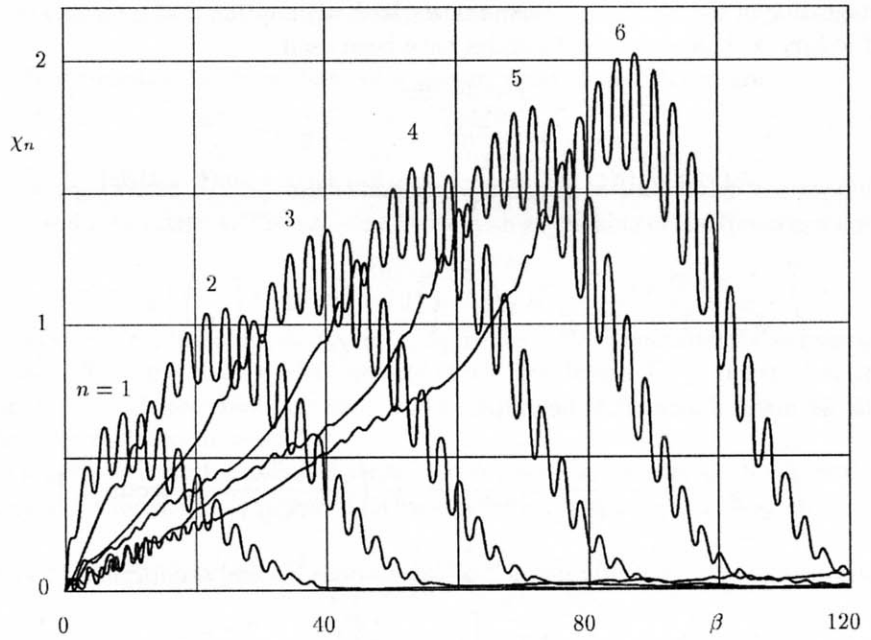

Fig. 1. Normalized reactance of radiation of a planar annular membrane versus β for the modes $(0, n)$, $n = 1, 2, ..., 6$ and $k = 1.2$.

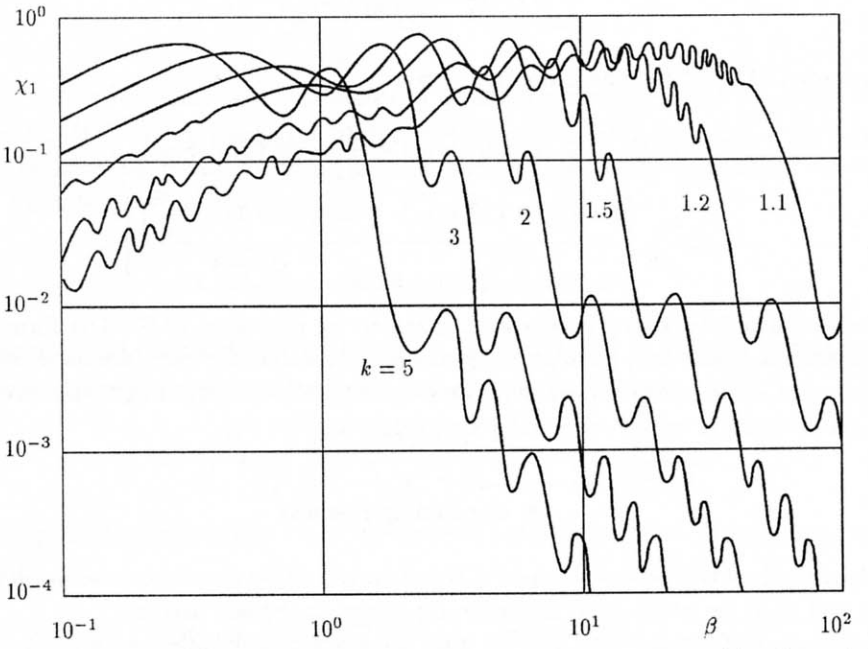

Fig. 2. Normalized reactance of radiation of a planar annular membrane versus β for the mode $(0, 1)$ and different k.

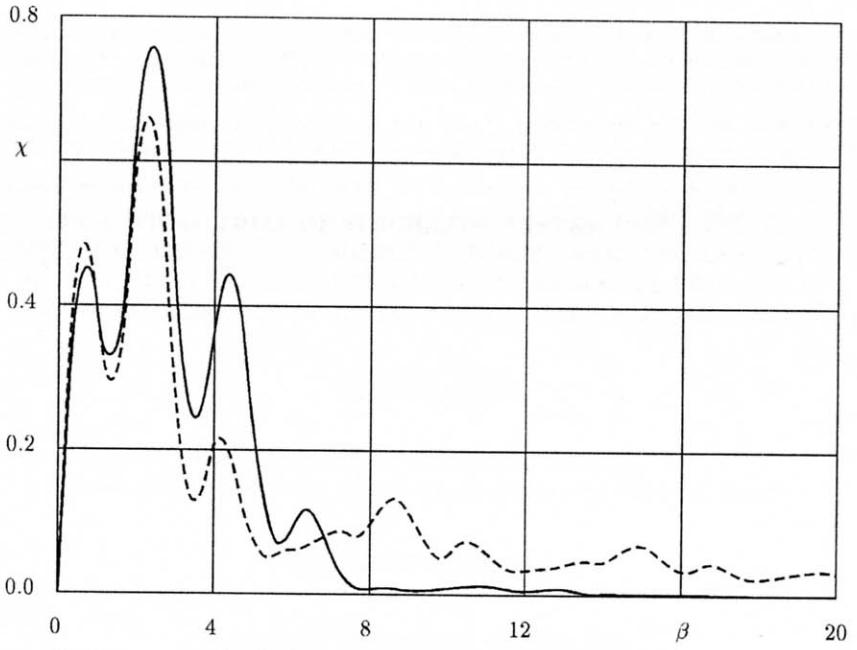

Fig. 3. Normalized reactance of radiation of a planar annular source versus parameter β for $k = 2$. The annular membrane for the mode $(0,1)$ – solid line, the annular piston – dashed line.

In the case when the condition $x_n < \beta$ is not satisfied or when high precision of results is necessary, calculations must be made using the integral formula (3.1).

For comparison — apart of frequency characteristics of vibrating annular membrane — there have been presented a graph of radiation reactance of an annular piston.

On the basis of presented graphical illustration one can draw a conclusion that the radiation reactance of an annular membrane depends on: its sizes $k = r_2/r_1$, its form of vibrations $(0, n)$ and the interference parameter $\beta = k_0 r_1$.

Obtained formulas (3.1) and (3.6) can be used to describe the acoustic radiation of a vibrating system more complicated and less idealized. The example of analysis of such a system can be calculation of distribution of acoustic pressure or acoustic power, radiated by an annular membrane with consideration of the vibration force factor. Taking into account the reflexive interaction of radiated pressure wave of surrounding medium is also possible.

References

[1] F. FONTANA and D. ROCCHESSO, *Physical modeling of membranes for percusian instruments*, Acustica/Acta Acustica, **84**, 3, 529–542 (1998)

[2] A.S. MERRIWEATHER, *Acoustic radiation impedance of a rigid annular ring vibrating in an infinite rigid baffle*, Journal of Sound and Vibrations, **10**, 3, 369–379 (1969).

[3] W.J. RDZANEK and W.P. RDZANEK JR., *The real acoustic power of a planar annular membrane radiation for axially-symmetric free vibrations*, Archives of Acoustics, **22**, 4, 455–462 (1997).

[4] C.C. SUNG and C.Y. HUANG, *Comparison of active control effect in terms of structural and radiation modes for transmited soud power through thin plate*, [in:] Proc. of the International Symposium on active control of sound and vibration ACTIVE'97, pp. 1049–1062, Budapest 1997.

[5] W. THOMPSON, JR., *The computation of self- and mutual-radiation impedances for annular and elliptical pistons using Bouwkamp's integral*, Journal of Sound and Vibrations, **17**, 2, 221–233 (1971).

[6] R. WYRZYKOWSKI *et al.*, *Selected problems on the theory of the acoustic field*, [in Polish], Fosze Publishers, Rzeszów 1994.

ARCHIVES OF ACOUSTICS
24, 2, 213–220 (1999)

A PRACTICAL TRIAL OF STOCHASTIC SYSTEM IDENTIFICATION UNDER EXISTENCE OF BACKGROUND NOISE BASED ON EQUIVALENCE OF STATISTICS AND ITS APPLICATION TO RESPONSE PROBABILITY EVALUATION OF ACOUSTIC SYSTEM WITH MUSIC INPUT

MITSUO OHTA

Honorary Professor of Hiroshima University
(1106, 1-7-10 Matoba-cho, Minami-ku, Hiroshima City, 732-0824, Japan)

KIMINOBU NISHIMURA

Faculty of Engineering, Kinki University
(5-1-3 Hiro Koshingai, Kure Shi, 737-0112, Japan)

A practical identification method of functional type for sound insulation systems is derived especially in the form matched to the prediction problem of output response probability distribution once after introducing some new evaluation criteria on output statistics. The probability distribution of output response with an arbitrary input sound under the contamination of background noise is principally able to predict theoretically by positively using the statistics of input and background noises based on the physical law of intensity linearity. More specifically, the system parameters of the objective sound insulation system are systematically identified by employing an equivalence property between the experimentally observed output probability distribution and the theoretically predicted one as a criterion of the parameter identification. As an application to the actual noise environment, the proposed method has been concretely applied to a double walls sound insulation system and experimentally confirmed under a music sound input.

Keywords: *system identification, probabilistic evaluation, environmental noise, sound insulation system, prediction of output distribution*

Notations

η	intensity of output noise,
ξ_i	intensity of input noise in the i-th frequency band,
ζ	intensity of external background noise,
a_i	system parameter for i-th frequency band,
N	number of frequency component band in overall frequency range,
x_i	level observation of ξ_i,
y	level observation of η,
v	level observation of ζ,
$P(y)$	probability density function of y,
$H_n()$	n-th order Hermite polynomial,
n	order of approximation,
L	upper limit of approximation,

μ	mean value of y,
σ^2	variance of y,
A_n	n-th order expansion coefficient,
$\langle\ \rangle$	time average,
$M_y()$	moment generating function of y,
M	$10/\log_e 10$,
ε_0	$10^{-12}\,\mathrm{W/m^2}$,
$\mathbf{a}$	vector of system parameter,
$\mu_T(\mathbf{a})$	theoretically estimated mean value under the estimation $\mathbf{a}$,
$\sigma_T^2(\mathbf{a})$	theoretically estimated variance under the estimation $\mathbf{a}$,
$A_{Tn}(\mathbf{a})$	theoretically estimated coefficient under the estimation $\mathbf{a}$,
$\widehat{\mathbf{a}}^{(k)}$	estimation of $\mathbf{a}$ at k-th stage,
Γ	Robbins Monro's gain diagonal matrix,
$P_T(y:\mathbf{a})$	theoretically estimated p.d.f. under the estimation $\mathbf{a}$,
$Q(y)$	cumulative distribution of $P(y)$,
z	integral variable,
L_x	noise evaluation index.

1. Introduction

As is well-known, a sound insulation system is usually evaluated by its transmission loss [1, 2, 3] given by the difference of sound pressure levels between input and output in each frequency band. On the other hand, it is usual that not only the input sound showing several types of probability distribution form but also the output response is observed under an inevitable contamination by a background noise of arbitrary distribution type. Furthermore, in addition to the lower order moment statistics like mean and variance of sound levels, L_{eq} and noise indexes like $(100-x)$ percentile L_x closely connected with a whole cumulative probability distribution form of sound level are actually employed to evaluate the environmental noises [4].

In this study, first, we pay our attention to a probability prediction problem on the output response of a sound insulation system in a room acoustics. So, not from a bottom up way of thinking like the standard type of analytical method along to the physical law, our main concern is paid to the prediction on a whole probability distribution form of the system output response on a dB scale based on the functional introduction of some object-oriented type evaluation criteria. That is, the probability distribution of the output response with an arbitrary stochastic input (e.g. music sound) under an avoidable contamination of background noise is able to be predicted by using the statistics of input and background noises based on the physical law of intensity linearity. More concretely, by employing the equivalence property between the experimentally observed output probability distribution and the theoretically predicted one as a criterion of the parameter identification, the system parameters of the objective sound insulation system are systematically identified. Then, the probability distribution of output response can be estimated with use of the statistical Hermite type expansion expression [5] reflecting the system parameters, the statistics of input and background noises observed on dB scale.

As an application to the actual noise environment, the proposed method is concretely applied to an evaluation problem of double walls sound insulation system excited by

a music sound input under the contamination of background noise at an observation point. The system parameters and the probability distribution form of output response are theoretically predicted and compared with the experimentally observed data. It is noteworthy that the system parameters are identified without employing the standard type frequency analysis like the 1/1 or 1/3 octave band analysis for the system output.

2. Model of sound environmental system

In the standard frequency analysis directly connected to the physical countermeasure, it is usual that a sound insulation system can be usually described by a linear system on the intensity scale in a frequency domain and is contaminated by an additional background noise of arbitrary distribution type at an observation point as follows:

$$\eta = \sum_{i=1}^{N} a_i \xi_i + \zeta. \tag{1}$$

3. The output response probability distribution of sound insulation system

As is well-known, an arbitrary type probability density function (abbr. p.d.f.) on the continuous level can be universally expressed in the form of statistical Hermite type expansion expression [5].

$$P(y) = \frac{1}{\sqrt{2\pi}\sigma} e^{-\frac{(y-\mu)^2}{2\sigma^2}} \left\{ 1 + \sum_{n=3}^{L} \frac{1}{n!} A_n H_n\left(\frac{y-\mu}{\sigma}\right) \right\} \qquad (L \to \infty) \tag{2}$$

with distribution parameters

$$\mu \triangleq \langle y \rangle, \qquad \sigma^2 \triangleq \langle (y-\mu)^2 \rangle \qquad \text{and} \qquad A_n \triangleq \left\langle H_n\left(\frac{y-\mu}{\sigma}\right) \right\rangle. \tag{3}$$

On the other hand, by considering Eq. (1), the moment generating function of the above p.d.f. $P(y)$ can be easily derived as follows:

$$M_y\left(\frac{\theta}{M}\right) \triangleq \left\langle e^{\frac{\theta}{M} y} \right\rangle = \frac{\langle \eta^\theta \rangle}{\varepsilon_0^\theta} = \sum_{r=0}^{\theta} \binom{\theta}{r} X_r \left\langle e^{\frac{\theta - r}{M} v} \right\rangle, \tag{4}$$

where

$$X_r \triangleq \sum_{r_1 + r_2 + \cdots + r_N = r} \frac{a_1^{r_1} a_2^{r_2} \cdots a_N^{r_N}}{r_1! r_2! \cdots r_N!} \left\langle e^{\frac{r_1}{M} x_1 + \frac{r_2}{M} x_2 + \cdots + \frac{r_N}{M} x_N} \right\rangle,$$

$$M \triangleq 10/\log_e 10 \qquad \text{and} \qquad \varepsilon_0 = 10^{-12}\,\mathrm{W/m^2}.$$

By taking the well-known relationship between the moment generating function, Eq. (4) and the cumulant statistics of y into consideration, the distribution parameters defined in Eq. (3) can be estimated by employing the statistics of input and background noises as follows:

$$\begin{bmatrix} \frac{\mu}{M} \\ \frac{\sigma^2}{M^2} \\ \frac{\sigma^3}{M^3}A_3 \\ \frac{\sigma^4}{M^4}A_4 \end{bmatrix} = \begin{bmatrix} 4 & -3 & \frac{4}{3} & -\frac{1}{4} \\ -\frac{26}{3} & \frac{19}{2} & -\frac{14}{3} & \frac{11}{12} \\ 9 & -12 & 7 & -\frac{3}{2} \\ -4 & 6 & -1 & 1 \end{bmatrix} \begin{bmatrix} \ln\left\{\sum_{r=0}^{1} X_r \left\langle e^{\frac{1-r}{M}v}\right\rangle\right\} \\ \ln\left\{\sum_{r=0}^{2} \binom{2}{r} X_r \left\langle e^{\frac{2-r}{M}v}\right\rangle\right\} \\ \ln\left\{\sum_{r=0}^{3} \binom{3}{r} X_r \left\langle e^{\frac{3-r}{M}v}\right\rangle\right\} \\ \ln\left\{\sum_{r=0}^{4} \binom{4}{r} X_r \left\langle e^{\frac{4-r}{M}v}\right\rangle\right\} \end{bmatrix}. \tag{5}$$

Hereupon, the expression of p.d.f. in Eq. (2) is approximately employed by letting $L = 4$. Therefore, by substituting the solution of Eq. (5) into Eq. (2), the output probability distribution of a sound insulation system can be explicitly estimated.

4. Identification of system parameters

The Eq. (5) can be regarded as a simultaneous nonlinear equation with respect to system paremeters a_i's through the variables X_r's. So, the system parameters can be estimated by solving the some complicated nonlinear equation Eq. (5) with respect to a_i's. Here, let us employ the well-known stochastic approximation method to solve it under two kinds of criterions on the equivalency of theoretically estimated p.d.f. and experimentally observed one of the output response.

Agreement of distribution parameters [Method I]

Let us introduce the following criterions with respect to each distribution parameter:

$$\begin{aligned} \mu_T(\mathbf{a}) - \mu &= 0, \\ \sigma_T^2(\mathbf{a}) - \sigma^2 &= 0, \\ A_{Tn}(\mathbf{a}) - A_n &= 0, \end{aligned} \tag{6}$$

where $\mu_T(\mathbf{a})$, $\sigma_T^2(\mathbf{a})$ and $A_{Tn}(\mathbf{a})$ are obtained by Eq. (5) with use of $\mathbf{a} \triangleq (a_1, a_2, \ldots, a_N)^T$. Parameters μ, σ^2 and A_n are directly obtained ones from the actual output response observation. Then, the system parameters can be estimated successively by using the following algorithm of the stochastic approximation method [6]:

$$\widehat{\mathbf{a}}^{(k)} = \widehat{\mathbf{a}}^{(k-1)} - \Gamma_k \begin{bmatrix} A_{T1}\left(\widehat{\mathbf{a}}^{(k-1)}\right) - H_1\left(\dfrac{y^{(k-1)} - \mu}{\sigma}\right) \\ \vdots \\ A_{TN}\left(\widehat{\mathbf{a}}^{(k-1)}\right) - H_N\left(\dfrac{y^{(k-1)} - \mu}{\sigma}\right) \end{bmatrix}, \tag{7}$$

with

$$\widehat{\mathbf{a}}^{(k)} \triangleq \left(\widehat{a}_1^{(k)}, \widehat{a}_2^{(k)}, \ldots, \widehat{a}_N^{(k)}\right)^T,$$

$$A_{T1}(\mathbf{a}) \triangleq \frac{\mu_T(\mathbf{a}) - \mu}{\sigma} \quad \text{and} \quad A_{T2}(\mathbf{a}) \triangleq \frac{\sigma_T^2(\mathbf{a}) - \sigma^2}{\sigma^2}.$$

Agreement of whole distribution shape [Method II]

Let us introduce the well-known least-squares error criterion with respect to the estimation error between $P_T(y : \mathbf{a})$ calculated by Eq. (2) and the corresponding experimental one, as follows:

$$\left\langle \{P_T(y : \mathbf{a}) - P(y)\}^2 \right\rangle \longrightarrow \min. \tag{8}$$

Then, the system parameters can be estimated successively by using the following algorithm on the stochastic approximation method:

$$\widehat{\mathbf{a}}^{(k)} = \widehat{\mathbf{a}}^{(k-1)} - \Gamma_k \begin{bmatrix} \dfrac{\partial}{\partial \widehat{a}_1^{(k-1)}} P_T(y_k; \widehat{\mathbf{a}}^{(k-1)}) \\ \vdots \\ \dfrac{\partial}{\partial \widehat{a}_N^{(k-1)}} P_T(y_k; \widehat{\mathbf{a}}^{(k-1)}) \end{bmatrix} \left\{ P_T(y_k; \widehat{\mathbf{a}}^{(k-1)}) - P(y_k) \right\}. \tag{9}$$

5. Experimental consideration

5.1. Experimental arrangement

Figure 1 shows an experimental arrangement in two reverberation rooms. Here, the speaker 1 excites the transmission room, two microphones can receive the input and output sound level fluctuations of an insulation system and the speaker 2 radiates the background noise into the reception room. For simulating an actual living environment, a music sound (rock music) has been positively employed as the input noise. A white noise has been employed as the background noise. Double walls consisting of aluminum panel with 1.2 mm thickness and surface mass 3.22 kg/m^2 have been employed as a partition wall. The overall response fluctuation has been observed over about 10 minutes with a sampling rate of 0.5 sec under the contamination of a background noise. Each frequency component of the input has been obtained simultaneously by employing the octave band analysis.

5.2. Identification of system parameters

The system identification has been carried out by solving the Eq. (7) with the first half of observed data. The estimation results of system parameters calculated under two methods ([Method I] and [Method II]) are shown in Table 1 as the transmission losses on dB. Experimentally observed transmission losses obtained actually by the usual octave band analysis with a usual white noise are also shown in Table 1 as "Experiment".

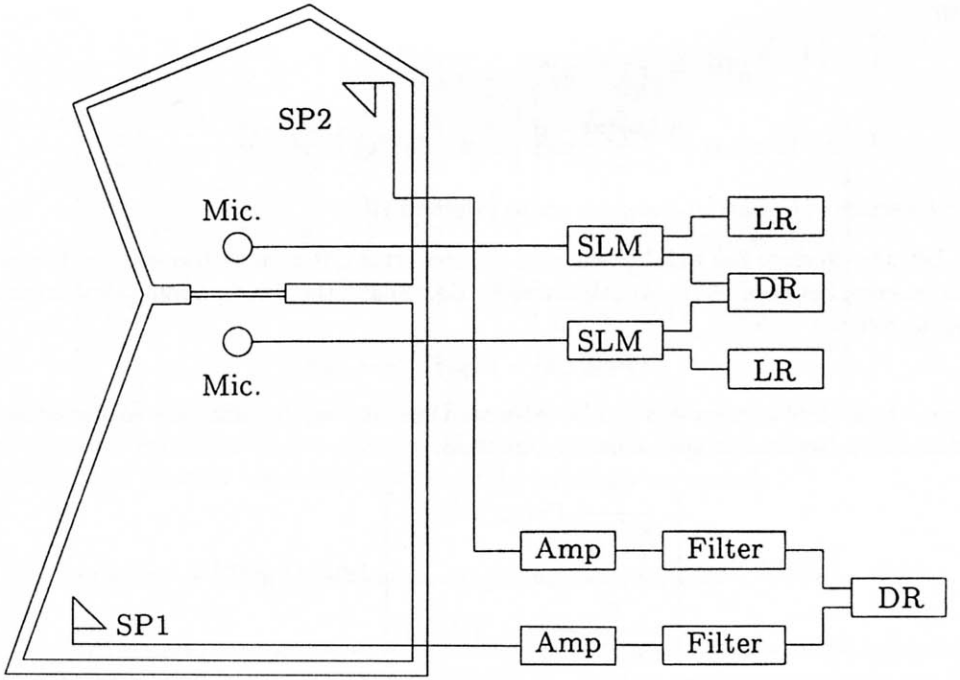

Fig. 1. Experimental arrangement in two reverberation rooms.

Table 1. Estimation results of the system parameters (Transmission loss).

Method	a_1(250 Hz)	a_2(500 Hz)	a_3(1 kHz)
Method I	9.72	20.46	25.63
Method II	9.71	20.67	26.75
Experiment	11.69	21.05	28.19

[dB]

5.3. Probability distribution for output response of sound insulation system

The probability distribution form of output response can be estimated with use of Eq. (2) by substituting the distribution parameters calculated in Eq. (5) with previously estimated system parameters, the statistics of input and background noises. Here, in close relation to the usual noise evaluation index, L_x noise level, Eq. (2) is evaluated especially in a cumulative distribution form as:

$$Q(y) = \int_{-\infty}^{y} P(z)\,dz. \tag{10}$$

The output cumulative distribution of a double walls sound insulation system is estimated for the first half of total observation data of non-stationary type used in the identification process of the system parameters. The estimations were carried out for

two cases with and without background noise at the system output. The results are shown in Fig. 2 with comparisons to the experimentally observed cumulative probability distributions of the system output noise.

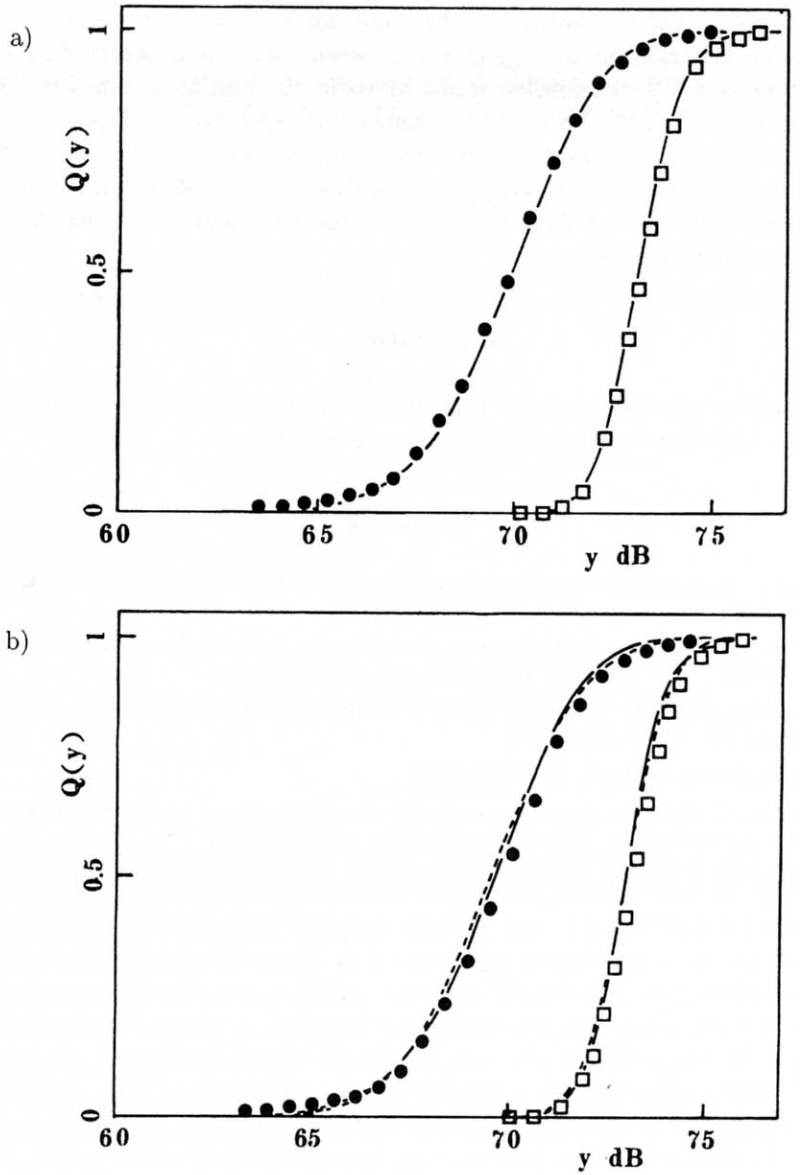

Fig. 2. Comparisons between experimentally sampled points and theoretically estimated curves for the output probability distribution of double walls sound insulation system with and without the effect of background noise under a music sound input: (a) Method I and (b) Method II. Experimentally observed points for output noise response are marked by • without background noise and □ with background noise. Theoretical curves are shown with the degree of approximation n in Eq. (2) as - - - - -, n=0 (for case (b)); ——, n=4.

6. Conclusions

In this study, first, a systematical identification method of sound insulation system with arbitrary input fluctuation of non-Gaussian type has been theoretically proposed under a contamination of arbitrary background noise especially by introducing some new evaluation criterion on the agreement between theory and observation for input and output probability distribution forms or their distribution parameters. Then, as an application to the actual sound environment, the proposed evaluation method is employed for the evaluation of double walls sound insulation system excited by a music sound. Finally, by using the proposed method, it seems possible to identify the actual sound insulation system in a daily living environment without employing the standard type usual frequency analysis.

Acknowledgement

We express our cordial thanks to Prof. Kazutatsu Hatakeyama, Dr. Akira Ikuta and Mr. Motomu Ueda for their helpful discussions and assistance.

References

[1] A. LONDON, *Transmission of reverberant sound through single wall*, J. Res. Nat. Bur. of Stand., **42**, 605–615 (1949).

[2] A. LONDON, *Transmission of reverberant sound through double walls*, J. Acoust. Soc. Am, **22**, 270–279 (1959).

[3] K.A. MULHOLLAND, H.D. PARBROOK and A. CUMMINGS, *The transmission loss of double panels*, J. Sound and Vib., **6**, 324–334 (1967).

[4] *Japanese Industrial Standard*, JIS Z-8731-1983.

[5] M. OHTA and T. KOIZUMI, *General statistical treatment of response of nonlinear rectifying device to stationary random input*, IEEE Trans. IT, **IT-14**, 595–598 (1968).

[6] H. ROBBINS and S. MONRO, *Stochastic approximation method*, Ann. of Math. Statist., **22**, 400–407 (1951).

ARCHIVES OF ACOUSTICS
24, 2, 221–232 (1999)

SOME PRECISE EVALUATION THEORY OF L_{eq} USING A WIDE SENSE DIGITAL FILTER AND ITS APPLICATION TO TRFFIC NOISE

MITSUO OHTA

Honorary Professor of Hiroshima University
(1106, 1-7-10 Matoba-cho, Minami-ku, Hiroshima City, 732-0824, Japan)

AKIRA IKUTA

Faculty of Human Life & Environmental Science,
Hiroshima Women's University
(1-1-71 Ujina-Higashi, Minami-ku, Hiroshima City, 734-0003, Japan)

YASUO MITANI

Faculty of Engineering, Fukuyama University
(Sanzo, 1 Gauen-cho, Fukuyama City, 729-0292, Japan)

1. Introduction

In a usual modeling method for actual stochastic systems, it is very often to find some idealized model by paying attention to only the average form of stochastic phenomena. Namely, the deviations form this idealized model are artificially treated as some meaningless information. Especially in a case when considering an arbitrary non-linear system with non-Gaussian input signals, however, the available informations still remain in these deviations in order to estimate and predict precisely some stochastic characteristics, e.g., the probability density function (abbr., p.d.f.), the cumulative distribution function (abbr., c.d.f.) and the higher order non-linear correlation functions. In the usual modeling methods for actual systems, the deviations from the actual phenomena occur inevitably owing to the model constructions under the idealized conditions.

In the evaluation problem of L_{eq} noise index, we first propose a new modeling method with the ability of extracting the available information in the deviations from an idealized L_{eq} evaluation model by considering not only the averaged form of actual systems but also the deviations from its averaged form. More specifically, we first introduce an additive correction term with probabilistic characteristics as the above deviations by

expressing the fluctuations around the averaged form. Next, in order to find the regression relationship between the correction term and a stochastic input signal, a prediction method for the output response probability is proposed by introducing a generalized regression analysis method of an extended type with less information loss [1]. Especially from the acoustical point of view, the noise L_{eq} evaluation index for road traffic noise can be predicted by using an averaged headway interval, a distance between a track lane and an observation point, and an A-weighted average power level. This idealized prediction formula has been constructed by paying attention to only an averaged form such as the headway interval and the power level. In the averaging process especially for headway intervals, it should be done based on the infinite data length from the statistical point of view. In the actual calculation of averaging process, however, we cannot help calculating the average by using the finite data length measured actually. Therefore, in this paper, by utilizing the statistical properties of the deviations between the measured values of L_{eq} and the above idealized prediction formula, we propose a precise method for predicting the c.d.f. (or p.d.f.) for the fluctuation of L_{eq}. In this case, the variability of L_{eq} is caused by essentially the complicated traffic flow. The stochastic prediction of this L_{eq} fluctuation even at an fixed measurement point is fairly difficult by only using the averaged traffic property based on the usual statistical approaches established under the linear and/or Gaussian assumptions. For the purpose of grasping precisely the statistical property of the L_{eq} fluctuation, we introduce reasonably the extended regression with less information loss. That is, after learning the regression relationship between the above-mentioned deviations and the averaged headway intervals (reflecting the traffic flow) through the learning data, we can predict precisely the c.d.f. (or p.d.f.) of unknown L_{eq} by use of the proposed prediction method. Namely, by introducing reasonably the stochastic correction term for an idealized L_{eq} prediction model, a new stochastic prediction method of L_{eq} is proposed based on the extended regression analysis method.

Moreover, by paying attention to the actual measurement under the existence of background noise, a recursive estimation algorithm for the regression parameter is proposed by introducing a wide sense digital filter. The effectiveness of the proposed method is experimentally confirmed by applying it to the prediction problem of a noise evaluation index for road traffic noise.

2. Theoretical consideration

2.1. Prediction method of output response probability by using an extended regression analysis method

Now, let us introduce the system model by taking account of the deviations from an idealized system model, as follows:

$$y = f(x, a) + \varepsilon(x), \tag{1}$$

where x denotes a stochastic input signal to a stochastic system under consideration, and y denotes its output fluctuation. Furthermore, it is assumed that the construction of an

idealized model $f(\bullet)$ and a parameter a contained in it are known. The whole available informations between ε and x are reflected in the conditional p.d.f. $P(\varepsilon|x)$. Based on the previously reported regression analysis method [1] with less information loss, let us first expand the joint p.d.f. $P(x,\varepsilon)$ in an orthogonal series expansion type as follows:

$$P(x,\varepsilon) = P_0(x)P_0(\varepsilon)\sum_{m=0}^{\infty}\sum_{n=0}^{\infty}A_{mn}\varphi_m^{(1)}(x)\varphi_n^{(2)}(\varepsilon), \tag{2}$$

$$A_{mn} \equiv \left\langle \varphi_m^{(1)}(x)\varphi_n^{(2)}(\varepsilon)\right\rangle. \tag{3}$$

Here, these fundamental p.d.fs. $P_0(\varepsilon)$ and $P_0(x)$ can be determined in advance as the p.d.fs. describing the dominant parts of each fluctuation, or chosen artificially among the well-known standard p.d.fs. (e.g., Gaussian distribution or gamma distribution). Furthermore, $\varphi_m^{(1)}(x)$ and $\varphi_n^{(2)}(\varepsilon)$ denote orthogonal polynomials with two weighting functions $P_0(\varepsilon)$ and $P_0(x)$ satisfying the following orthonormal conditions, respectively:

$$\int \varphi_m^{(1)}(x)\varphi_n^{(1)}(x)P_0(x)\,dx = \delta_{mn}, \tag{4}$$

$$\int \varphi_m^{(2)}(\varepsilon)\varphi_n^{(2)}(\varepsilon)P_0(\varepsilon)\,d\varepsilon = \delta_{mn}. \tag{5}$$

It should be noted that various types of correlation informations between x and ε are reflected hierarchically in the expansion coefficient A_{mn} $(m \neq 0,\ n \neq 0)$. From Eq. (2), the marginal p.d.f. $P(x)$ can be derived as

$$P(x) = P_0(x)\sum_{m=0}^{\infty}A_{m0}\varphi_m^{(1)}(x). \tag{6}$$

By substituting Eqs. (2) and (6) into Bayes' theorem about the definition of conditional p.d.f., the objective conditional p.d.f. $P(\varepsilon|x)$ is derived as follows:

$$P(\varepsilon|x) = \frac{P_0(\varepsilon)\displaystyle\sum_{m=0}^{\infty}\sum_{n=0}^{\infty}A_{mn}\varphi_m^{(1)}(x)\varphi_n^{(2)}(\varepsilon)}{\displaystyle\sum_{m=0}^{\infty}A_{m0}\varphi_m^{(1)}(x)}. \tag{7}$$

Thus, based on this conditional p.d.f., the l-th order regression function is derived as

$$\langle\varepsilon|x\rangle \equiv \int_{-\infty}^{\infty}\varepsilon P(\varepsilon|x)\,d\varepsilon = \frac{\displaystyle\sum_{m=0}^{\infty}\sum_{n=0}^{l}A_{mn}c_{ln}\varphi_m^{(1)}(x)}{\displaystyle\sum_{m=0}^{\infty}A_{m0}\varphi_m^{(1)}(x)}, \tag{8}$$

where the expansion coefficient c_{li} can be calculated in advance by using the following expansion type expression:

$$\varepsilon^l = \sum_{i=0}^{l}c_{li}\varphi_i^{(2)}(\varepsilon). \tag{9}$$

By using the probabilistic measure preserving transformation of $P(\varepsilon|x)$, the conditional p.d.f. of the output signal y is estimated by

$$P(y|x) = P(\varepsilon = y - f(x,a)|x). \tag{10}$$

Therefore, the output response p.d.f. $P(y)$ and its c.d.f. expression $Q(y)$ can be respectively evaluated as follows:

$$P(y) = \langle P(y|x)\rangle_x = \langle P(\varepsilon = y - f(x,a)|x)\rangle_x, \tag{11}$$

$$Q(y) = \int_{-\infty}^{y} P(y)\,dy = \int_{-\infty}^{y} \langle P(\varepsilon = y - f(x,a)|x)\rangle_x\,dy \,(= \langle Q(\varepsilon = y - f(x,a)|x)\rangle_x). \tag{12}$$

Finally, by substituting Eq. (7) into Eq. (12), the c.d.f. which plays a very important role to evaluate arbitrary percentage points in various engineering fields (e.g., noise evaluation index L_x for acoustic environment) can be evaluated as follows:

$$Q(y) = \left\langle \frac{\displaystyle\sum_{m=0}^{\infty}\sum_{n=0}^{\infty} A_{mn}\varphi_m^{(1)}(x) \int_{-\infty}^{y-f(x,a)} \varphi_n^{(2)}(\varepsilon)P_0(\varepsilon)\,d\varepsilon}{\displaystyle\sum_{m=0}^{\infty} A_{m0}\varphi_m^{(1)}(x)} \right\rangle_x. \tag{13}$$

So, after identifying in advance the expansion coefficient A_{mn} by using the data for learning, the response probability distribution in a form of c.d.f. can be predicted for the input data x.

2.2. Dynamical estimation method of regression parameters under the existence of external noise

In this section, we consider a realistic situation with observations contaminated by an external noise of arbitrary distribution type. Each expansion coefficient A_{mn} in the joint p.d.f. of Eq. (2) must be estimated on the basis of the noisy observations, because the expansion coefficient A_{mn} can not be evaluated based on the definition of Eq. (3) in the actual situation with the existence of external noise. In order to estimate the expansion coefficient A_{mn} based on successive observations under the existence of an additive external noise, the following observation equation is introduced:

$$z_k = y_k + v_k = f(x_k,a) + \varepsilon_k + v_k, \tag{14}$$

where z_k is the noisy observation at a discrete time k, and v_k denotes the external noise with known statistics. After regarding the expansion coefficients A_{mn} $(m = 0,1,...M;$ $n = 0,1,...,M')$ as unknown regression parameters, a simple dynamical model on the parameters is introduced in a successive estimation form employing a computer technique, as follows:

$$\begin{aligned} \boldsymbol{\alpha}(k+1) &= \boldsymbol{\alpha}(k), \\ \boldsymbol{\alpha}(k) &\equiv (\alpha_1(k),...,\alpha_N(k))^T = (A_{00k},...,A_{MM'k})^T, \end{aligned} \tag{15}$$

because the regression parameters to be estimated are intrinsically constant. Though Eq. (2) is originally an infinite series expansion, a finite expansion series with $m \leq M$ and $n \leq M'$ is adopted because only finite expansion terms are available and the consideration of the coefficients from the first few terms is usually sufficient in practice.

Next, in order to derive an algorithm to estimate successively the regression parameter $\boldsymbol{\alpha}(k)$ from the observations contaminated by additive noise, let us consider Bayes' theorem about the conditional p.d.f. as the fundamental relationship:

$$P(\boldsymbol{\alpha}(k)|Z_k) = \frac{P(\boldsymbol{\alpha}(k), z_k|Z_{k-1})}{P(z_k|Z_{k-1})}, \tag{16}$$

where Z_k $(= \{z_1, z_2, ..., z_k\})$ denotes a set of observations up to a time k. The conditional joint p.d.f. $P(\boldsymbol{\alpha}(k), z_k|Z_{k-1})$ on the unknown parameter $\boldsymbol{\alpha}(k)$ and the observed value z_k should be expanded generally in a statistical orthogonal expansion series. The product of two fundamental p.d.fs. for the unknown parameter $\boldsymbol{\alpha}(k)$ and the observation z_k is adopted as the first term of the series expansion. These two fundamental p.d.fs. $P_0(\boldsymbol{\alpha}(k)|Z_{k-1})$ and $P_0(z_k|Z_{k-1})$ can be determined *a priori* so as to describe the dominant parts of the actual fluctuation, or chosen artificially among the well-known standard p.d.fs. (such as Gaussian or gamma distribution functions). Then, the orthogonal series type expansion expression of $P(\boldsymbol{\alpha}(k), z_k|Z_{k-1})$ can be obtained as follows [2, 3]:

$$P(\boldsymbol{\alpha}(k), z_k|Z_{k-1}) = P_0(\boldsymbol{\alpha}(k)|Z_{k-1})P_0(z_k|Z_{k-1}) \sum_{\mathbf{m}=\mathbf{0}}^{\infty} \sum_{n=0}^{\infty} C_{\mathbf{m}n}\xi_{\mathbf{m}}^{(1)}(\boldsymbol{\alpha}(k))\xi_n^{(2)}(z_k) \tag{17}$$

with

$$C_{\mathbf{m}n} \equiv \left\langle \xi_{\mathbf{m}}^{(1)}(\boldsymbol{\alpha}(k))\xi_n^{(2)}(z_k)|Z_{k-1} \right\rangle, \tag{18}$$

where $\sum_{\mathbf{m}=\mathbf{0}}^{\infty}$ denotes

$$\sum_{\mathbf{m}=\mathbf{0}}^{\infty} \equiv \sum_{m_1=0}^{\infty} \sum_{m_2=0}^{\infty} \cdots \sum_{m_M=0}^{\infty}. \tag{19}$$

Here, $\xi_{\mathbf{m}}^{(1)}(\boldsymbol{\alpha}(k))$ $\left(\equiv \xi_{m_1 m_2 ... m_N}^{(1)}(\alpha_1(k), ..., \alpha_N(k)) \right)$ and $\xi_n^{(2)}(z_k)$ are the orthogonal polynomials of degree $\mathbf{m}$ $(= (m_1, m_2, ..., m_N))$ and n, associated with the weighting functions $P_0(\boldsymbol{\alpha}(k)|Z_{k-1})$ and $P_0(z_k|Z_{k-1})$ respectively, and must satisfy the following orthonormal relationships:

$$\int\int ... \int \xi_{\mathbf{m}}^{(1)}(\boldsymbol{\alpha}(k))\xi_{\mathbf{n}}^{(1)}(\boldsymbol{\alpha}(k))P_0(\boldsymbol{\alpha}(k)|Z_{k-1})\, d\boldsymbol{\alpha}(k) = \delta_{\mathbf{mn}}, \tag{20}$$

$$\int \xi_m^{(2)}(z_k)\xi_n^{(2)}(z_k)P_0(z_k|Z_{k-1}\, dz_k = \delta_{mn}. \tag{21}$$

Substituting Eq. (17) into Eq. (16), the following estimated p.d.f. on the parameter $\boldsymbol{\alpha}(k)$ is obtained:

$$P(\boldsymbol{\alpha}(k)|Z_k) = \frac{P(\boldsymbol{\alpha}(k)|Z_{k-1}) \sum_{\mathbf{m}=\mathbf{0}}^{\infty} \sum_{n=0}^{\infty} C_{\mathbf{m}n}\xi_{\mathbf{m}}^{(1)}(\boldsymbol{\alpha}(k))\xi_n^{(2)}(z_k)}{\sum_{n=0}^{\infty} C_{\mathbf{0}n}\xi_n^{(2)}(z_k)}. \tag{22}$$

By use of the above unified expression of Bayes' theorem, the recursive algorithm for estimating an arbitrary $\mathbf{S}$ ($\equiv (S_1, S_2, ..., S_N)$)-th order polynomial function $F_S(\boldsymbol{\alpha}(k))$ of the regression parameter can be easily derived in an infinite series expression, as follows:

$$\widehat{F}_S(\boldsymbol{\alpha}(k)) \equiv \langle F_S(\boldsymbol{\alpha}(k))|Z_k\rangle = \frac{\sum_{\mathbf{m}=\mathbf{0}}^{S}\sum_{n=0}^{\infty} C_{\mathbf{m}n} d_{\mathbf{m}}^{(S)} \xi_n^{(2)}(z_k)}{\sum_{n=0}^{\infty} C_{0n}\xi_n^{(2)}(z_k)}. \tag{23}$$

Here, the coefficient $d_{\mathbf{m}}^{(S)}$ is determined in advance to express $F_S(\bullet)$ in a series expansion form by use of $\xi_{\mathbf{m}}^{(1)}(\bullet)$:

$$F_S(\boldsymbol{\alpha}(k)) = \sum_{i=0}^{S} d_i^{(S)} \xi_i^{(1)}(\boldsymbol{\alpha}(k)). \tag{24}$$

In order to illustrate a practical form of general theory, Gaussian distribution functions are adpted as the fundamental p.d.fs. $P_0(\boldsymbol{\alpha}(k)|Z_{k-1})$ and $P_0(z_k|Z_{k-1})$:

$$P(\boldsymbol{\alpha}(k)|Z_k) = \prod_{i=1}^{N} N(\alpha_i(k); \alpha_i^*(k), \Gamma_i(k)), \tag{25}$$

$$P_0(z_k|Z_{k-1}) = N(z_k, z_k^*, \Omega_k) \tag{26}$$

with

$$\alpha_l^* = \langle \alpha_i|Z_{k-1}\rangle, \qquad \Gamma_i(k) = \left\langle (\alpha_i(k) - \alpha_i^*(k))^2|Z_{k-1}\right\rangle,$$
$$z_k^* = \langle z_k|Z_{k-1}\rangle, \qquad \Omega_k = \left\langle (z_k - z_k^*)^2|Z_{k-1}\right\rangle,$$
$$N(x;\mu,\sigma^2) = \frac{1}{\sqrt{2\pi\sigma^2}} \exp\left\{-\frac{(x-\mu)^2}{2\sigma^2}\right\}. \tag{27}$$

Then, the orthogonal functions in Eqs. (20) and (21) are expressed in terms of Hermite polynomials:

$$\xi_{\mathbf{m}}^{(1)}(\boldsymbol{\alpha}(k)) = \prod_{i=1}^{N} \frac{1}{\sqrt{m_i!}} H_{m_i}\left(\frac{\alpha_i(k) - \alpha_i^*(k)}{\sqrt{\Gamma_i(k)}}\right), \tag{28}$$

$$\xi_n^{(2)}(z_k) = \frac{1}{\sqrt{n!}} H_n\left(\frac{z_k - z_k^*}{\sqrt{\Omega_k}}\right). \tag{29}$$

The statistics of the contaminating noise v_k are assumed to be known in advance, and thus their p.d.fs. can be expressed in Gram–Charlier A type series form [4]:

$$P(v_k) = N(v_k; \overline{v}_k, R_k)\left\{1 + \sum_{n=3}^{\infty} \frac{\gamma_n}{\sqrt{n!}} H_n\left(\frac{v_k - \overline{v}_k}{\sqrt{R_k}}\right)\right\}, \tag{30}$$

$$\gamma_n \equiv \left\langle H_n\left(\frac{v_k - \overline{v}_k}{\sqrt{R_k}}\right)\right\rangle, \qquad \overline{v}_k = \langle v_k\rangle, \quad \left\langle (v_k - \overline{v}_k)^2\right\rangle. \tag{31}$$

Here, by using the statistical independence between x_k, ε and v_k, two statistics z_k^* and Ω_k in Eq. (27) can be expressed as follows:

$$\begin{aligned} z_k^* &= \langle f(x_k,a)|Z_{k-1}\rangle + \langle \varepsilon_k|Z_{k-1}\rangle + \overline{v}_k, \\ \Omega_k &= S_k + T_k + R_k, \\ S_k &= \left\langle \{f(x_k,a) - \langle f(x_k,a)|Z_{k-1}\rangle\}^2 |Z_{k-1}\right\rangle, \\ T_k &= \langle \varepsilon_k^2|Z_{k-1}\rangle - \{\langle \varepsilon_k|Z_{k-1}\rangle\}^2. \end{aligned} \tag{32}$$

By substituting Eqs. (25) – (32) into Eq. (18) and applying an additive theorem on Hermite polynomials, the expansion coefficient $C_{\mathbf{m}n}$ can be expressed as follows:

$$\begin{aligned} C_{\mathbf{m}n} &= \left\langle \prod_{i=1}^{N} \frac{1}{\sqrt{m_i!}} H_{m_i}\left(\frac{\alpha_i(k)-\alpha_i^*(k)}{\sqrt{\Gamma_i(k)}}\right) \frac{1}{\sqrt{n!}} H_n\left(\frac{z_k - z_k^*}{\sqrt{\Omega_k}}\right) \Big| Z_{k-1} \right\rangle \\ &= \frac{1}{\sqrt{n!}} \sum_{j=0}^{n} \binom{n}{j} \left(\sqrt{\frac{S_k+T_k}{\Omega_k}}\right)^{n-j} \left(\sqrt{\frac{R_k}{\Omega_k}}\right)^{j} \\ &\quad \bullet \sum_{r=0}^{[(n-j)/2]} (-1)^r (2r-1)! \binom{n-j}{2r} \frac{1}{\sqrt{S_k+T_k}} \sum_{l}^{n-j-2r} \binom{n-j-2r}{l} \\ &\quad \bullet \left\langle \left\{ f(x_k,a) - \langle f(x_k,a)|Z_k\rangle^{n-j-2r-l} |Z_{k-1}\right\}\right\rangle \\ &\bullet \left\langle \prod_{i=1}^{N} \frac{1}{\sqrt{m_i!}} H_{m_i}\left(\frac{\alpha_i(k)-\alpha_i^*(k)}{\sqrt{\Gamma_i(k)}}\right) \{\varepsilon_k - \langle \varepsilon_k|Z_{k-1}\rangle\}^l |Z_{k-1}\right\rangle \left\langle H_j\left(\frac{v_k-\overline{v}_k}{\sqrt{R_k}}\right)\right\rangle. \end{aligned} \tag{33}$$

Hereupon, $\langle \varepsilon_k^l|Z_{k-1}\rangle$ $(l=1,2,...)$ in Eqs. (32) and (33) are evaluated by use of Eq. (8).

In two special cases when $F_{0\ldots\underset{(i)}{010}\ldots 0}(\boldsymbol{\alpha}(k)) = \alpha_i(k)$ and $F_{0\ldots\underset{(i)}{020}\ldots 0}(\boldsymbol{\alpha}(k)) = (\alpha_i(k) - \widehat{\alpha}_i(k))^2$, two estimates related to mean and variance of the parameter are expressed as follows:

$$\begin{aligned} \widehat{\alpha}_i(k) &= \langle \alpha_i(k)|Z_k\rangle \\ &= \frac{\sum_{n=0}^{\infty} \left\{ C_{\mathbf{0}n} d_{0\ldots000\ldots0}^{(0\ldots010\ldots0)} + C_{0\ldots010\ldots0n} d_{0\ldots010\ldots0}^{(0\ldots010\ldots0)} \right\} \frac{1}{\sqrt{n!}} H_n\left(\frac{z_k - z_k^*}{\sqrt{\Omega_k}}\right)}{\sum_{n=0}^{\infty} C_{\mathbf{0}n} \frac{1}{\sqrt{n!}} H_n\left(\frac{z_k - z_k^*}{\sqrt{\Omega_k}}\right)}, \end{aligned} \tag{34}$$

$$\begin{aligned} p_i(k) &= \left\langle (\alpha_i(k) - \widehat{\alpha}_i(k))^2 |Z_k\right\rangle \\ &= \frac{\sum_{n=0}^{\infty} \left\{ C_{\mathbf{0}n} d_{0\ldots000\ldots0}^{(0\ldots020\ldots0)} + C_{0\ldots010\ldots0n} d_{0\ldots010\ldots0}^{(0\ldots020\ldots0)} + C_{0\ldots020\ldots0n} d_{0\ldots020\ldots0}^{(0\ldots020\ldots0)} \right\}}{\sum_{n=0}^{\infty} C_{\mathbf{0}n} \frac{1}{\sqrt{n!}} H_n\left(\frac{z_k - z_k^*}{\sqrt{\Omega_k}}\right)} \\ &\quad \bullet \frac{1}{\sqrt{n!}} H_n\left(\frac{z_k - z_k^*}{\sqrt{\Omega_k}}\right), \end{aligned} \tag{35}$$

with

$$\begin{aligned} d^{(0\ldots010\ldots0)}_{0\ldots000\ldots0} &= \alpha^*_i(k), \qquad d^{(0\ldots010\ldots0)}_{0\ldots010\ldots0} = \Gamma_i(k), \\ d^{(0\ldots020\ldots0)}_{0\ldots000\ldots0} &= \Gamma_i(k) + (\alpha^*_i(k) - \widehat{\alpha}_i(k))^2, \\ d^{(0\ldots020\ldots0)}_{0\ldots010\ldots0} &= 2\sqrt{\Gamma_i(k)}\,(\alpha^*_i(k) - \widehat{\alpha}_i(k)), \\ d^{(0\ldots020\ldots0)}_{0\ldots020\ldots0} &= \sqrt{2}\,\Gamma_i(k). \end{aligned} \tag{36}$$

Furthermore, by focusing on a polynomial function:

$$F_{0\ldots0N_i0\ldots0}(\boldsymbol{\alpha}(k)) = \frac{1}{\sqrt{N_i!}} H_{N_i}\left(\frac{\alpha_i(k) - \widehat{\alpha}_i(k)}{\sqrt{p_i(k)}}\right), \tag{37}$$

the estimate for the expansion coefficient of the parameter is given by

$$\begin{aligned} \widehat{\alpha}_{N_i}(k) &= \frac{1}{\sqrt{N_i!}} \left\langle H_{N_i}\left(\frac{\alpha_i(k) - \widehat{\alpha}_i(k)}{\sqrt{p_i(k)}}\right) \middle| Z_k \right\rangle \\ &= \frac{\displaystyle\sum_{n=0}^{\infty} \left\{ C_{0n} d^{(0\ldots0N_i0\ldots0)}_{0\ldots000\ldots0} + C_{0\ldots010\ldots0n} d^{(0\ldots0N_i0\ldots0)}_{0\ldots010\ldots0} + C_{0\ldots0N_i0\ldots0n} d^{(0\ldots0N_i0\ldots0)}_{0\ldots0N_i0\ldots0} \right\}}{\displaystyle\sum_{n=0}^{\infty} C_{0n} \frac{1}{\sqrt{n!}} H_n\left(\frac{z_k - z^*_k}{\sqrt{\Omega_k}}\right) \cdot \frac{1}{\sqrt{n!}} H_n\left(\frac{z_k - z^*_k}{\sqrt{\Omega_k}}\right)}, \end{aligned} \tag{38}$$

where $d^{(0\ldots0N_i0\ldots0)}_{0\ldots0l0\ldots0}$ $(l = 0, 1, \ldots, N_i)$ are coefficients satisfying the following relationship:

$$\frac{1}{\sqrt{N_i!}} H_{N_i}\left(\frac{\alpha_i(k) - \widehat{\alpha}_i(k)}{\sqrt{p_i(k)}}\right) = \sum_{l=0}^{N_i} d^{(0\ldots0N_i0\ldots0)}_{0\ldots0l0\ldots0} \frac{1}{\sqrt{l!}} H_l\left(\frac{\alpha_i(k) - \widehat{\alpha}_i(k)}{\sqrt{\Gamma_i(k)}}\right). \tag{39}$$

Finally, the predicted value of an arbitrary function $G(\boldsymbol{\alpha}(k+1))$ can be easily derived as:

$$\langle G(\boldsymbol{\alpha}(k+1)) | Z_k \rangle = \langle G(\boldsymbol{\alpha}(k) | Z_k \rangle . \tag{40}$$

Hence, by using Eqs. (34), (35), (38) and (40), the whole procedure of estimation and prediction algorithms is completed in a successive form matched to the use of computer technique.

3. Experimental consideration

In order to confirm the practical effectiveness of the proposed method, let us apply it to the prediction problem of the L_{eq} noise evaluation index for road traffic noise. In Eq. (1), we adopt an averaged headway interval d as the input signal x. In this case, the distance ℓ between a track lane and an observation point can be adopted as the system parameter a. Here, Eq. (1) is rewritten in the following specific formula:

$$L_{\mathrm{eq}} = f(d, \ell) + \varepsilon(d), \tag{41}$$

where $f(d, \ell)$ denotes the following well-known idealized model [5]:

$$f(d, \ell) \equiv L_w + 10 \log_{10} \frac{1}{2d\ell}. \tag{42}$$

In the above equation, L_w is an A-weighted average power level. Furthermore, from the additive property of energy quantities, the following observation equation at the k observation time can be found in this case:

$$z_k = 10 \log_{10} \left\{ 10^{[f(d_k, \ell) + \varepsilon(d_k)]/10} + 10^{v_k/10} \right\}. \tag{43}$$

For the purpose of deriving the specific prediction algorithm, when paying attention to the fact that the averaged headway interval d fluctuates within a non-negative fluctuation range, it is reasonable to employ a gamma distribution as the fundamental p.d.f. in the statistical orthogonal expansion for the random variable d [6]. In addition, when paying attention to the fact that the values of the correction term ε fluctuate over both positive and negative fluctuation ranges, it is also reasonable to employ Gaussian distribution as the fundamental p.d.f. in the statistical orthogonal expansion for the random variable ε. Therefore, these two fundamental p.d.fs. $P_0(d)$ and $P_0(\varepsilon)$ are employed as follows:

$$P_0(d) = \frac{d^{m_d - 1}}{\Gamma(m_d) s_d^{m_d}} e^{-d/s_d}, \tag{44}$$

$$P_0(\varepsilon) = \frac{1}{\sqrt{2\pi}\, \sigma_\varepsilon} e^{-\frac{(\varepsilon - \mu_\varepsilon)^2}{2\sigma_\varepsilon^2}}. \tag{45}$$

In Eq. (44), two parameters m_d and s_d are the distribution parameters by using a mean value μ_d ($\equiv \langle d \rangle$) for d and a variance σ_d^2 ($\equiv \langle (d - \mu_d)^2 \rangle$) for d, as follows:

$$m_d s_d = \mu_d, \qquad m_d s_d^2 = \sigma_d^2. \tag{46}$$

In Eq. (45), two parameters μ_ε and σ_ε^2 denote respectively a mean value of ε ($\equiv \langle \varepsilon \rangle$) and a variance ($\equiv \langle (\varepsilon - \mu_\varepsilon)^2 \rangle$). At this time, two orthonormal polynomials $\varphi_m^{(1)}(d)$ and $\varphi_n^{(2)}(\varepsilon)$ with two weighting functions are expressed in the following formulae:

$$\varphi_m^{(1)}(d) = \sqrt{\frac{\Gamma(m_d) m!}{\Gamma(m_d + m)}} L_m^{(m_d - 1)} \left(\frac{d}{s_d} \right), \tag{47}$$

$$\varphi_n^{(2)}(\varepsilon) = \frac{1}{\sqrt{n!}} H_n \left(\frac{\varepsilon - \mu_\varepsilon}{\sigma_\varepsilon} \right), \tag{48}$$

where $L_m^{(m_d - 1)}(\bullet)$ and $H(\bullet)$ denote respectively the associated Laguerre polynomial and Hermite polynomial. The expansion coefficient A_{mn} reflecting linear and non-linear correlation informations between ε and d can be evaluated as follows:

$$A_{mn} = \left\langle \frac{\sqrt{\Gamma(m_d) m!}}{\Gamma(m_d + m)} \frac{1}{\sqrt{n!}} L_m^{(m_d - 1)} \left(\frac{d}{s_d} \right) H_n \left(\frac{\varepsilon - \mu_\varepsilon}{\sigma_\varepsilon} \right) \right\rangle. \tag{49}$$

In this case, since the observed data is contaminated by external noise, it is impossible to estimate this expansion coefficient by using directly the above equation. So, it is necessary

to estimate this expansion coefficient by using the proposed recursive algorithm given by a wide sense digital filter.

The road traffic noise has been measured near a national main road in Hiroshima City. The actual location for measuring the road traffic noise is shown in Fig. 1. Simultaneously, the vehicle numbers for heavy and light categories have been counted within the length L under consideration. As the averaged headway interval d, the evaluation procedure $d = \langle L/N \rangle$ according to the original definition can be employed. The L_{eq} data measured in each 1 minute observation interval has been measured successively. Moreover, a white noise has been used as an external noise. Of course, in the proposed method, it is possible to employ an arbitrary non-Gaussian type noise fluctuation as an external noise. Hereupon, the white noise of Gaussian type is very often used as one of the standard random excitations in various acoustic experiments. At the starting point of the experimental consideration for the purpose of confirming the principal effectiveness of the proposed methodology, since an arbitrary p.d.f. (or c.d.f.) of non-Gaussian type noise fluctuation can be theoretically expressed in an infinite orthonormal expansion form with Gaussian p.d.f. (or c.d.f.) in the first expansion term and successively the n-th $n = 3, 4, ...$) differential of Gaussian p.d.f. (or c.d.f.) in the n-th expansion term (see Appendix), it is quite natural to employ the usual white noise with the known acoustic characteristics and statistical properties (on Gaussian p.d.f.) in advance.

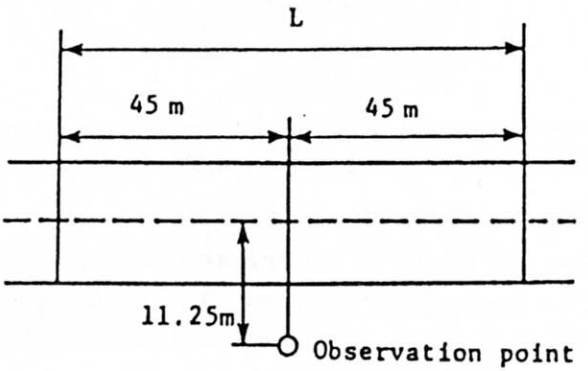

Fig. 1. The actual location for measuring the road traffic noise.

After identifying in advance the regression parameters by using the first half of data for learning process, we predict the c.d.f. for the latter half of data. The predicted results by using the proposed prediction method are shown in Fig. 2. The predicted results by using the proposed method are in good agreement with the experimental values, as compared with the result by using directly Eq. (42) with no correction term in a case of no existence of external noise. Thus, the practical effectiveness of the proposed method has been experimentally confirmed.

Here, in this case, the values of L_{eq} at another observation point can be originally predicted by using the idealized prediction formula of Eq. (42) (reflecting an arbitrary distance ℓ). After then, we must examine the regression relationship between the deviations and the averaged headway intervals from the theoretical and/or experimental

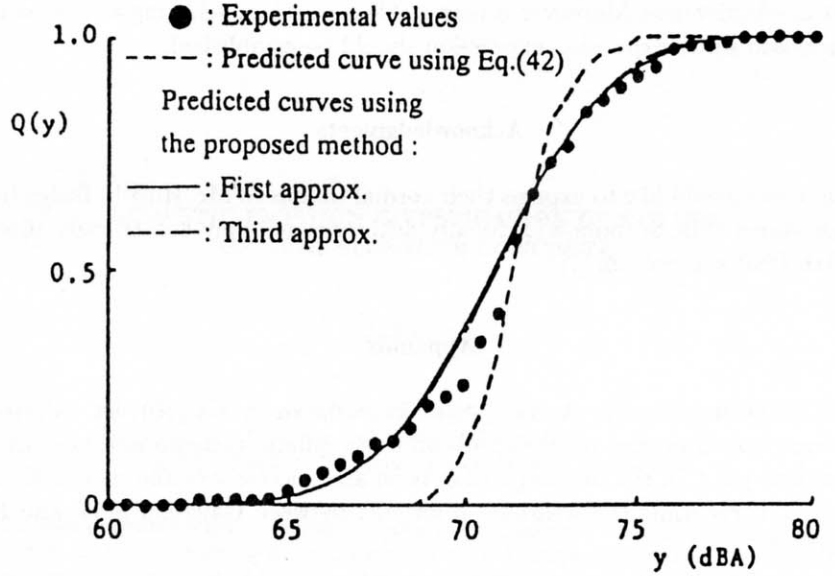

Fig. 2. A comparison between the experimentally sampled points and the theoretically predicted curves for the cumulative distribution form.

viewpoints by taking account of the physical mechanisms, e.g., the geometrical structure of road, the sound propagation characteristics and so on. That is, the correction term from the idealized model should be evaluated theoretically and/or experimentally when changing the observation point.

4. Conclusions

In this paper, a new modeling method with the ability of extracting the available informations latent in the deviations from an idealized system model has been proposed by considering not only the averaged form of actual systems but also the deviations from its averaged form. Namely, an additive correction term with probabilistic characteristics as the above deviations has been first introduced for the purpose of grasping quantitatively the fluctuations around the averaged form. Next, in order to find the regression relationship between this correction term and a stochastic input signal, a prediction method for the output response probability has been proposed by introducing a generalized regression analysis method of an extended type with less information loss. Moreover, by paying attention to the actual measurement under the existence of background noise, a recursive estimation algorithm has been proposed by introducing a wide sense digital filter. Finally, the effectiveness of the proposed method has been experimentally confirmed by applying it to the prediction problem of L_{eq} for road traffic noise.

Since this study is in an early stage, there still remain several future problems. For example, this method must be applied to many other actual cases to broaden and confirm

its practical effectiveness. Moreover, a reasonable method for selecting an optimum order of the proposed series expansion expression should be established.

Acknowledgments

The authors would like to express their cordial thanks to Mr. Hiroshi Ikebuchi for his kind suggestions. The authors additionally acknowledge many constructive discussions in the 11th DSP symposium [7].

Appendix

Based on Gram–Charlier A type series form shown in Eq. (30), let us now derive the arbitrary non-Gaussian p.d.f. expression in an infinite orthonormal expansion form with Gaussian p.d.f. in the first expansion term and successively the n-th differential of Gaussian p.d.f. By using the well-known formula between Gaussian p.d.f. and Hermite polynomial [4]:

$$N(v_k;\overline{v}_k,R_k)H_n\left(\frac{v_k-\overline{v}_k}{\sqrt{R_k}}\right)=(-1)^nR_k^{n/2}\frac{d^n}{dv_k^n}N(v_k;\overline{v}_k,R_k), \tag{A.1}$$

the objective expression can be derived as follows:

$$P(v_k)=N(v_k;\overline{v}_k,R_k)+\sum_{n=3}^{\infty}(-1)^n\frac{\gamma_n}{\sqrt{n!}}R_k^{n/2}\frac{d^n}{dv_k^n}N(v_k;\overline{v}_k,R_k). \tag{A.2}$$

In the same manner, the c.d.f. formula for this expression can be also derived.

References

[1] M. OHTA, A. IKUTA and N. TAKAKI, *A new trial of regression analysis with less information loss and its application to the sound insulation walls Matching to the prediction of response probability distribution* [in Japanese], J. Acoust. Soc. Jpn, **44**, 848–855 (1988).

[2] M. OHTA, K. HATAKEYAMA and M. NISHIMURA, *Some unified methods in multivariate linear filtering and prediction problems by use of the expansion form of Bayes' theorem*, Proc. of the 26th Japan National Congress for App. Mech., 383–398 (1976).

[3] M. OHTA and H. YAMADA, *New methodological trials of dynamical state estimation for the noise and vibration environmental system Establishment of general theory and its application to urban noise problems*, Acustica, **6**, 199–212 (1984).

[4] G.E.P. BOX and G.M. JENKINS, *Time series analysis — Forecasting and control*, Holden-Day (1970).

[5] M. OHTA and T. KOIZUMI, *General statistical treatment of the response of a linear rectifying device to a stationary random input*, IEEE Trans. Inf. Theory, **IT-14**, 595– 598 (1968).

[6] Edition by the Acoust. Soc. Jpn, *Noise and Vibration* (II) [in Japanese], 1982.

[7] Y. MITANI, M. OHTA and A. IKUTA, *An estimation theory of regression parameters based on digital filter in a hierarchical form and its application to traffic noise* [in Japanese], Proc. of DSP Symposium, 593–598 (1996).

ARCHIVES OF ACOUSTICS
24, 2, 233–244 (1999)

ACOUSTIC-EMISSION INVESTIGATION OF FAILURE OF HIGH-STRENGTH CONCRETE

J. HOŁA

Institute for Building Engineering
Wrocław University of Technology
(50-370 Wrocław, Wybrzeże Wyspiańskiego 27, Poland)

This paper presents results of acoustic-emission investigations of the failure of high-strength concrete. Concretes differing in their composition and compressive strength were tested. Several acoustic emission (AE) parameters were recorded as a function of failure time. It has been shown that the failure of such concretes is signalled, starting from a certain stress level, by visibly intensifying acoustic activity. An analysis of the AE measurements has shown that the failure of the tested high-strength concretes is not continual but multistage. Stress values which delimit these stages have been determined.

1. Introduction

High-strength concrete, in comparison with plain concrete, is characterized by very high compressive strength and a rapid increase of this strength at the initial stage of hardening. Its minimum compressive strength amounts to 60 MPa after 28 days of hardening [1, 2, 3]. This high strength is obtained by using aggregate and cement of proper quality and a small quantity of make-up water and modifying the structure with appropriate additives and chemical admixtures. Such concrete has been used increasingly more often in building practice to make concrete and reinforced concrete structural components, such as monolithic and prefabricated framework members employed in tall buildings and building structures, which work under heavy loads [3, 4, 5].

The stress pattern in the structure of loaded high-strength concrete is considered to be more uniform than that in plain concrete [2, 3, 6]. As a result, stress concentrations in the former are reduced. The size of defects which appear during the production stage is reduced due to a superplasticizer admixture and an addition of very fine particles of microsilica. The variation in porosity also is reduced and the interfacial transition zone becomes more consolidated. The difference between the rigidity of the aggregate and that of the cement mortar is smaller. As a result, fewer microcracks appear in the structure of loaded high-strength concrete whereby the crack resistance of this material increases but at the same time a fracture is more sudden [2, 3]. It is not clear if there is any warning sign of this sudden fracture. It is known only that during standard strength tests high-strength concrete fails in an "explosive" way. It is not clear either if, similarly

as in plain concrete, the failure of this concrete is a multistage process and what the stress, i.e. initiating stress σ_i and critical stress σ_{cr}, levels delimiting the particular stages are. Papers [7, 8] deal with the investigation of the failure of concrete possessing high compressive strength but not exceeding 60 MPa. Taking into account the findings presented in papers [9, 10, 11, 12, 13, 14, 15 and 16], it can be assumed that the above kinds of stress delimit the particular stages in the failure of concrete. It is accepted that the initiating stress marks the upper limit of the elastic zone of concrete work under short-time loads and it assumes a similar value as that of the fatigue strength of the concrete. The critical stress is identified with the long-term strength of concrete. It is essential to know the values of these stresses in order to assess properly the durability and safety of, especially, concrete structures subjected to repeated loading or overloads. Since structures made of high-strength concrete are not an exception to this, the problems touched upon in this paper are important both for theory and practice.

2. Description of tests

Four high-strength concretes, made from crushed 2 – 16 mm basalt aggregate, washed 0 – 2 mm sand and Portland cement 45, were tested. Concrete composition designated as "0", which was first modified with a superplasticizer and then with a superplasticizer and micro silica to obtain ever higher values of compressive strength, was taken to be the initial composition. Table 1 summarizes the basic data on the tested concretes and Fig. 1 shows the increase in their compressive strength in time.

Table 1. Basic data on tested high-strength concretes.

Concrete designation	Components in kg/m^3					Average compressive strength sfter 28 days [MPa]
	Cement	Aggregate	Water	Super-plasticizer	Micro-silica	
"0"	450	2033	180	–	–	65
"1"	450	2085	146	9.00	–	86
"2"	450	2096	140	11.25	13.50	95
"3"	450	2069	140	13.50	31.50	105

The failure of the concretes was investigated, after 90 days of curing, by subjecting 50 × 50 × 100 mm specimens cut out from larger elements to axial compression. There were 12 specimens in each batch of concrete. The acoustic emission technique was used. A diagram of the AE measuring position is shown in Fig. 2. The sum and rate of AE count, the sum of events and the short pulse energy were recorded versus failure time and stored in the computer's memory. The ultrasonic technique was used as an ancillary. In this case, changes in the velocity of longitudinal ultrasonic waves versus the stress increment were examined perpendicular to the direction of compression in 150 × 150 × 150 mm specimens.

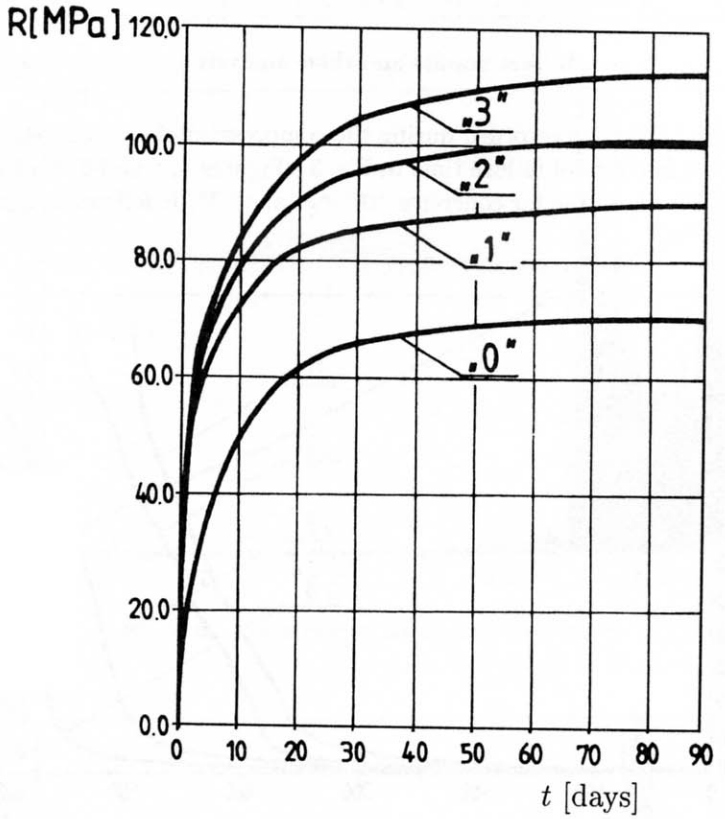

Fig. 1. Increase of compressive strength in time for tested high-strength concretes.

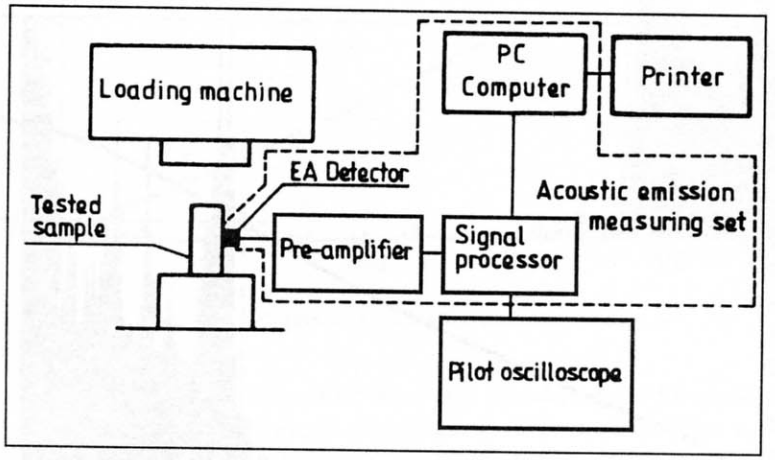

Fig. 2. Diagram of AE measuring position.

3. Test results and their analysis

The averaged AE counts recorded during the compression of the concrete specimens are presented as a function of failure time in Fig. 3. Figures 4, 5 and 6 show the rate of AE counts versus failure time for concretes "0", "1" and "3". It follows from the figures

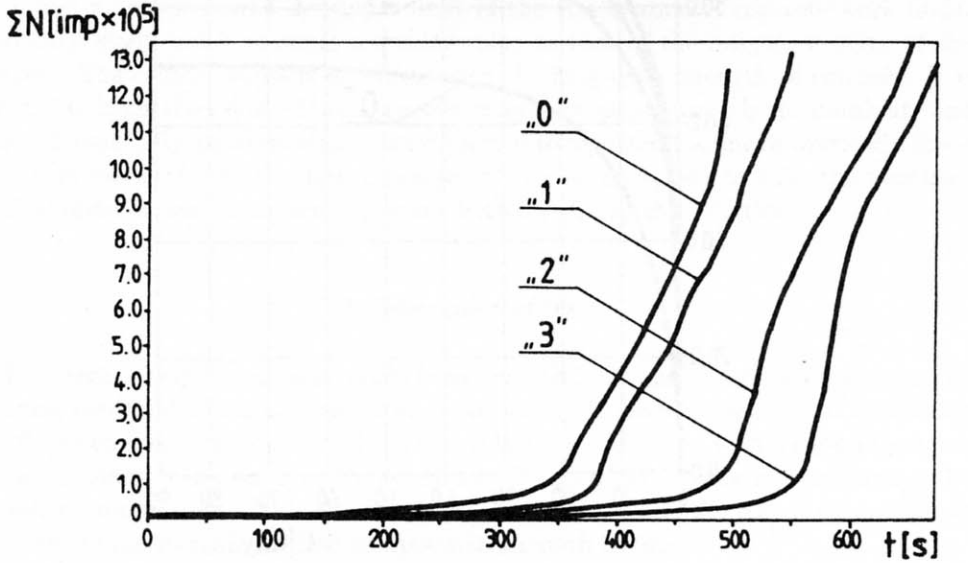

Fig. 3. AE counts vs. failure time determined during compression of high-strength concretes "0", "1", "2" and "3".

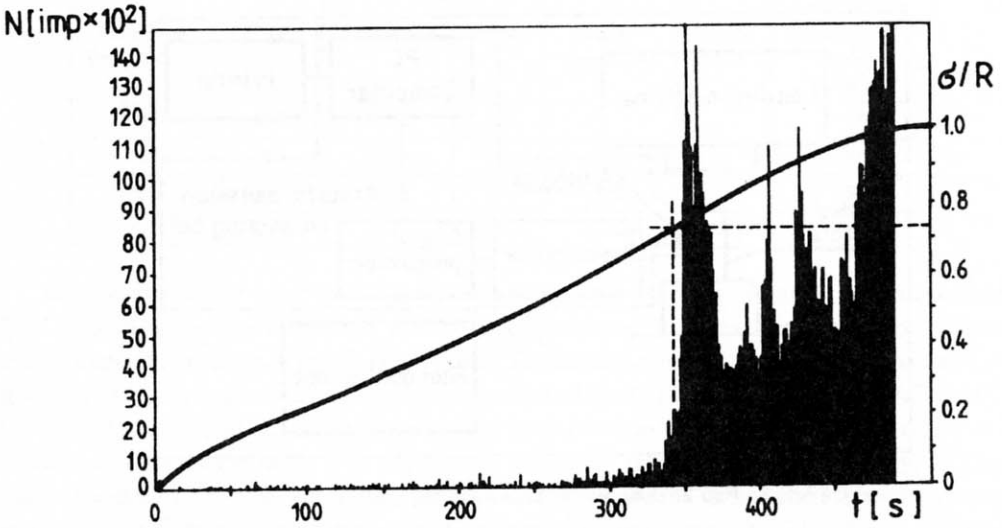

Fig. 4. AE counts rate vs. failure time for concrete "0".

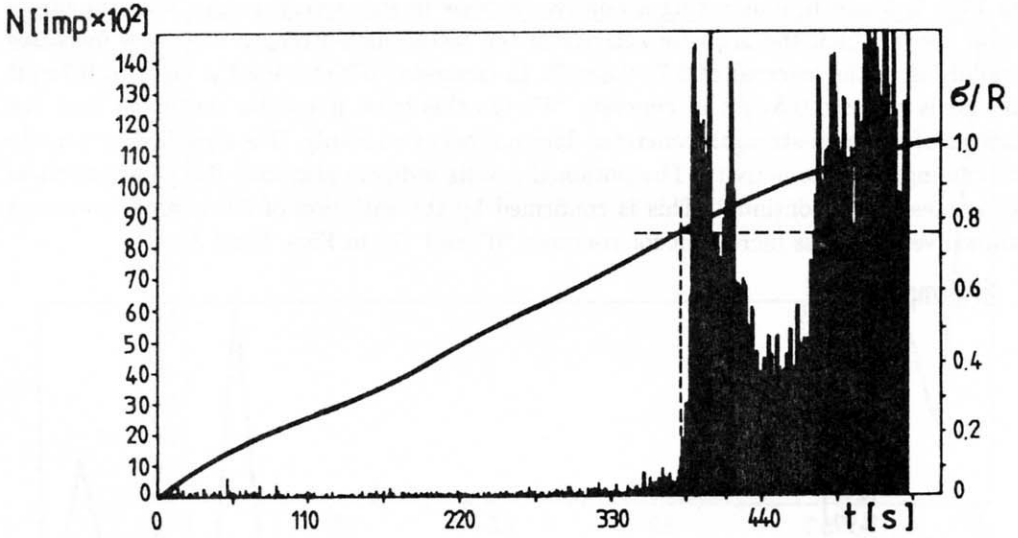

Fig. 5. AE counts rate vs. failure time for concrete "1".

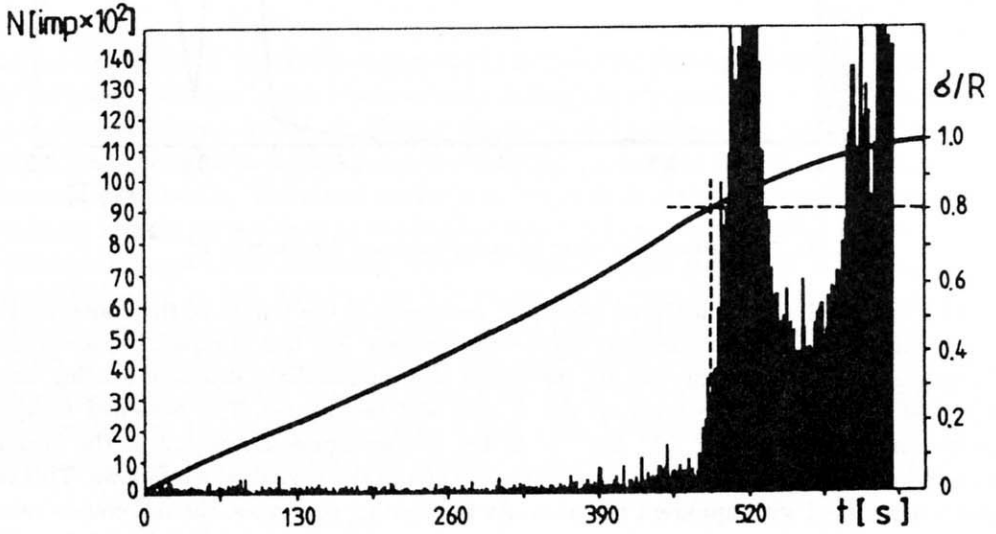

Fig. 6. AE counts rate vs. failure time for concrete "3".

that the acoustic activity of the tested concretes remains slight for some time after the commencement of loading. This indicates that few microcracks appear at the initial and intermediate stages of loading. It is only at the final stage of loading that the values of the measured AE parameters increase rapidly, which indicates that microcracks appear and develop at a very fast rate. Similar observations were made by the authors of paper [8] during the testing of high-strength concretes. It follows from the auxiliary diagrams

in Figs. 4, 5 and 6, illustrating a relative increase in stress versus time, that the stress level above which the acoustic activity of the tested high-strength concretes increases rapidly is in the interval of $0.7-0.8\sigma/R$. In concrete "0", this level is close to $0.7\sigma/R$ and it is close to $0.8\sigma/R$ in concrete "3". On this basis it can be concluded that the failure of the high-strength concretes does not occur suddenly. It is signalled by rapidly increasing acoustic activity. The obtained results indicate also that the failure of these concretes is not continual. This is confirmed by the variation of AE counts increment shown versus stress increment for concrete "0" and "1" in Figs. 7 and 8.

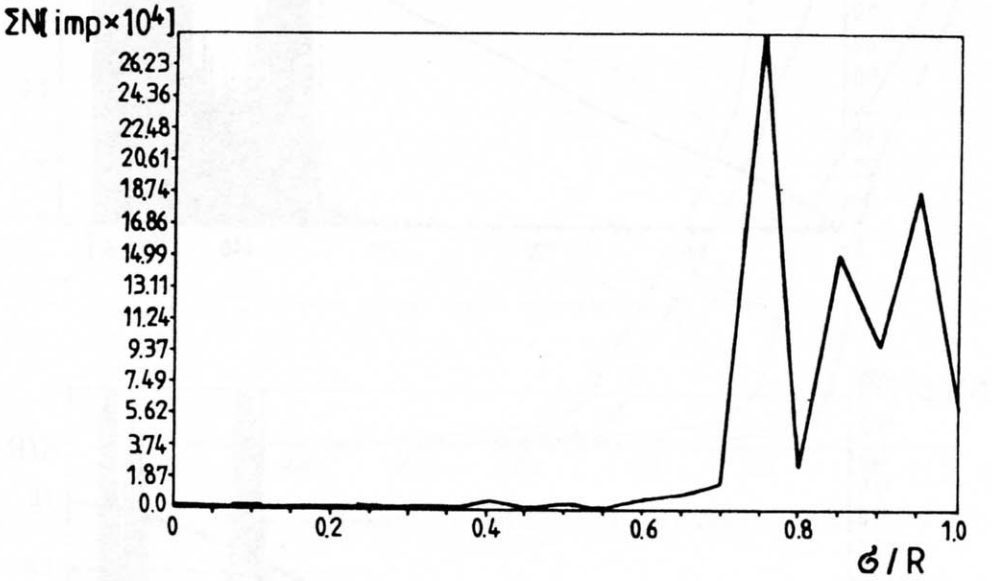

Fig. 7. AE counts increment vs. stress increment for concrete "0".

The test results were analyzed closely to determine if the failure of the concretes is a two-stage or, as in plain concrete, three-stage process. For this purpose, the accuracy of reading of AE counts rate during the initial and intermediate stages of loading was increased by changing the scale on the X-axis and the Y-axis. The obtained results are shown for concrete "0", "1" and "3" in Fig. 9. The figure shows that at the initial stage of loading the count rate is slightly faster than in the period which follows. This is clearly associated with apparent emission. As the loading continues, the AE counts rate decreases and stabilizes. One can say that the loaded concretes have "quietened down". At the intermediate stage the count rate begins to grow steadily. When the loading enters the final stage, the AE counts rate goes up sharply and continues to increase rapidly until the concrete fails totally. The stress levels which delimit these stages are marked in Fig. 9. The results of the investigations indicate that the failure of the high-strength concretes is a multistage process. These findings have been verified, although less firmly, by the measurements of the energy of short AE pulses, shown for concrete "0", "1" and "3" in Fig. 10. It is significant that the stress level at which stabilization ends and a steady increase of both the counts rate and the AE short signals energy begins is close

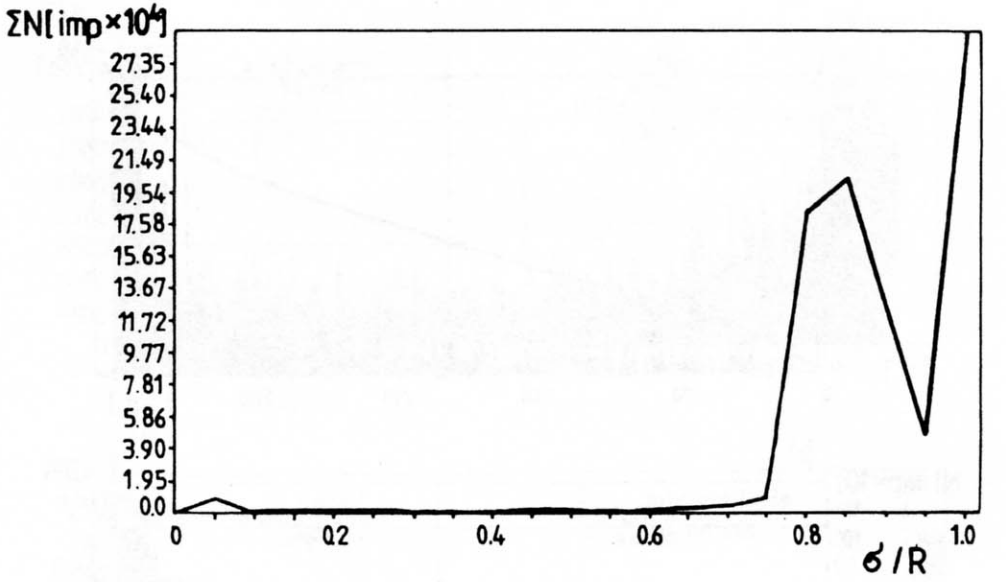

Fig. 8. AE counts increment vs. stress increment for concrete "1".

to the stress level at which also a decrease in the velocity of longitudinal ultrasonic waves is observed. Changes in the latter velocity during the compression of the high-strength concretes are shown in Fig. 11. Taking the above observations and the criteria given in [13, 15] into account, it can be assumed with a high probability that this level corresponds to initiating stress σ_i. The stress level at which the values of the measured AE parameters increase rapidly corresponds to the level at which it becomes impossible to measure the velocity of longitudinal ultrasonic waves in high-strength concretes. According to the criteria defined in [13, 14], this level corresponds to critical stress σ_{cr}. The averaged values of initiating and critical stresses in the tested concretes have been compiled in Table 2. It should be mentioned that the compressive force versus failure time data stored in the computer's memory turned out to be very useful for the determination of the stresses. It follows from Table 2 that both initiating and critical stress values are the higher, the higher the compressive strength of the tested concretes. They are

Table 2. Initiating and critical stress values determined for high-strength concretes by acoustic emission technique.

Concrete designation	Initiating stress σ_i	Critical stress σ_{cr}
"0"	0.40	0.73
"1"	0.45	0.76
"2"	0.52	0.80
"3"	0.54	0.82

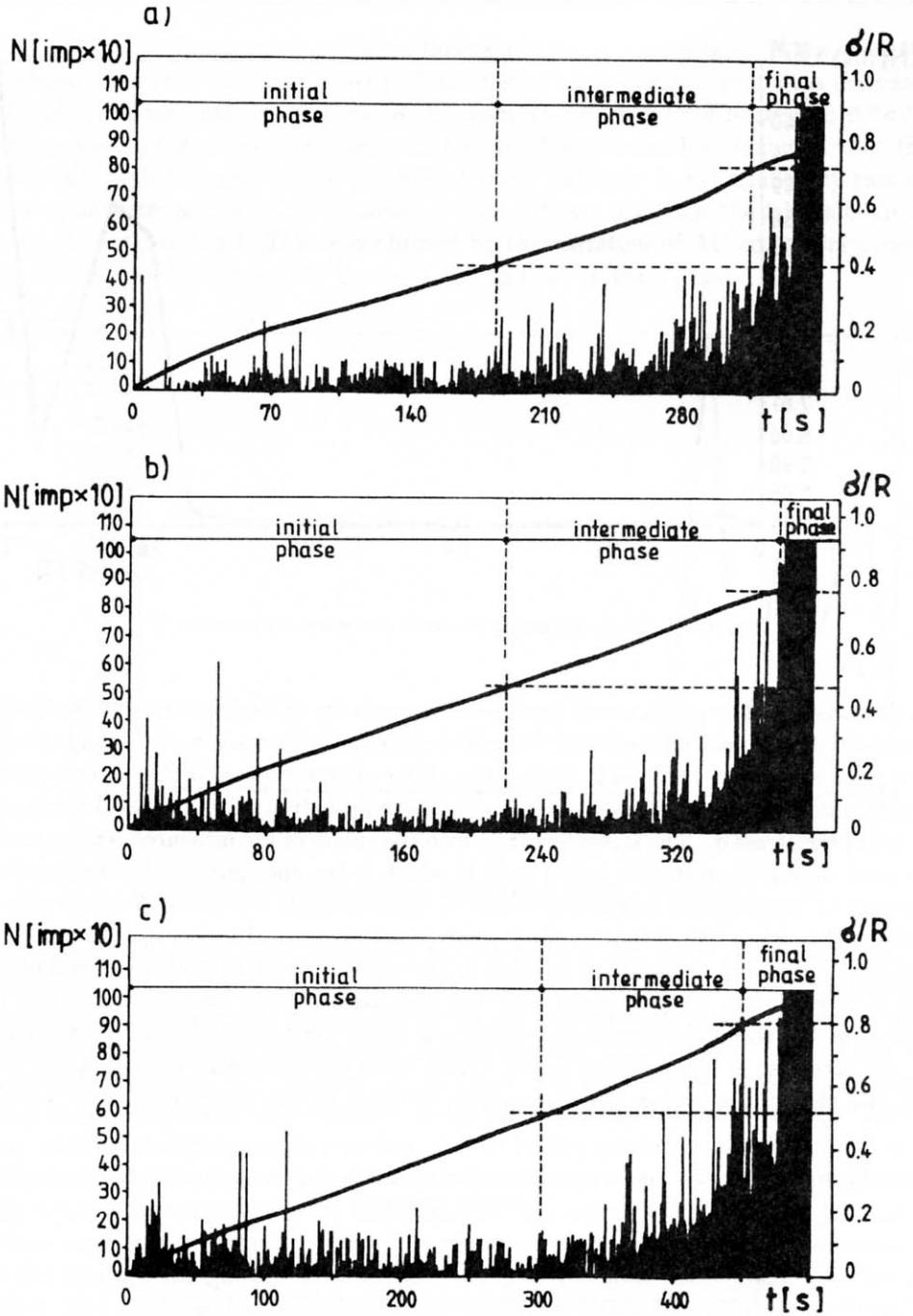

Fig. 9. AE counts rate at initial and intermediate stages of loading for: a) concrete "0", b) concrete "1", c) concrete "3".

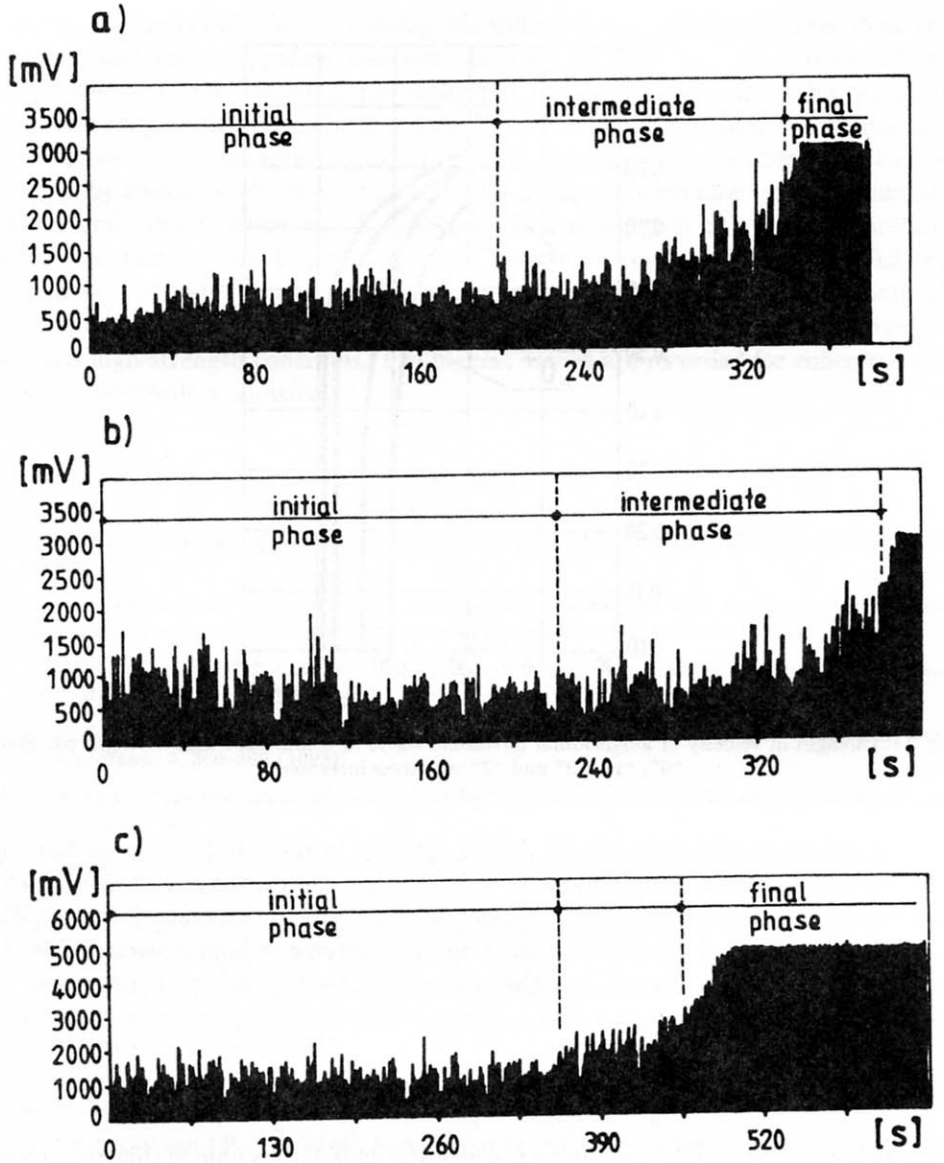

Fig. 10. Measurements of AE short pulses energy in: a) concrete "0", b) concrete "1", c) concrete "3".

highest in the high-strength concretes which contain microsilica. This may be due to the positive effect of microsilica on the structure of concrete. As mentioned previously, micro silica causes, among other things, the compaction of the structure in the interfacial transition zone between the aggregate and the cement paste [17, 18]. It contributes to a reduction in both the size of the portlandite crystals and the degree of their orientation relative to the aggregate grains [17, 18]. It also brings about a reduction in the size

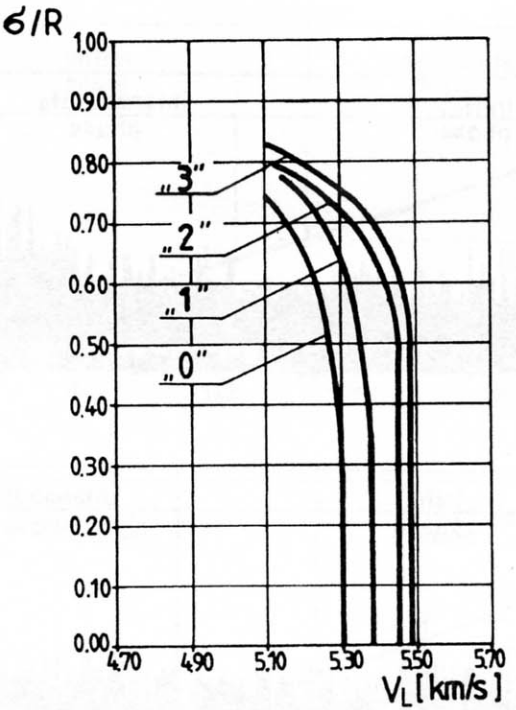

Fig. 11. Changes in velocity of longitudinal ultrasonic waves in compressed high-strength concretes "0", "1", "2" and "3" vs. stress increment.

of the largest pores and their partial closing not only in the interfacial transition zone but in the whole cement paste volume as well [19]. As a result, the size of defects which appear in the structure of high-strength concrete at the production stage decreases. Thus microcracks appear and develop in high-strength concretes at higher stress levels than in plain concrete, as manifested by higher values of initiating and critical stresses.

4. Conclusions

It has been determined by applying the acoustic emission technique that the acoustic activity of the tested high-strength concretes is very low at the initial and intermediate stages of loading. This indicates that very few microcracks appear during this time. A rapid increase in this activity, indicating intensive microcracking, occurs only at the final stage of loading. On the basis of the obtained results it can be concluded that the failure of high-strength concrete is not sudden and it is preceded by warning signs. The stress level at which the warning signs are very clear depends on the compressive strength of concrete and for the tested concretes it is in the interval of $0.7-0.8\,\sigma/\mathrm{R}$.

An analysis of the AE counts rate and the AE short pulses energy recorded as a function of failure time has shown that these relationships do not have continual

character. At the initial stage of loading the values of the parameters, after their slight initial increase due to apparent emission, decrease and stabilize. Then there follows a steady increase in the values of the measured AE parameters, which becomes rapid at the final stage of loading. On this basis it can be concluded that the failure of the tested high-strength concretes is not a continual but multistage process. This has been confirmed by results of ultrasonic tests. The limits of the particular stages are initiating stress σ_i and critical stress σ_{cr}. It has been determined that the values of initiating stress in the tested high-strength concretes are within the interval of $0.40-0.54\,\sigma/R$. The values of critical stress are in the interval of $0.73-0.82\,\sigma/R$. It is symptomatic that the values of the two kinds of stress are the higher, the higher the compressive strength of the tested high-strength concretes. The highest values are recorded for concretes which contain an microsilica addition.

References

[1] J. MIKOŚ, *Technology of high strength concretes* [in Polish], Przegląd Budowlany, 8-9, 355–358 (1992).

[2] L. KUCHARSKA and A.M. BRANDT, *Composition, production and mechanical properties of high-strength concretes* [in Polish], Inżynieria i Budownictwo, 9, 356–360 (1993).

[3] J. JASICZAK and P. MIKOŁAJCZYK, *Technology of concrete modified by admixtures and additives. Domestic and foreign tendencies* [in Polish], Poznań 1997.

[4] R. KOWALCZYK, *Application of high strength concrete in high buildings* [in Polish], Inżynieria i Budownictwo, 9, 366–369 (1993).

[5] K. FLAGA, *Reflection about application of high-grade concrete in Poland* [in Polish], Przegląd Budowlany, 6, 4–7 (1995).

[6] L. KUCHARSKA, *Forming of the structure of high-efficient concretes, the role of additions and admixtures* [in Polish], Przegląd Budowlany, 8-9, 351–354 (1992).

[7] M.M. SMADI and F.O. SLATE, *Microcracking of high and normal strength concrete under short- and long-term loadings*, ACI J., **86**, 3, 117–127 (1989).

[8] J. MIERZWA, K. POGAN and Z. RANACHOWSKI, *The correlation between the generated acoustic emission and the compressive and static strength in plain and high strength concrete*, Archives of Acoustics, **22**, 3, 333–342 (1997).

[9] S.P. SHAH and S. CHANDRA, *Critical stress volume change and microcracking of concrete*, ACI J., **65**, 9, 770–781 (1968).

[10] K. NEWMANN and I.B. NEWMANN, *Failure theories and design criteria for plain concrete. Structures, solid mechanics and engineering design*, Proc. Southampton, 1969, Civ. Eng. Mat. Conf., 963–995, London 1971.

[11] A.M. BRANDT *et al.*, *Cracking and failure mechanism in concrete-like composites* [in Polish], [in:] Mechanical Properties and Structures of Concrete Composites, Polish Academy of Sciences, Ossolineum, 163–209, 1974.

[12] Z. RANACHOWSKI, *Application of acoustic emission method to determine the limit of proportionality and the static strength in concrete*, [in:] Brittle Matrix Composites 3, A.M. BRANDT and I.H. MARSHALL [Eds.], Elservier Applied Science Publishers, London and New York, 234–239, 1991.

[13] J. HOŁA, *Effect of aggregate grading on the stress degradation of compressed concrete*, Archives of Civil Engineering, 1–2, 85–101 (1992).

[14] K. FLAGA, *The influence of the stresses on the stress destruction and the strength parameters of concrete. Analytical models and new concepts in mechanics of structural concrete*, Published by the Białystok University of Technology, Białystok, 55–77, 1993.

[15] J. HOŁA, *Acoustic emission in concrete: Acoustic emission sources, application, methods* [in Polish], J. MALECKI and J. RANACHOWSKI [Eds.], Institute of Fundamental Technological Research, Polish Academy of Sciences, Biuro Pascal, Publishers, Warsaw, 223–240, 1994.

[16] P. STROEVEN and A. MOCZKO, *Assessment of damage evolution stages in cementitious composites by acoustic emission technique*, 2nd International Conf. on Nondestructive Testing of Concrete in the Infrastructure, Nashville, 12–14, 1996.

[17] J. PIASTA and W. PIASTA, *Aggregates v. high strength concretes* [in Polish], Przegląd Budowlany, 8–9, 361–363 (1992).

[18] Cz. WOLSKA-KOTAŃSKA, *Utilization of a silica dustdirective tendency in world building industry* [in Polish], Przegląd Budowlany, 2, 19–21 (1995).

[19] A.M. BRANDT, *Influence of the interfacial transition zone (ITZ) on the mechanical properties of high performance concretes (HPC)* [in Polish], [in:] Zagadnienia materiałowe w Inżynierii Lądowej MATBUD'98, Kraków-Mogilany, 21–30, 1998.

ARCHIVES OF ACOUSTICS
24, 2, 245–247 (1999)

C H R O N I C L E

DISSERTATIONS

Investigation of dynamic characteristics of vibration of acoustic sources with complex mechanical structure by means of modal analysis [in Polish]

by JACEK KROMULSKI
June 1998
Adam Mickiewicz University, Institute of Acoustics,
Industrial Institute of Agricultural Engineering,
ul. Starolecka 31, Poznań, Poland
e-mail: kromulsk@pimr.poznan.pl
Supervisor: Prof. dr. hab. E. Hojan

The aim of the dissertation was to complete the modal identification procedure with singular value decomposition method.

Two experimental modal analysis methods are presented for the determination of operational deflection shapes (ODSs). The first method allows one to determine the ODSs by measuring mechanical vibrations at test points of the operating machine (created by the forces occurring in the actual work cycle). The second method is based on the modal model of the machine, including the forces which occur in the operation process, and yields the operational modes of vibration. The forces introduced into the model are calculated by inverting of FRF matrix and multiplying it by the operating response vector. The determination of the forces involved is necessary for the definition of the paths of energy transfer and for the analysis of the noise emitted by the mechanical system (machine).

The two methods of determination of operational deflection shapes described in this dissertation (modal and operational), as verified by investigating the corn-flattening contrivance, yield similar results.

The dissertation contains the practical examples of identification of uncorrelated sources of exciting forces by means of singular value decomposition method. A commonly used method of identification the uncorrelated sources of exciting forces is the method of square crosspower spectrum matrix decomposition into eigenvalues. In the dissertation there is discussed practical use of the method of crosspower spectrum matrix decomposition into singular values in problems of identification of exciting forces

sources. The method allows to draw the conclusions about the number of uncorrelated exciting forces acting in the system. The application of the method of decomposition of crosspower spectrum matrices into singular values allows to reduce the number of performed calculations. If there are several dominant exciting forces, there is no need to determine all elements of crosspower spectrum matrices, only some chosen columns and rows should be determined.

A new method of identification uncorrelated sources based on singular value decomposition of autopower spectrum matrix was also presented in the dissertation.

All these methods were used to identify the sources of the exciting forces acting during the work of a real mechanical system – a collecting press of high level crushing.

The dissertation describes also the possibility of application of singular value decomposition method for analysis of dynamic behaviours of the system with varying mechanical parameters. The decomposition into the principal spectra system responses allows to make the reduction of existing in the system changes of mechanical parameters to those which influence on changes of system responses is crucial. The method can find as well its application for minimalization of noise occurring in the operating characteristics of the system.

The imaging possibility analysis of an inner object structure using the ultrasound transmission tomography method [in Polish]

Doctor Thesis
by KRZYSZTOF J. OPIELIŃSKI
December 2, 1998
Institute of Telecommunications and Acoustics
Wrocław University of Technology
Wybrzeże Wyspiańskiego 27, 50-370 Wrocław, Poland
Supervisor: Andrzej B. Dobrucki

The imaging possibility analysis of an inner object structure using the ultrasound transmission tomography method (UTT) has been described in the dissertation. The parallel ray projection geometry was used for an acquisition of measured data. The ultrasonic wave time-of-flight was chosen as a measured acoustical parameter of the object.

In particular, the problems relating to the ultrasonic tomography have been systematized. The convolution and backprojection algorithm has been adapted for UTT as an image reconstruction method. It was also optimized and tested. The computer software has been elaborated in order to create object cross-sections, to simulate tomographic measurements and to reconstruct images. The computer measurement system for UTT has been designed and programmed, and the examinations on real objects were provided.

On the base of experiments and simulated calculations, the most essential error sources introducing distortions into reconstructed image, have been recognized. The magnitude of the errors was estimated and the ways of error minimization were proposed and tested. It enabled to define the possibilities of UTT applications.

The theoretical and experimental results have shown, that it is possible to construct the ultrasonic transmission tomograph, which uses a personal computer as the main unit. It allows to characterize an inner object structure in both: quantitative and qualitative ways. It can be done by means of the local value distribution imaging of the acoustical parameters of the object.